NTNU – Trondheim
Norwegian University of
Science and Technology

Handling Unknown External Forces with Highly Responsive DP Controller

Christoffer Andreas Ofstad

Master of Science in Cybernetics and Robotics
Submission date: February 2014
Supervisor: Tor Arne Johansen, ITK
Co-supervisor: Thor Inge Fossen, ITK

Norwegian University of Science and Technology
Department of Engineering Cybernetics

NTNU
Norwegian University of Science and Technology
Cybernetics

Faculty of Information Technology, Mathematics and Electrical Engineering
Department of Engineering

MSC THESIS DESCRIPTION SHEET

Name:	Christoffer Andreas Ofstad
Department:	Engineering Cybernetics
Thesis title:	Handling Unknown External Disturbances with Highly Responsive DP Controller

Thesis Description: Current DP controllers are not optimal for handling large and sudden unknown external forces, such as ice loads, cables, and similar. Wave filtering, estimation errors, and slow feedback may lead to unacceptable position errors under such conditions. Use of IMU data, selective wave filtering, stronger feedback and feed-forward from predicted external forces can improve DP performance. The overall objective is to evaluate these opportunities.

Tasks

1. Study alternative concepts for handling of external forces, considering feedback, sensors, filtering and feed-forward elements. Consider scenarios related to DP in ice.
2. Investigate possible modifications to the DP controller, such as stronger feedback, selective wave filtering, feed-forward from measured and predicted external forces.
3. Implement the controller in Simulink, and evaluate its performance in closed loop. Compare with existing solutions.
4. Implement the controller in MT's DP simulator, and compare with existing controller.

Start date:	2013-09-15
Due date:	2014-02-21

Thesis performed at:	Department of Engineering Cybernetics, NTNU
Supervisor:	Professor Tor Arne Johansen, Dept. of Eng. Cybernetics, NTNU
Co-supervisor:	Professor Thor I. Fossen, Dept. of Eng. Cybernetics, NTNU

Abstract

Rising marine activity in the arctic has introduced many ice related challenges for Dynamically Positioned (DP) marine vessels. Current motion control systems for DP vessels are not designed to handle ice-related disturbances, and will thus need to be improved to be able to operate in these challenging conditions.

The main goals of this master thesis have been to evaluate opportunities for handling large and sudden unknown external disturbances, and compare these with existing solutions.

There will be presented a predictive feedforward controller to minimize the impact of an external disturbance. There will also be presented a selective wave filter with a notch frequency that is adapted by a wave-frequency tracker.

A modified highly responsive PID controller with nonlinear stiffness and damping terms is derived, and proven globally asymptotically stable using Lyapunov based stability analysis. There will also be presented a Disturbance Rejection by Acceleration Feedforward controller that utilizes acceleration feedback from inertial measurements.

All of the proposed improvements have been implemented and tested in Matlab/Simulink, while some of the methods have been implemented and tested hardware-in-the-loop in a simulator provided by Marine Technologies. The proposed methods were shown both theoretically and through simulations to yield improved station-keeping performances.

Sammendrag

Økt maritim aktivitet i arktis har introdusert mange is-relaterte utfordringer for Dynamisk Posisjonerte (DP) marine fartøy. Nåværende regulatorsystemer for DP fartøy er ikke designet for å takle is-relaterte forstyrrelser, og vil derfor trenge forbedringer for å ha mulighet til å operere i de vanskelige forholdene.

Hovedmålene i denne masteroppgaven har vært å evaluere mulighetene for å takle store og plutselige ukjente eksterne forstyrrelser, samt og sammenligne disse med eksisterende løsninger.

Det vil bli presentert en prediktiv foroverkoblet regulator for å minimere sammenstøtet av en ekstern forstyrrelse. Det vil også bli presentert et selektivt bølgefilter med en notch-frekvens som er adaptert av en bølge-frekvens måler.

En modifisert svært responderende PID-regulator med ulineær stivhet og demping er utledet, og bevist globalt asymptotisk stabil ved bruk av Lyapunov-basert stabilitetsanalyse. Det vil også bli presentert en forstyrrelsesavvisende regulator med akselerasjons-foroverkobling som tar nytte av en akselerasjons-tilbakekobling fra treghetsmålinger.

Alle foreslåtte forbedringer har blitt implementert og testet i Matlab/Simulink, mens noen av metodene har blitt implementert og testet "hardware-in-the-loop" i en simulator levert av Marine Technologies. De foreslåtte metodene ble vist å gi forbedrede posisjonerings-prestasjoner, både teoretisk og gjennom simuleringer.

Acknowledgements

This thesis is submitted as the finalization of the Master of Science in Engineering Cybernetics program at the Norwegian University of Science and Technology. The work presented in this thesis has been performed during the fall of 2013, and the winter of 2014.

First of all, I would like to give special thanks my supervisor Tor Arne Johansen for inspiring meetings and excellent guidance whenever needed. I would also like to thank my co-supervisor Thor Inge Fossen for feedback provided throughout the last year.

This thesis has been conducted in collaboration with Marine Technologies LLC. I would like to thank Tore Flobakk for implementing the control strategies proposed in this thesis on the MT simulator. I would also like to thank Marine Technologies for support and for giving me the opportunity to perform this thesis.

Last, but not least, I would like to thank my friends and family for their support throughout this last year. I would also like to thank my office colleagues for providing a good working environment. That includes a special thanks to Tor Eirik Østrem, fellow student and best friend.

Christoffer Andreas Ofstad
Trondheim, February 21, 2014.

Contents

List of Abbreviations and Acronyms

AFB	Acceleration Feedback
AFF	Acceleration Feedforward
AoI	Angle of Impact
AUV	Autonomous Underwater Vehicle
BOA	Breadth Overall
CC	Control Computer
CG	Center of Gravity
CO	Center of Origin
CSV	Comma-Separated Value
DOF	Degree of Freedom
DP	Dynamic Positioning
GAS	Global Asymptotic Stability
HIL	Hardware-in-the-Loop
IMU	Inertial Measurement Unit
IR	Infrared
ISE	Integral Square Error
ISO	Integral Square Output
LAS	Local Asymptotic Stability
LOA	Length Overall
LOS	Line-of-Sight
LF	Low-Frequency
MIMO	Multiple-Input Multiple-Output
MSS	Marine Systems Simulator
MT	Marine Technologies
NED	North-East-Down
OS	Operator Station
PID	Proportional-Integral-Derivative
RCN	Research Council of Norway
RAO	Response Amplitude Operator
UAV	Unmanned Aerial Vehicle
UDP	User Datagram Protocol
UUB	Uniformly Ultimately Bounded
WF	Wave-Frequency

List of Figures

List of Tables

Chapter 1

Introduction

Due to the rising global demand for energy, the oil and gas development has been driven into the arctic region. Global climate changes have also led to increased arctic ship traffic, research and tourism.

The harsh arctic climate and ice-infested waters make ship operations hazardous and more complex. These operations include, but are not limited to: dynamic positioning, towing, drilling and transit. Additional factors such as remoteness, winter darkness and fog make these operations even more challenging.

1.1 Background and Motivation

Dynamic Positioning (DP) of marine vessels is a challenging practical problem, where the main purpose is to control and maintain the vessel position and heading within some accuracy, by the sole use of its propulsion and navigation systems [2]. DP operations include, but are not limited to: stationkeeping, position mooring and low speed reference tracking. DP control systems were first commercially utilized in the 1960s petroleum industry, and have been experiencing significant improvements up to this date [3]. Advanced multivariable optimal control and Kalman filtering techniques were proposed in the 1970s by [4], and this work was later modified and extended by [5][6][7][8] and more recently by [9]. These days, DP systems are in addition to oil and gas applications, used in many other marine operations such as cable-laying, cruise ships, flotels and even yachts.

With the increasing interest in arctic marine operations, new ships are being designed and built in order to meet the demands for efficiency, survivability and operability related to the challenging conditions. In arctic waters, there are even higher standards for safety and environmental protection related to petroleum production, so there is clearly a gap that needs to be closed [10]. This motivates for the exploration of stationkeeping applications in various ice conditions.

Traditional DP systems are designed to operate up to certain limitations with

regards to environmental conditions, limited by power and actuation capacities [11]. These conditions however, are related to open water phenomena. Due to the nature of ice related external forces, the environmental loads arising in arctic waters are very different from those in open waters, but unfortunately, few full scale experiments have been reported to this regard [3]. A general opinion is that current DP systems designed for open water applications, are not adequately capable of handling ice related disturbances [12][13][14]. Several projects have thus recently been launched to address this matter. Examples include the Research Council of Norway (RCN) project: *"Arctic DP: Safe and Green Dynamic Positioning Operations of Offshore Vessels in an Arctic Environment"* [15], which seeks to increase knowledge and competence related to offshore stationkeeping operations in arctic ice-infested waters, and the DYPIC project [16], which involved large ice tank experiments. The DYPIC project also explored the comprehension of ice interactions on DP vessels, which was found to be of crucial importance for stationkeeping performances in arctic conditions.

In the presence of level ice, [17] proposes a DP control design based on an ice-load model. However, a more realistic scenario is where the DP vessel operates in a combination of open and ice infested waters, or in managed ice [11]. According to [18], managed ice can be considered to be the most likely operating condition for DP vessels in the arctic. Managed ice is the result of *ice management*, which is defined by [19] as *"... the sum of all activities where the objective is to reduce or avoid actions from any kind of ice features"*. This includes, but is not limited to: physical ice management in terms of ice breaking or iceberg towing; threat evaluation; and detection, tracking and forecasting of sea ice. The latter term requires *ice intelligence*, which is the process of collecting and analyzing relevant information about the ice environment [20]. For a complete ice intelligence system, several sensor platforms are needed to obtain sufficient ice information, as no single ice observation system will suffice [21]. Ice observation systems can be found in the works by [22], where autonomous underwater vehicles (AUVs) are considered as mobile sensor platforms for underwater ice observation, or in [20], where studies on aerial ice observation by the use of unmanned aerial vehicles (UAVs) are presented. The results from several such ice observation systems are necessary for the determination and compensation of ice loads, as well as for decision support and risk assessment in arctic operations [18]. This would also tend toward robust solutions, with regards to the redundancy insured by several sensory platforms [20]. As proposed in [23], ice observation systems can be used to predict short-term ice load changes, and use these predictions to pro-actively generate thruster forces in order to minimize the impact of the disturbance.

As managed ice also will experience patches of open water, there will be a need to consider DP designs that perform well in combinations of open and ice-infested waters [11]. [24] proposes to ignore the use of wave filtering when the vessel is subjected to ice, but due to the changing conditions, some form of switching would be a better approach. [11] suggests the use of hybrid control to switch between controllers and control settings, but stability may become a concern when non-

linear controllers are involved. A better approach may be to utilize acceleration measurements from Inertial Measurement Units (IMUs), which are becoming more available at low cost and with high quality. According to [25], acceleration feedback can be used for better compensation of external forces, without compromising thruster usage. The use of IMU measurements has also been encouraged by [26], who addresses environmental disturbance rejection by the use of acceleration feedforward, with promising results with regards to arctic operations. This approach virtually cancels out disturbances, leaving the underlying controller to experience a calm sea state, and thus making it a favorable approach for constantly changing arctic conditions.

The main motivation of this thesis was to explore methods for improved handling of sudden and unknown external disturbances, for the purpose of achieving more robust and accurate dynamic positioning in ice-infested waters. This includes the use of inertial measurements, issues related to wave filtering in ice, and short-term prediction of external forces caused by ice loads.

As real-life applications are time consuming as well as very expensive, it is desirable to test proposed designs in a simulator such as Simulink. Since practical performances rarely match the theoretical, it is imperative to have the opportunity to run numerous simulations with an easily modifiable design, [27].

1.2 Contribution

This master thesis shall provide the following contributions:

- A study on inertial measurements with accompanying theoretical examples.
- A nonlinear multivariable PID controller augmented with nonlinear stiffness and damping terms, with corresponding Lyapunov stability analysis.
- A Disturbance Rejection by Acceleration Feedforward controller.
- A predictive feedforward controller.
- A selective adaptive wave filter.
- Simulations of all proposed methods in Simulink and hardware-in-the-loop simulations of selected methods.

Although the main focus of this thesis has been on ice-related challenges, the proposed methods are also applicable to handle other unknown or poorly modeled external disturbances related to e.g. cable-laying, pipe-laying or seismic tracking operations.

The consideration of thruster use corresponding to eventual position performance improvements has also been taken, both in the interest of reducing cost and maintenance related to wear and tear, as well as the environmental impact of fuel consumption.

1.3 Outline

This thesis is organized in 9 chapters and 4 appendices. The chapters are numbered 1 through 9 while the appendices are numbered A through D. The appendix presents nonlinear stability theory, modeling of the vessel used in Simulink simulations, a description of the attached Matlab files, and additional results and plots. The content of the chapters is described as follows:

Chapter 2 presents the notation used throughout this thesis, and studies kinetic and kinematic equations of motion describing a marine vessel.

Chapter 3 presents a brief study on the possible advantages of utilizing inertial measurements.

Chapter 4 presents an augmented PID controller design and the corresponding stability properties. A Disturbance Rejection by Acceleration Feedforward controller design is also presented.

Chapter 5 presents the design of a predictive feedforward controller as well as simulation results.

Chapter 6 presents a selective adaptive wave filter design and corresponding simulations.

Chapter 7 presents the simulation results of several case studies involving different external disturbances.

Chapter 8 gives a general discussion of the results in this thesis.

Chapter 9 gives a conclusion on the results, and suggests future work.

Chapter 2

Vessel Modeling

The purpose of this chapter is to study the kinematic and kinetic equations of motion describing a marine vessel. The 6 DOF equations of motion will be derived from first principles. The notation and results presented in this chapter are mainly based on [1].

2.1 Notation and Reference Frames

2.1.1 Reference Frames

To describe the vessel kinematics in 6 DOF, several reference frames are needed, [1]. The following definitions are obtained from [1] and [25]:

NED: The North-East-Down coordinate system $\{n\} = (x_n, y_n, z_n)$ has the origin fixed at an arbitrarily chosen point on the Earth's surface, where the x axis points true North, the y axis points East and the z axis points Downwards normal to the Earth's surface. Throughout this thesis, this coordinate system is chosen as the inertial reference frame.

BODY: The body-fixed coordinate system $\{b\} = (x_b, y_b, z_b)$ has the origin fixed in the vessel center of origin that coincides with the principal axes of inertia, where the x axis points in the longitudinal direction, the y axis points in the lateral direction and the z axis points normal to the xy plane, [1]. The x, y and z axes are positive in the forward, right and downwards directions, respectively.

Reference-parallel: The reference-parallel coordinate system $\{d\} = (x_d, y_d, z_d)$ is the BODY frame rotated an angle ψ_d about z_b, where ψ_d is the desired angle specified by the user or by a reference model.

Body-fixed reference points

CO: Center of origin, i.e. the origin of the BODY coordinate system.

CG: Center of gravity, i.e. the point where the gravitational forces are considered to act on the body.

2.1.2 Notation of Marine Vessel State-Space Vectors

To describe forces and moments, velocities, positions and angles, the following table is adopted from [1]:

DOF	Description	Forces and moments	Linear and angular velocities	Positions and Euler angles
1	Motions in the x direction (surge)	X	u	N
2	Motions in the y direction (sway)	Y	v	E
3	Motions in the z direction (heave)	Z	w	D
4	Rotation about the x axis (roll)	K	p	ϕ
5	Rotation about the y axis (pitch)	M	q	θ
6	Rotation about the z axis (yaw)	N	r	ψ

Table 2.1.1: The notation for vessel forces, moments, velocities, positions and angles [1].

Note that the notation N is mentioned twice, for the yaw moment and the x position in NED frame, respectively, but they will not be used in a context where confusion could arise about which one is being referred to.

2.1.3 Vectorial Notation of Marine Vessel in 6 DOF

For marine craft, the following notation will be used for vectors in the BODY and NED frames [1]:

$\boldsymbol{v}_{b/n}^{b} = \begin{bmatrix} u \\ v \\ w \end{bmatrix}$, linear velocity of origin of $\{b\}$ with respect to $\{n\}$ expressed in $\{b\}$ [m/s]

$\boldsymbol{\omega}_{b/n}^{b} = \begin{bmatrix} p \\ q \\ r \end{bmatrix}$, angular velocity of $\{b\}$ with respect to $\{n\}$ expressed in $\{b\}$ [rad/s]

$\boldsymbol{p}_{b/n}^{n} = \begin{bmatrix} N \\ E \\ D \end{bmatrix}$, NED position of $\{b\}$ with respect to $\{n\}$ expressed in $\{n\}$ [m]

$\boldsymbol{p}_{b/n}^{b} = \begin{bmatrix} x \\ y \\ z \end{bmatrix}$, BODY position of $\{b\}$ with respect to $\{n\}$ expressed in $\{b\}$ [m]

$\boldsymbol{f}_{b}^{b} = \begin{bmatrix} X \\ Y \\ Z \end{bmatrix}$, force with line of action through origin of $\{b\}$ expressed in $\{b\}$ [N]

$\boldsymbol{m}_{b}^{b} = \begin{bmatrix} K \\ M \\ N \end{bmatrix}$, moment about the origin of $\{b\}$ expressed in $\{b\}$ [Nm]

$\boldsymbol{\Theta}_{nb} = \begin{bmatrix} \phi \\ \theta \\ \psi \end{bmatrix}$, Euler angles between $\{n\}$ and $\{b\}$ [rad]

$\boldsymbol{r}_{g}^{b} = \begin{bmatrix} x_g \\ y_g \\ z_g \end{bmatrix}$, vector from origin of $\{b\}$to CG expressed in $\{b\}$ [m]

2.2 Kinematics

To transform between different coordinate systems, a rotation matrix R is introduced in [1] with the properties

$$\boldsymbol{R}\boldsymbol{R}^{T} = \boldsymbol{R}^{T}\boldsymbol{R} = \boldsymbol{I} \Leftrightarrow \boldsymbol{R}^{-1} = \boldsymbol{R}^{T} \tag{2.1}$$

$$\det\boldsymbol{R} = 1 \tag{2.2}$$

where $\boldsymbol{R} \in \mathrm{SO}(3)$, i.e. the special orthogonal group of order 3.

A rotation from frame a to frame b can then be expressed as

$$\boldsymbol{v}^{b} = \boldsymbol{R}_{a}^{b}\boldsymbol{v}^{a} \tag{2.3}$$

This transformation can now be used to rotate the body-fixed velocity into the NED-reference frame, such that

$$\boldsymbol{v}_{b/n}^{n} = \boldsymbol{R}_{b}^{n}(\boldsymbol{\Theta}_{nb})\boldsymbol{v}_{b/n}^{b} \tag{2.4}$$

where $\boldsymbol{R}_{b}^{n}(\boldsymbol{\Theta}_{nb})$ represents three successive principal rotations about the the z, y and x axis, i.e.

$$\boldsymbol{R}_{b}^{n}(\boldsymbol{\Theta}_{nb}) = \boldsymbol{R}_{z,\psi}\boldsymbol{R}_{y,\theta}\boldsymbol{R}_{x,\phi} \tag{2.5}$$

and its inverse

$$\boldsymbol{R}_b^n(\boldsymbol{\Theta}_{nb})^{-1} = \boldsymbol{R}_n^b(\boldsymbol{\Theta}_{nb}) = \boldsymbol{R}_{x,\phi}\boldsymbol{R}_{y,\theta}\boldsymbol{R}_{z,\psi} \tag{2.6}$$

where, using the notation $s\cdot = \sin(\cdot)$ and $c\cdot = \cos(\cdot)$, the principal rotations are given as

$$\boldsymbol{R}_{x,\phi} = \begin{bmatrix} 1 & 0 & 0 \\ 0 & c\phi & -s\phi \\ 0 & s\phi & c\phi \end{bmatrix} \boldsymbol{R}_{y,\theta} = \begin{bmatrix} c\theta & 0 & s\theta \\ 0 & 1 & 0 \\ -s\theta & 0 & c\theta \end{bmatrix} \boldsymbol{R}_{z,\psi} = \begin{bmatrix} c\psi & -s\psi & 0 \\ s\psi & c\psi & 0 \\ 0 & 0 & 1 \end{bmatrix} \tag{2.7}$$

such that $\boldsymbol{R}_b^n(\boldsymbol{\Theta}_{nb})$ becomes

$$\boldsymbol{R}_b^n(\boldsymbol{\Theta}_{nb}) = \begin{bmatrix} c\psi c\theta & -s\psi c\phi + c\psi s\theta s\phi & s\psi s\phi + c\psi c\phi s\theta \\ s\psi c\theta & c\psi c\phi + s\phi s\theta s\psi & -c\psi s\phi + s\theta s\psi c\phi \\ -s\theta & c\theta s\phi & c\theta c\phi \end{bmatrix} \tag{2.8}$$

2.3 Equations of Motion

2.3.1 Kinematic Equations of Motion

The kinematic equations for marine craft can be described as translational and rotational motions of a fixed body with respect to the NED frame, and can be expressed in terms of the Euler angles, [1]. The kinematic equation for translation is given in (2.4), and can be expressed in component form as

$$\begin{bmatrix} \dot{N} \\ \dot{E} \\ \dot{D} \end{bmatrix} = \boldsymbol{R}_{z,\psi}\boldsymbol{R}_{y,\theta}\boldsymbol{R}_{x,\phi} \begin{bmatrix} u \\ v \\ w \end{bmatrix} \tag{2.1}$$

where $\boldsymbol{R}_{z,\psi}$, $\boldsymbol{R}_{y,\theta}$, and $\boldsymbol{R}_{x,\phi}$ are the Euler angle rotational matrices about the z, y and x axis, respectively, [1].

The kinematic equations for rotation, i.e. attitude, are given by [1] as the relationship between the body-fixed angular velocity vector $\boldsymbol{\omega}_{b/n}^b$ and the Euler rate vector $\dot{\boldsymbol{\Theta}}_{nb}$ transformed by the transformation matrix $\boldsymbol{T}_\Theta(\boldsymbol{\Theta}_{nb}) \in \mathbb{R}^{3\times3}$, such that

$$\dot{\boldsymbol{\Theta}}_{nb} = \boldsymbol{T}_\Theta(\boldsymbol{\Theta}_{nb})\boldsymbol{\omega}_{b/n}^b \tag{2.2}$$

The transformation matrix $\boldsymbol{T}_\Theta(\boldsymbol{\Theta}_{nb})$ can be found by

$$\boldsymbol{\omega}_{b/n}^b = \begin{bmatrix} \dot{\phi} \\ 0 \\ 0 \end{bmatrix} + \boldsymbol{R}_{x,\phi}^T \begin{bmatrix} 0 \\ \dot{\theta} \\ 0 \end{bmatrix} + \boldsymbol{R}_{x,\phi}^T\boldsymbol{R}_{y,\theta}^T \begin{bmatrix} 0 \\ 0 \\ \dot{\psi} \end{bmatrix} := \boldsymbol{T}_\Theta^{-1}(\boldsymbol{\Theta}_{nb})\dot{\boldsymbol{\Theta}}_{nb} \tag{2.3}$$

which gives

$$\boldsymbol{T}_\Theta(\boldsymbol{\Theta}_{nb}) = \begin{bmatrix} 1 & s\phi t\theta & c\phi t\theta \\ 0 & c\phi & -s\phi \\ 0 & s\phi/c\theta & c\phi/c\theta \end{bmatrix} \tag{2.4}$$

where $s\cdot = \sin(\cdot)$, $c\cdot = \cos(\cdot)$, $t\cdot = \tan(\cdot)$. There is a singularity in $\theta = \pm 90°$, but this is not a problem for surface vessels. For underwater vehicles operating near this singularity, the use of unit quaternions to represent attitude would avoid this problem at the cost of a fourth parameter.

The kinematic equations can now be expressed in vector form by introducing the Earth-fixed position and orientation vector $\boldsymbol{\eta}$ and the body-fixed velocity vector $\boldsymbol{\nu}$, as

$$\boldsymbol{\eta} = \begin{bmatrix} \boldsymbol{p}_{b/n}^{n} \\ \boldsymbol{\Theta}_{nb} \end{bmatrix} \tag{2.5}$$

and

$$\boldsymbol{\nu} = \begin{bmatrix} \boldsymbol{v}_{b/n}^{b} \\ \boldsymbol{\omega}_{b/n}^{b} \end{bmatrix} \tag{2.6}$$

The kinematic equations then becomes [1]

$$\dot{\boldsymbol{\eta}} = \boldsymbol{J}_{\Theta}(\boldsymbol{\eta})\boldsymbol{\nu} \tag{2.7}$$

where

$$\boldsymbol{J}_{\Theta}(\boldsymbol{\eta}) = \begin{bmatrix} \boldsymbol{R}_{b}^{n}(\boldsymbol{\Theta}_{nb}) & \boldsymbol{0}_{3\times 3} \\ \boldsymbol{0}_{3\times 3} & \boldsymbol{T}_{\Theta}(\boldsymbol{\Theta}_{nb}) \end{bmatrix} \tag{2.8}$$

2.3.2 Rigid-Body Kinetic Equations of Motion

The rigid-body equations of motion can be written as [28][1]

$$\boldsymbol{M}\dot{\boldsymbol{\nu}} + \boldsymbol{C}_{RB}(\boldsymbol{\nu})\boldsymbol{\nu} + \boldsymbol{C}_{A}(\boldsymbol{\nu}_r)\boldsymbol{\nu}_r + \boldsymbol{D}(\boldsymbol{\nu}_r)\boldsymbol{\nu}_r + \boldsymbol{G}(\boldsymbol{\eta}) = \boldsymbol{\tau}_{thr} + \boldsymbol{\tau}_{env} \tag{2.9}$$

where $\boldsymbol{M} \in \mathbb{R}^{6\times 6}$ is the inertia matrix, $\boldsymbol{C}_{RB}(\boldsymbol{\nu}) \in \mathbb{R}^{6\times 6}$ and $\boldsymbol{C}_{A}(\boldsymbol{\nu}_r) \in \mathbb{R}^{6\times 6}$ are the skew-symmetrical Coriolis and centripetal matrices of the rigid body and added mass, respectively, $\boldsymbol{D}(\boldsymbol{\nu}_r) \in \mathbb{R}^{6\times 6}$ is the damping matrix consisting of both linear potential damping and nonlinear viscous damping, $\boldsymbol{G}(\boldsymbol{\eta}) \in \mathbb{R}^{6}$ is the restoring force vector consisting of buoyancy and gravitational forces, $\boldsymbol{\tau}_{thr} \in \mathbb{R}^{6}$ is the controlled force vector produced by the thruster system, and $\boldsymbol{\tau}_{env} \in \mathbb{R}^{6}$ are the environmental forces caused by external disturbances such as e.g. wind, waves and ice. $\boldsymbol{\nu}_r$ is the relative velocity vector given in [28] as

$$\boldsymbol{\nu}_r = \begin{bmatrix} u - u_c \\ v - v_c \\ w \\ p \\ q \\ r \end{bmatrix} \tag{2.10}$$

where the horizontal current components u_c and v_c in surge and sway, respectively, are defined in [28] as

$$u_c := V_c cos(\beta_c - \psi), \qquad v_c := V_c sin(\beta_c - \psi) \tag{2.11}$$

where V_c and β_c are the current velocity and direction, respectively.

Rigid-body and Added Mass

The mass matrix is given in [1] as

$$\boldsymbol{M} = \boldsymbol{M}_{RB} + \boldsymbol{M}_A \tag{2.12}$$

where $\boldsymbol{M}_A$ is the hydrodynamic added mass and $\boldsymbol{M}_{RB}$ is the rigid-body mass given by [1] as

$$\boldsymbol{M}_{RB} = \begin{bmatrix} m\boldsymbol{I}_{3\times 3} & -m\boldsymbol{S}(\boldsymbol{r}_g^b) \\ m\boldsymbol{S}(\boldsymbol{r}_g^b) & \boldsymbol{I}_b \end{bmatrix} \tag{2.13}$$

where m is the mass and where

$$\boldsymbol{I}_b = \boldsymbol{I}_g - m\boldsymbol{S}^2(\boldsymbol{r}_g^b) \tag{2.14}$$

where $\boldsymbol{I}_g$ is the inertia dyadic about CG, defined as

$$\boldsymbol{I}_g := \begin{bmatrix} I_x & -I_{xy} & -I_{xz} \\ -I_{yx} & I_y & -I_{yz} \\ -I_{xz} & -I_{zy} & I_z \end{bmatrix} \tag{2.15}$$

and where $\boldsymbol{S} \in SS(3)$ is defined in [1] as

$$\boldsymbol{S}(\boldsymbol{\lambda}) = -\boldsymbol{S}^T(\boldsymbol{\lambda}) = \begin{bmatrix} 0 & -\lambda_3 & \lambda_2 \\ \lambda_3 & 0 & -\lambda_1 \\ -\lambda_2 & \lambda_1 & 0 \end{bmatrix}, \ \boldsymbol{\lambda} = \begin{bmatrix} \lambda_1 \\ \lambda_2 \\ \lambda_3 \end{bmatrix} \tag{2.16}$$

Damping Forces

The damping matrix $\boldsymbol{D}(\boldsymbol{\nu}_r)$ can be expressed as the sum of linear damping forces, $\boldsymbol{D}_L$, and nonlinear damping forces, $\boldsymbol{D}_N(\boldsymbol{\nu}_r)$, such as viscous forces and wave drift. The linear damping can be regarded as proportional to the velocity, while the nonlinear damping can be assumed to be proportional to the square of the velocity [25]. Marine vessels operating at low velocities will thus experience that linear damping forces are dominating.

2.4 3 DOF Model

For positioning of conventional marine vessels it is normal to neglect the vertical motion and only control the horizontal plane [28]. That means that only vessel dynamics in surge, sway and yaw are considered, and thus the vessel model is reduced from 6 DOF to 3 DOF. This is done by neglecting every vertical component and thus letting $w = p = q = 0$, and reducing the position/orientation and velocity vectors to $\boldsymbol{\eta} = [x, y, \psi]^T$ and $\boldsymbol{\nu} = [u, v, r]^T$, respectively. The 3 DOF model then becomes

$$\begin{aligned} \dot{\boldsymbol{\eta}} &= \boldsymbol{R}(\psi)\boldsymbol{\nu} \\ \boldsymbol{M}\dot{\boldsymbol{\nu}} + \boldsymbol{C}_{RB}(\boldsymbol{\nu})\boldsymbol{\nu} + \boldsymbol{C}_A(\boldsymbol{\nu}_r)\boldsymbol{\nu}_r + \boldsymbol{D}(\boldsymbol{\nu}_r)\boldsymbol{\nu}_r &= \boldsymbol{\tau}_{thr} + \boldsymbol{\tau}_{env} \end{aligned} \tag{2.1}$$

where $\boldsymbol{R}(\psi)$ is the principal rotation about the z axis given in (2.7). To further simplify the 3 DOF model, the following assumptions are made [1]:

1. The vessel is rigid.
2. The NED frame $\{n\}$ is inertial.
3. The vessel is symmetric in the xz plane.
4. The $\{b\}$ frame originates in the centerline of the vessel.

The first assumption implies that all structural points on the vessel remain fixed in time. The second assumption implies that the forces caused by the Earth's rotation can be neglected. The third assumption implies that the products of inertia about the xz plane equals zero, i.e. $I_{xy} = I_{yz} = 0$. The fourth assumption implies that $y_g = 0$.

The mass matrix then simplifies to

$$\boldsymbol{M}_{RB} = \begin{bmatrix} m & 0 & 0 \\ 0 & m & mx_g \\ 0 & mx_g & I_z \end{bmatrix} \tag{2.2}$$

and the added mass matrix to

$$\boldsymbol{M}_A = \begin{bmatrix} -X_{\dot{u}} & 0 & 0 \\ 0 & -Y_{\dot{v}} & -Y_{\dot{r}} \\ 0 & -N_{\dot{v}} & -N_{\dot{r}} \end{bmatrix} \tag{2.3}$$

such that

$$\boldsymbol{M} = \boldsymbol{M}_{RB} + \boldsymbol{M}_A = \begin{bmatrix} m - X_{\dot{u}} & 0 & 0 \\ 0 & m - Y_{\dot{v}} & mx_g - Y_{\dot{r}} \\ 0 & mx_g - N_{\dot{v}} & I_z - N_{\dot{r}} \end{bmatrix} \tag{2.4}$$

Notice that surge is decoupled from sway and yaw due to the symmetry about the xz plane.

The total Coriolis and centripetal matrix $\boldsymbol{C}(\boldsymbol{\nu}, \boldsymbol{\nu}_r)$ can now be expressed as

$$\boldsymbol{C}(\boldsymbol{\nu}, \boldsymbol{\nu}_r) \quad = \quad \boldsymbol{C}_{RB}(\boldsymbol{\nu}) + \boldsymbol{C}_A(\boldsymbol{\nu}_r) \tag{2.5}$$

where

$$\boldsymbol{C}_{RB}(\boldsymbol{\nu}) = \begin{bmatrix} 0 & 0 & -m(x_g r + v) \\ 0 & 0 & mu \\ m(x_g r + v) & -mu & 0 \end{bmatrix} \tag{2.6}$$

and

$$\boldsymbol{C}_A(\boldsymbol{\nu}_r) = \begin{bmatrix} 0 & 0 & Y_{\dot{r}} r + Y_{\dot{v}} v_r \\ 0 & 0 & -X_{\dot{u}} u_r \\ -Y_{\dot{r}} r - Y_{\dot{v}} v_r & X_{\dot{u}} u_r & 0 \end{bmatrix} \tag{2.7}$$

The linear damping matrix becomes

$$\boldsymbol{D}_L = \begin{bmatrix} -X_u & 0 & 0 \\ 0 & -Y_v & -Y_r \\ 0 & -N_v & -N_r \end{bmatrix} \tag{2.8}$$

2.4.1 DP Model

For dynamic positioning of marine vessels, one often assumes low speed conditions as DP is used for stationkeeping and low-speed maneuvering (up to about 2 m/s) [29]. Therefore a low-speed 3 DOF DP model can be derived. Assuming that roll and pitch angles are small [1], the 3 DOF model (2.1) can be linearized around $\boldsymbol{\nu} \approx 0$, which implies that the nonlinear Coriolis, centripetal, restoring, damping and buoyancy forces and moments can be linearized about $\boldsymbol{\nu} = 0$ and $\phi = \theta = 0$. The DP model can then be expressed as

$$\begin{aligned} \dot{\boldsymbol{\eta}} &= \boldsymbol{R}(\psi)\boldsymbol{\nu} \\ \boldsymbol{M}\dot{\boldsymbol{\nu}} + \boldsymbol{D}\boldsymbol{\nu}_r &= \boldsymbol{\tau} + \boldsymbol{R}^T(\psi)\boldsymbol{b} \end{aligned} \tag{2.9}$$

where $\boldsymbol{D} = \boldsymbol{D}_L$, $\boldsymbol{\tau} = \begin{bmatrix} \tau_x & \tau_y & \tau_\psi \end{bmatrix}^T$ is the control vector and $\boldsymbol{b} \in \mathbb{R}^3$ is the bias vector consisting of unknown forces and moments caused by e.g. wave drift, ice and unmodeled dynamics.

2.5 Actuator Dynamics

As opposed to the ideal case, where thrust is applied at the instant it is requested, the actuators have their own dynamics with regards to rate limits and total effect. This introduces a phase lag and reduced amplitude with respect to the commanded signals. According to [30], the actuator dynamics can conveniently be modeled with a first-order approximation that satisfyingly reflects realistic behavior. The actuator model is given as [30]

$$\dot{\boldsymbol{\tau}} = -\boldsymbol{A}\left(\boldsymbol{\tau} - \boldsymbol{\tau}_c\right) \tag{2.1}$$

where $\boldsymbol{\tau}$ is the actual applied thrust vector, while $\boldsymbol{\tau}_c$ is the thrust vector requested by the controller. The thruster dynamics matrix $\boldsymbol{A}$ is given as $\boldsymbol{A} = \text{diag}\left(\begin{bmatrix} 1/T_1 & 1/T_2 & 1/T_3 \end{bmatrix}\right)$, where $T_{1,2,3}$ represent the time constants for surge, sway sand yaw, respectively. This model will limit the rate of which the trust can change, while it does not limit the maximal thrust in each DOF. A saturation term is therefore added, such that the applied thrust vector becomes

$$\boldsymbol{\tau} = \begin{cases} \boldsymbol{\tau} & \text{if } |\boldsymbol{\tau}| < \boldsymbol{\tau}_{max} \\ \boldsymbol{\tau}_{max} & \text{else} \end{cases} \tag{2.2}$$

where the determination of $\boldsymbol{\tau}_{max}$ is discussed in Appendix B.

2.6 Environmental Forces and Moments

Environmental forces and moments normally represent wind, waves and ocean currents. However, as this thesis focuses on sudden and unknown external forces, wind and current models will not be discussed. Even though wind forces account for a large proportion of the environmental disturbance due to the vessels large surface area, both current and wind forces can be considered as constant or slowly varying, and will thus be handled by integral action and or wind feedforward control, respectively. Gusty winds will not affect the vessel due to its large inertia [1].

2.6.1 Wave Forces and Moments

Wave forces are one the most influencing forces on a controlled marine vessel [31], not necessarily in magnitude, but in frequency. The wave-induced forces can be divided into first and second-order forces, where the second-order forces are slowly varying drift forces, while the first-order are rapid oscillatory zero-mean wave-frequency (WF) motions [1]. As the second-order forces are slowly varying, they can be attenuated by integral action, and will thus not be modeled in this thesis. The first-order forces, however, have great influence on the control system due to its high-frequency rapid motion. To evaluate the performance and robustness of the DP controller, the first-order wave-forces must thus be included in the model. According to [1], response amplitude operators (RAOs) can be used to compute the wave-induced force vector.

To utilize the RAOs, a wave spectrum must be introduced, where the JONSWAP spectrum was chosen as it has been adopted as the industry standard [1]. The JONSWAP spectrum can conveniently be approximated by a second-order transfer function, given in one DOF as [1]

$$h(s) = \frac{2\lambda\omega_0\sigma s}{s^2 + 2\lambda\omega_0 s + \omega_0^2} \tag{2.1}$$

where λ is a damping coefficient, σ represents the wave intensity, while ω_0 is the dominating wave-frequency. The values for λ and σ can be found by the *wavespec.m* function in the MSS toolbox [32], which takes in ω_0 and H_s as parameters. H_s represents the significant wave height, which is the mean of the one-third highest waves.

The force RAO can now be utilized by approximating the first-order wave-induced forces $\boldsymbol{\tau}_{wave}$ by the linear approximation [1]

$$\boldsymbol{\tau}_{wave} \approx \boldsymbol{K}\boldsymbol{H}(s)\boldsymbol{w}(s)$$

where $\boldsymbol{H}(s)$ is a diagonal matrix consisting of the second-order wave transfer function approximation for each DOF, $\boldsymbol{w}(s)$ is a zero-mean Gaussian white noise process and spectral density $P_{ww}(w) = 1$, and $\boldsymbol{K}$ is a tunable constant gain matrix that should be tuned such that the effect the wave forces have on $\boldsymbol{\eta}$, becomes reasonable.

Chapter 3

Inertial Measurements

3.1 Introduction

Today's conventional DP control systems typically consist of Kalman filters, and PID or optimal control strategies to control the position and velocity of the vessel [26]. The common scheme is to only use measurements of the position and velocity states, while acceleration measurements are not used. These strategies are model-based, and separate the fast-varying first order wave disturbances from the slowly-varying forces such as nonlinear wave drift, ocean currents, wind and ice. The desired thrust is then calculated from the low-frequency (LF) estimates to reduce wear and tear of the actuators and rudders, as the oscillatory zero mean wave motions have been filtered out. The DP system thus only reacts to constant and slowly-varying disturbances, although it should be mentioned that some high-frequency oscillatory wave components will always find its way into the feedback loop. When the varying disturbances are measurable, it is desirable to use disturbance feed-forward to cancel them out. However, most disturbances are not measurable and must be handled by other means. Wind is the only disturbance that is relatively easy to measure and requiring that the vessel's wind coefficients are well known, the wind force can be estimated by the use of wind sensor measurements. Wind feed-forwarding is thus commonly implemented on conventional DP systems [25].

Conventional DP control systems are usually proved stable and robust, but they do not necessarily provide adequate compensation of environmental disturbances [26]. This especially applies when these disturbances are unknown external forces, such as ice loads or cables. A PID control system will efficiently handle constant disturbances, but will use unnecessary thruster power as momentum needs to build up before the controller kicks in. In addition, due to the phase lag, the PID controller performs poorly when exposed to varying disturbances. This could be compensated by increased damping, but as there will always be residues of wave frequencies in the LF velocity estimates, this would lead to increased wear and tear on the actuators [25].

Introducing acceleration feedback (AFB) is an alternative way to handle these problems. AFB can be viewed as virtually manipulating the mass of the vessel. Negative feedback increases the mass, while positive feedback decreases it. By applying negative acceleration feedback, the system appears virtually heavier from the disturbance's point of view, and thus the effects of the disturbance are attenuated. This will improve the closed-loop dynamics and thus improve the stationkeeping performance [25]. AFB can also be used to virtually shape the kinetic energy of the vessel, later to be used in e.g. backstepping designs [29]. Acceleration measurements are usually gathered from inertial measurement units (IMUs), which are small, high-precision units that measure linear accelerations, and often angular rates as well. IMUs are becoming increasingly cheap in cost, and are easily retrofitted in existing control and navigation systems for increased performance. In addition, the sensor equipment was initially intended for aircraft and is therefore very reliable and robust [25]. The use of acceleration measurements are common in the aerospace industry [33], but are generally considered superfluous in marine control as the model-based systems tend to perform excellent. However, when system parameters are not well known, positioning performance may become poor. As implied in Newton's 2. law, the acceleration is proportional with the resulting force acting on the vessel, and thus by decomposing the absolute acceleration $\boldsymbol{a}$ into $\boldsymbol{a} = \boldsymbol{a}_a + \boldsymbol{a}_e$, where $\boldsymbol{a}_a$ represents the acceleration due to known forces and $\boldsymbol{a}_e$ represents accelerations due to unknown environmental disturbances, $\boldsymbol{a}_e$ can be directly compensated by applying AFB [26]. Notice that $\boldsymbol{a}_e$ also encapsulates model uncertainties, and thus by applying AFB, direct compensation will also relax the need of an accurate model [26].

3.2 Background

To explore the actual effect of AFB, a scalar and a multiple-input multiple-output (MIMO) example is presented.

3.2.1 Scalar Example

Considering a 1 DOF simplified ship model, the low speed model takes the form of a linear mass-damper

$$m\ddot{x} + d\dot{x} = \tau + w \tag{3.1}$$

where m is the mass, d is the linear damping constant, x, $\dot{x} = v$ and $\ddot{x}$ represent position, velocity and acceleration, respectively, τ is the control input and w is the unknown disturbance. By defining the time constant $T = m/d > 0$, the transfer function from the velocity to the disturbance can be written as

$$\frac{v}{w}(s) = \frac{v}{\tau}(s) = \frac{1}{d}\frac{1}{1+Ts} \tag{3.2}$$

Introducing a control law including acceleration feedback as

$$\tau = -K_m\dot{v} + \tau_{PID} \tag{3.3}$$

where τ_{PID} represents a conventional PID controller to be described later, and $K_m > 0$ is the acceleration feedback gain. The negative K_m term will virtually increase the vessel mass to $m_{total} = m + K_m$, such that (3.1) including the control law (3.3) can now be written as

$$(m + K_m)\ddot{x} + d\dot{x} = \tau_{PID} + w \tag{3.4}$$

or equivalently

$$\ddot{x} + \frac{d}{(m + K_m)}\dot{x} = \frac{1}{(m + K_m)}\tau_{PID} + \frac{1}{(m + K_m)}w \tag{3.5}$$

It can now be noticed that the disturbance gain has been reduced from $1/m$ to $1/(m + K_m)$ and the system will thus as expected be less sensitive to external disturbances. This is also apparent in the velocity to disturbance transfer function (3.2), which now can be expressed as

$$\frac{v}{w}(s) = \frac{v}{\tau_{PID}}(s) = \frac{1}{d}\frac{1}{1 + \frac{m+K_m}{d}s} \tag{3.6}$$

where the Bode plot of the transfer function before and after AFB is shown in Figure 3.2.2.

For improvement, the acceleration term can be expanded to a dynamic system $h_m(s)$, such that the virtual mass of the vessel becomes $m_{total}(s) = m + h_m(s)$. The control law then takes the form

$$\tau = -h_m(s)\dot{v} + \tau_{PID} \tag{3.7}$$

$h_m(s)$ can conveniently be chosen as a low-pass filter to attenuate low-frequency disturbances [1], as

$$h_m(s) = \frac{K_m}{T_m s + 1} \tag{3.8}$$

where $K_m > 0$ is the gain and $T_m > 0$ is the time constant. (3.4) can now be written as

$$\underbrace{(m + \frac{K_m}{T_m s + 1})}_{m_{total}(s)}\ddot{x} + d\dot{x} = \tau_{PID} + w \tag{3.9}$$

This means that for low frequencies, i.e. below $\omega_m = 1/T_m$, the total mass increases to $m + K_m$, while for high frequencies, the mass will converge to m as $h_m(s) \to 0$ for $\omega \gg \omega_m$, as seen in Figure 3.2.1.

The transfer function from velocity to disturbance can now be written as

$$\frac{v}{w}(s) = \frac{v}{\tau_{PID}}(s) = \frac{1}{d}\frac{1 + T_m s}{mT_m s^2 + (T_m + T + \frac{K_m}{d})s + 1} \tag{3.10}$$

and as seen in Figure 3.2.2, the frequency response is much better than the constant AFB except for a small range near the cutoff frequency. However, this exact

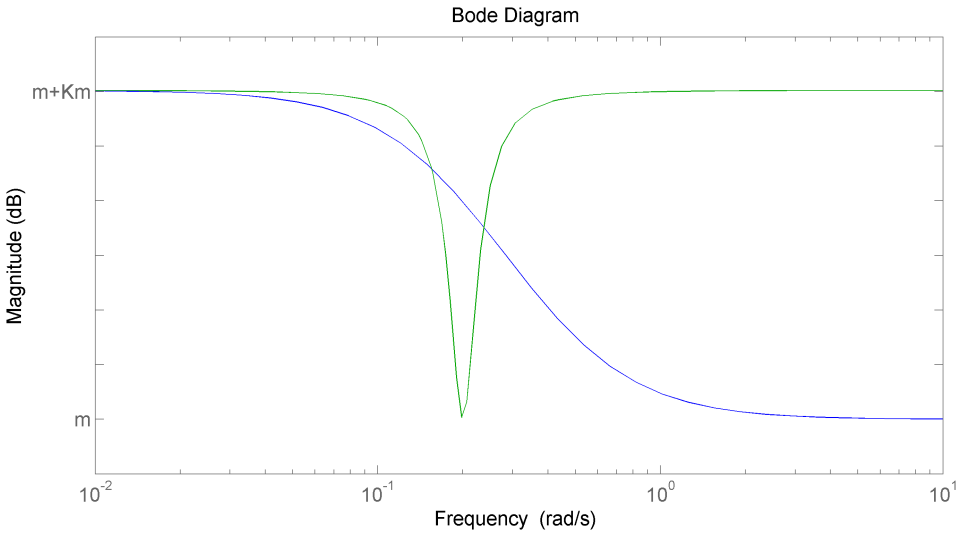

Figure 3.2.1: Virtual mass $h_m(s)$, where blue represents LP and green represents notch.

response is just a result of the chosen parameters used in the transfer function, which in this case are as follows: $m = 10$, $K_m = 10$, $d = 3$, $T_m = 5$, $\zeta = 0.2$ and $\omega_n = 0.2$, such that a different tuning of the filters or a different model would yield a different response.

The AFB filter $h_m(s)$ can also be chosen as a notch filter to attenuate first-order wave-induced forces [1]. Considering a second order notch filter on the form

$$h_m(s) = \frac{K_m(s^2 + \omega_n^2)}{s^2 + 2\zeta\omega_n s + \omega_n^2} \tag{3.11}$$

gives the transfer function from velocity to disturbance

$$\frac{v}{w}(s) = \frac{s^2 + 2\zeta\omega_n s + \omega_n^2}{(m + K_m)s^3 + (2\zeta\omega_n m + d)s^2 + (2\zeta\omega_n d + \omega_n^2(m + K_m))s + d\omega_n^2} \tag{3.12}$$

where the Bode plot is shown in Figure 3.2.2. The frequency response is similar to the constant AFB, except for a peak around ω_n, where the virtual mass approaches m (as seen in Figure 3.2.1). The effect of this peak will be that the first-order wave-induced forces will not be fed back to the controller and will thus reduce wear and tear on the actuators. However, the wave frequency is uncertain, so in the case of poor accuracy of the chosen notch frequency ω_n, the performance may become poor and the actuator wear will not be reduced for disturbances that does not fall within the notch frequency. This can be solved by introducing an adaptive notch filter, were the notch frequency ω_n is adapted to match the frequency of the incoming wave train. This matter is further discussed in Section 6.2.

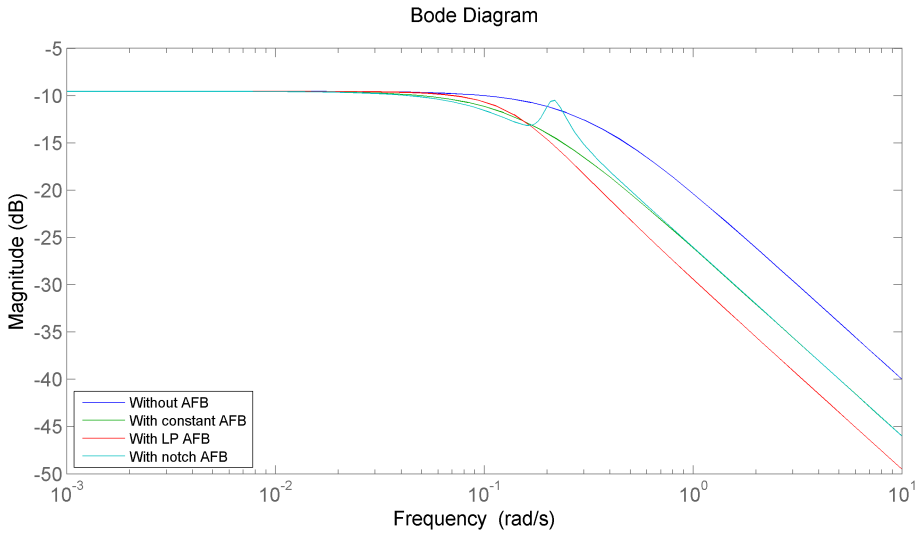

Figure 3.2.2: Bode plot of $\frac{v}{w}(s)$ without and with constant and dynamic AFB.

3.2.2 MIMO Example

Considering the 3 DOF model in (2.9) with the corresponding mass matrix given in (2.4) as

$$\boldsymbol{M} = \boldsymbol{M}_{RB} + \boldsymbol{M}_A = \begin{bmatrix} m - X_{\dot{u}} & 0 & 0 \\ 0 & m - Y_{\dot{v}} & mx_g - Y_{\dot{r}} \\ 0 & mx_g - N_{\dot{v}} & I_z - N_{\dot{r}} \end{bmatrix} \tag{3.13}$$

it can be noticed that $\boldsymbol{M}$ is not symmetrical, i.e. $\boldsymbol{M} \neq \boldsymbol{M}^T$, as $\boldsymbol{M}_{23} \neq \boldsymbol{M}_{32}$. This is because while the rigid-body mass matrix is symmetrical, the added mass matrix $\boldsymbol{M}_A$ is non-symmetrical due to wave-induced forces and forward speed effects [29]. For zero speed or low speed ($U \approx 0$) it is often assumed that $\boldsymbol{M} = \boldsymbol{M}^T$, but that is under several simplifying assumptions such as neglecting currents and incident waves. The non-symmetrical property will cause a problem for energy-based Lyapunov control techniques as they require that the system inertia matrix is positive definite, i.e. $\boldsymbol{M} = \boldsymbol{M}^T > 0$. This can be solved by including acceleration feedback, as the system inertia matrix can be reshaped to become symmetrical [29]. Notice that as the IMU only provide measurements of linear accelerations, there are no available measurements of accelerations in yaw. Recalling the control law including AFB and PID in (3.3) as

$$\boldsymbol{\tau} = -\boldsymbol{K}_m \dot{\boldsymbol{\nu}} + \boldsymbol{\tau}_{PID} \tag{3.14}$$

will then yield a gain $\boldsymbol{K}_m > 0$ on the form

$$\boldsymbol{K}_m = \begin{bmatrix} K_{11} & K_{12} & 0 \\ K_{21} & K_{22} & 0 \\ K_{31} & K_{32} & 0 \end{bmatrix} \tag{3.15}$$

Including AFB will then change the system inertia matrix to

$$\begin{aligned} \boldsymbol{H} &= \boldsymbol{M} + \boldsymbol{K}_m \\ &= \begin{bmatrix} m - X_{\dot{u}} + K_{11} & K_{12} & 0 \\ K_{21} & m - Y_{\dot{v}} + K_{22} & mx_g - Y_{\dot{r}} \\ K_{31} & mx_g - N_{\dot{v}} + K_{32} & I_z - N_{\dot{r}} \end{bmatrix} \end{aligned} \tag{3.16}$$

By letting

$$\boldsymbol{K}_m = \begin{bmatrix} X_{\dot{u}} + \Delta K_{11} & 0 & 0 \\ 0 & Y_{\dot{v}} + \Delta K_{22} & 0 \\ 0 & N_{\dot{v}} - Y_{\dot{r}} & 0 \end{bmatrix} \tag{3.17}$$

the reshaped inertia matrix becomes

$$\boldsymbol{H} = \begin{bmatrix} m + \Delta K_{11} & 0 & 0 \\ 0 & m + \Delta K_{22} & mx_g - Y_{\dot{r}} \\ 0 & mx_g - Y_{\dot{r}} & I_z - N_{\dot{r}} \end{bmatrix} \tag{3.18}$$

which implies that $\boldsymbol{H} = \boldsymbol{H}^T > 0$. The remaining design parameters, ΔK_{11} and ΔK_{22}, can be viewed as additional mass manipulators in the surge and sway directions, respectively. In addition, by choosing $\Delta K_{11} = \Delta K_{22}$, the mass will be equal in surge and sway, such that the PID controller will be independent on the heading angle, which gives an advantage in tuning of the DP controller [29].

Chapter 4

Controller Design

In order to dynamically position a marine vessel, some form of motion control system is needed. The problems of motion control of marine craft can be roughly classified into three groups [34]:

- *point stabilization (or setpoint regulation)*, to stabilize the vessel at a given fixed position with a desired heading.
- *trajectory tracking*, to have the vessel track a time parameterized reference.
- *path following*, to have the vessel converge to and follow a desired path, which is independent of time.

Trajectory tracking is the most common configuration for fully or over-actuated vehicles, i.e. the number of actuators are equal to or greater than the number of states that are to be tracked. This is thus a fitting approach for DP vessels, as they typically have more than three actuators to control horizontal motion. Trajectory tracking can also be used to track targets, e.g. seismic tracking or tracking of other ships, where the reference points are given by a separate tracking algorithm. The most common applications for DP vessels are low-speed maneuvering and stationkeeping, where it can be noticed that stationkeeping is tracking control with a constant position reference, which is equivalent to point stabilization.

Path following is a more common approach for under-actuated vessels [25], i.e. there are less actuators than the number of states to be tracked, where the typical configuration is forward speed and turning control. Path following can also be used on fully or over-actuated vehicles that operate in heading autopilot mode, such that the forward speed is held constant, while the heading is controlled to track the path. A popular method for this kind of path following is line-of-sight (LOS) guidance [1].

4.1 PID

Assuming full state feedback, a DP controller inspired by traditional PID controllers is proposed. Even though the controller is nonlinear, the linear terms can be isolated and tuned using linear pole placement techniques, while the nonlinearities are added and tuned later on. As the use of traditional multivariable PID controllers is the most common approach in DP systems today [11], the linear design techniques gives the advantage of intuitive tuning, compared to certain nonlinear control approaches that require a more theoretical background. The PID controller is augmented with nonlinear stiffness and damping terms in order to make it more responsive with regards to sudden and unknown external disturbances. A non-rigorous stability analysis is also included to show that the DP system is globally asymptotically stable.

4.1.1 Nonlinear Horizontal-Plane PID Control Law

Considering the 3 DOF DP model given in (2.9) as

$$\dot{\boldsymbol{\eta}} = \boldsymbol{R}(\psi)\boldsymbol{\nu} \tag{4.1}$$

$$\boldsymbol{M}\dot{\boldsymbol{\nu}} + \boldsymbol{D}\boldsymbol{\nu} = \boldsymbol{\tau} + \boldsymbol{w} \tag{4.2}$$

where the bias term $\boldsymbol{R}^T(\psi)\boldsymbol{b}$ has been switched out with a general disturbance term $\boldsymbol{w}$, and the relative velocity term $\boldsymbol{\nu}_r$ has been replaced with $\boldsymbol{\nu}$ for simplification, i.e. neglecting current. The objective of the controller is to track a smooth trajectory given by a reference model, which outputs $\boldsymbol{\eta}_d$ and $\boldsymbol{\nu}_d$, the desired positions and heading angle and velocities and yaw rate, respectively. The desired position and heading are commonly given in NED-coordinates, while the desired velocity and yaw rates are given in BODY-coordinates. The deviation vectors $\boldsymbol{e} \in \mathbb{R}^3$, $\tilde{\boldsymbol{\nu}} \in \mathbb{R}^3$ and $\boldsymbol{z} \in \mathbb{R}^3$describing the difference between the estimated and the desired states for position and heading, velocity and yaw rate and integrator states, respectively, can be expressed as [28]

$$\boldsymbol{e} = \begin{bmatrix} e_1 & e_2 & e_3 \end{bmatrix}^T = \boldsymbol{R}^T(\psi_d)(\hat{\boldsymbol{\eta}} - \boldsymbol{\eta}_d) \tag{4.3}$$

$$\tilde{\boldsymbol{\nu}} = \hat{\boldsymbol{\nu}} - \boldsymbol{R}^T(\psi)\dot{\boldsymbol{\eta}}_d \tag{4.4}$$

$$\dot{\boldsymbol{z}} = \boldsymbol{e} \tag{4.5}$$

where ψ_d is the desired heading angle, and $\hat{\boldsymbol{\eta}}$ and $\hat{\boldsymbol{\nu}}$ represent the estimates for position/heading and velocity/yaw rate, respectively. Notice that $\tilde{\boldsymbol{\nu}}$ is given in the BODY-frame, while $\boldsymbol{e}$ and $\dot{\boldsymbol{z}}$ are given in the reference-parallel frame.

Introducing the control law $\boldsymbol{\tau} = \boldsymbol{\tau}_{PID}$ as described in [28]

$$\boldsymbol{\tau}_{PID} = -\boldsymbol{R}_e^T\boldsymbol{K}_p\boldsymbol{e} - \boldsymbol{R}_e^T\boldsymbol{K}_{p3}\boldsymbol{f}(\boldsymbol{e}) - \boldsymbol{K}_d\tilde{\boldsymbol{\nu}} - \boldsymbol{R}_e^T\boldsymbol{K}_i\boldsymbol{z} \tag{4.6}$$

where $\boldsymbol{K}_p$, $\boldsymbol{K}_d$ and $\boldsymbol{K}_i \in \mathbb{R}^{3\times3}$ are the non-negative proportional, derivative and integral gain matrices of a traditional PID controller, respectively. $\boldsymbol{R}_e \in \mathbb{R}^{3\times3}$ is defined as

$$\boldsymbol{R}_e = \boldsymbol{R}(\psi - \psi_d) := \boldsymbol{R}^T(\psi_d)\boldsymbol{R}(\psi) \tag{4.7}$$

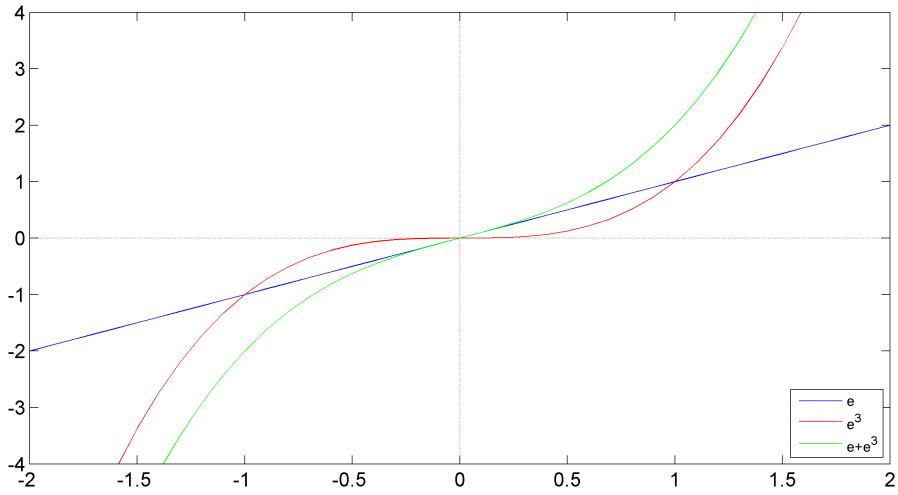

Figure 4.1.1: First-order proportional deviation term vs nonlinear third-order stiffness deviation term.

and can be regarded as a rotation matrix from the BODY-frame to the reference-parallel frame. This means that the control forces are calculated in BODY-coordinates, while the gains are given in the reference-parallel frame. It can later be more convenient to place the gains in front of $\boldsymbol{R}_e^T$, such that the gains become body-fixed, which is more intuitive for tuning purposes [25].

The term $\boldsymbol{f}(\boldsymbol{e})$ is a third order stiffness term proposed in [28] as

$$\boldsymbol{f}(\boldsymbol{e}) = \begin{bmatrix} e_1^3 & e_2^3 & e_3^3 \end{bmatrix}^T \tag{4.8}$$

where $\boldsymbol{K}_{p3} \in \mathbb{R}^{3\times3}$ is the corresponding non-negative gain matrix. This nonlinear term is very aggressive as it will penalize large deviations, i.e. $e_{1,2,3} > 1$, much more than the regular proportional term. However, for smaller deviations, i.e. $e_{1,2,3} < 1$, the proportional term will dominate the stiffness term. This is better visualized in Figure 4.1.1. The stiffness term thus gives the advantage that the proportional gain matrix can be reduced, which will reduce the amount of thrust commanded for small deviations. It will also make the system more responsive against large and sudden unknown external forces such as ice, which reduces the maximal value and duration of the offset after such a disturbance interacts with the vessel.

4.1.2 Stability Analysis

It can be of interest to show that the added stiffness term does not affect the stability properties of a traditional PID controller. The stability analysis is done by applying energy-based stability proofs as found in [1] and [35].

For simplification of the stability proof, the following assumptions are made: estimates are replaced with perfect signals for notational simplification; the desired

velocity equals zero, i.e. $\dot{\boldsymbol{\eta}}_d = 0$, such that the regulation of $\boldsymbol{\eta}$ to $\boldsymbol{\eta}_d$ is constant; the desired and actual heading angle equals zero, i.e. $\psi = \psi_d = 0$, as this greatly simplifies the derivation; the integral action can be removed, i.e. $\boldsymbol{K}_i = 0$, as more elaborately explained in Section 4.2.1. In addition, for the purpose of general analysis, the system is reduced to 1 DOF, such that e.g. $\boldsymbol{\nu}^T \boldsymbol{M} \boldsymbol{\nu}$ can be written as $M\nu^2$. Notice that the use of subscripts to represent a single DOF in each vector or matrix has been neglected for notational simplification. It should be mentioned that this approach is not rigorous, but it greatly simplifies the analysis and will still give a good idea of the stability properties.

The control law in (4.6) can now be expressed as

$$\tau_{PD} = -K_p e - K_{p3} f(e) - K_d \nu \tag{4.9}$$

and by noticing that (4.1) can be rewritten as

$$\nu = \dot{\eta} \tag{4.10}$$

and

$$\dot{e} = \dot{\eta} - \dot{\eta}_d = \dot{\eta} = \nu \tag{4.11}$$

which will be exploited later in the analysis.

Now let the control law (4.9) be written as

$$\tau_{PD} = -K_p(t) e - K_d \nu \tag{4.12}$$

where a new gain term for the position deviation has been defined as

$$K_p(t) := K_p + K_{p3} e^2 \tag{4.13}$$

where $K_p(t) > 0, \ \forall t$ as $K_p, K_{p3} > 0$. The $K_p(t)$ gain encapsulates the third-order stiffness term in a single term, such that the controller takes the form of a traditional PD controller. Notice that $K_p(t)$ is time-varying as it is a function of the position deviation e, and will thus have a non-zero derivative.

4.1.2.1 Lyapunov Stability

As described in Appendix A, a Lyapunov function can be used to analyze the stability properties of the system.

Proposing a Lyapunov function candidate as

$$\begin{aligned} V &= \frac{1}{2} M \nu^2 + \frac{1}{2}(K_p + \frac{1}{2} K_{p3} e^2) e^2 \\ &= \frac{1}{2} M \nu^2 + \frac{1}{2} K_{p2}(t) e^2 \end{aligned} \tag{4.14}$$

where

$$K_{p2}(t) := K_p + \frac{1}{2} K_{p3} e^2 \tag{4.15}$$

where $M > 0$ and $K_{p2}(t) > 0$, $\forall t$. Notice that the two terms in (4.14) can be regarded as kinetic and potential energy, respectively [1]. Also notice that the more intuitive Lyapunov function candidate $V = \frac{1}{2}M\nu^2 + \frac{1}{2}K_p(t)e^2$ will not work due to the e^2 term inside $K_p(t)$.

(4.14) is then time differentiated along the trajectories of ν and e, such that

$$\dot{V} = M\dot{\nu}\nu + \frac{1}{2}\dot{K}_{p2}(t)e^2 + K_{p2}(t)e\dot{e} \tag{4.16}$$

where

$$\dot{K}_{p2}(t) = K_{p3}e\dot{e} \tag{4.17}$$

Inserting (4.17) into (4.16) yields

$$\begin{aligned}\dot{V} &= M\dot{\nu}\nu + K_{p2}(t)e\dot{e} + \frac{1}{2}K_{p3}e^3\dot{e} \\ &= M\dot{\nu}\nu + (K_{p2}(t) + \frac{1}{2}K_{p3}e^2)e\dot{e}\end{aligned} \tag{4.18}$$

and by replacing $K_{p2}(t)$ with (4.15)

$$\begin{aligned}\dot{V} &= M\dot{\nu}\nu + (K_p + \frac{1}{2}K_{p3}e^2 + \frac{1}{2}K_{p3}e^2)e\dot{e} \\ &= M\dot{\nu}\nu + K_p(t)e\dot{e} \\ &= (M\dot{\nu} + K_p(t)e)\nu\end{aligned} \tag{4.19}$$

where (4.11) was used to switch out $\dot{e} = \nu$. Inserting the DP model from (4.2) and the control law (4.12) into (4.19) then gives

$$\begin{aligned}\dot{V} &= (-K_p(t)e - K_d\nu + w - D\nu + K_p(t)e)\nu \\ &= w\nu - (K_d + D)\nu^2\end{aligned} \tag{4.20}$$

If the disturbance is neglected, (4.20) becomes

$$\dot{V} = -(K_d + D)\nu^2 \leq 0, \ \forall \nu \tag{4.21}$$

which according to [1] proves that the system is globally asymptotically stable (GAS) by applying Krasovskii-LaSalle's Theorem (A.1). In addition, the trajectories of ν and e will converge to the set Ω, which is the set of all points where $\dot{V} = 0$, i.e.

$$\dot{V} = -(K_d + D)\nu^2 \equiv 0 \tag{4.22}$$

This is true for $\nu = 0$, and thus the set Ω becomes

$$\Omega = \{(e, \nu) : \nu = 0\} \tag{4.23}$$

At the equilibrium point $\nu = 0$, the system becomes

$$M\dot{\nu} = -K_p(t)e \tag{4.24}$$

which yields that the system cannot get stuck at an equilibrium point other than $e = 0$, because as long as $e \neq 0$, the system (4.24) is non-zero. As the equilibrium point is the origin, i.e. $(e, \nu) = (0, 0)$, it is the largest invariant set in Ω, and thus according to Theorem (A.1), the origin is GAS.

Considering the special case where the disturbance is non-zero, but constant, i.e. $\dot{w} = 0$, the system will be uniformly ultimately bounded (UUB), which means that the trajectories of ν and e will converge to a ball about the equilibrium point $(e, \nu) = (0, 0)$. The radius of the ball will depend on the magnitude of w [1]. It is also possible to prove local asymptotic stability (LAS) in the case where integral action is included to remove the constant disturbance [1].

4.1.3 Cubic Damping

To compensate for the added nonlinear stiffness term, it can be advantageous to introduce a nonlinear damping term as well. The nonlinear damping gives the advantage of reduced transmissibility of force around the resonant frequency range, while leaving the higher frequencies unaffected [36]. In other words, it will reduce the oscillating effects that may arise when the stiffness term dominates the proportional term, which can be the case for large deviations as seen in Figure 4.1.2. For small deviations, the effect of the cubic damping becomes negligible, as also seen in Figure 4.1.2.

The nonlinear damping term $\boldsymbol{d}(\tilde{\boldsymbol{\nu}})$ can be described by the general form [1]

$$\boldsymbol{d}(\tilde{\boldsymbol{\nu}}) = \begin{bmatrix} d_1(\tilde{\nu}_1) & \dots & d_n(\tilde{\nu}_n) \end{bmatrix}^T \tag{4.25}$$

where

$$d_i(\tilde{\nu}_i) = |\tilde{\nu}_i|^{p_i}\tilde{\nu}_i \quad (i = 1, \dots, n) \tag{4.26}$$

where $p_i > 0$ are integers. As the stiffness term in this case is cubic, it is appropriate to choose cubic damping as well. By letting $p_{1,2,3} = 2$, (4.26) becomes

$$d_i(\tilde{\nu}_i) = |\tilde{\nu}_i|^2\tilde{\nu}_i = \tilde{\nu}_i^3 \quad (i = 1, 2, 3) \tag{4.27}$$

such that

$$\boldsymbol{d}(\tilde{\boldsymbol{\nu}}) = \begin{bmatrix} \tilde{\nu}_1^3 & \tilde{\nu}_2^3 & \tilde{\nu}_3^3 \end{bmatrix}^T \tag{4.28}$$

4.1.3.1 Stability with Cubic Damping

To check the stability properties when nonlinear cubic damping is included, the same assumptions as in Section 4.1.2 must be applied. As $\dot{\boldsymbol{\eta}}_d = 0$, (4.4) becomes

$$\tilde{\boldsymbol{\nu}} = \boldsymbol{\nu} - \boldsymbol{R}^T(\psi)\dot{\boldsymbol{\eta}}_d = \boldsymbol{\nu} \tag{4.29}$$

such that (4.28) reduces to

$$\boldsymbol{d}(\tilde{\boldsymbol{\nu}}) = \boldsymbol{d}(\boldsymbol{\nu}) = \begin{bmatrix} \nu_1^3 & \nu_2^3 & \nu_3^3 \end{bmatrix}^T \tag{4.30}$$

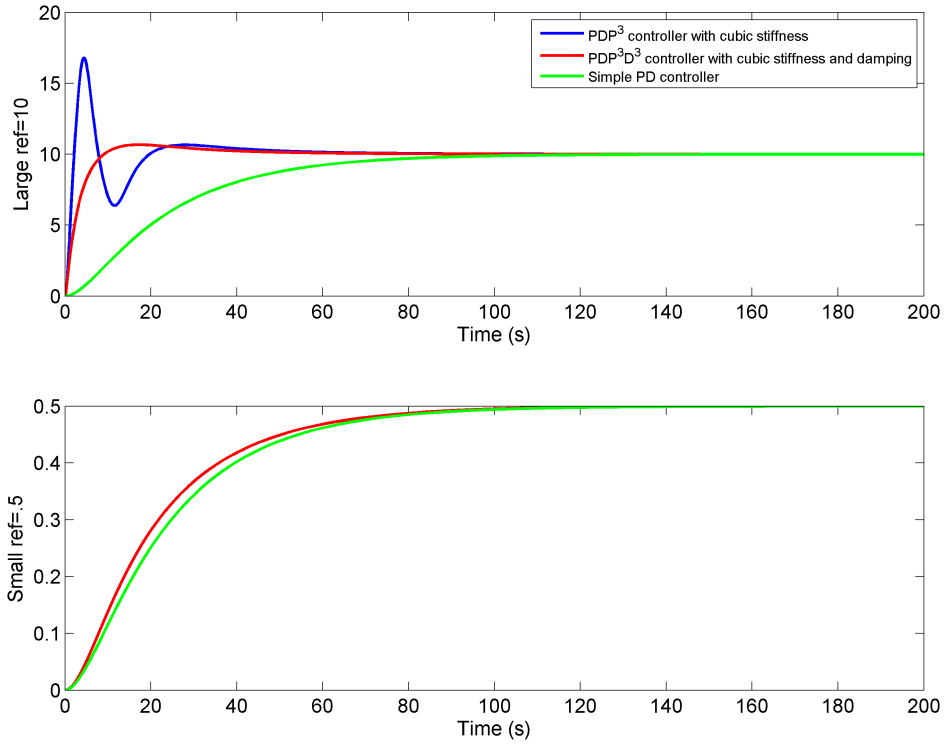

Figure 4.1.2: Comparison of controller performance between PD with stiffness, with and without cubic damping. The top plot represents a large deviation, while the bottom plot represents a small deviation.

Again, considering one DOF, the control law in (4.9) can be expressed as

$$\tau_{PD} = -K_p e - K_{p3} f(e) - K_d \nu - K_{d3} d(\nu) \tag{4.31}$$

where $K_{d3} \in \mathbb{R}^{3\times 3}$ is a non-negative gain. By defining the term

$$K_d(t) := K_d + K_{d3}\nu^2 \tag{4.32}$$

where $K_d(t) > 0,\ \forall t$ as $K_d, K_{d3} > 0$, (4.31) reduces to

$$\tau_{PD} = -K_p(t)e - K_d(t)\nu \tag{4.33}$$

and thus again takes the form of a traditional PD controller. By applying the same Lyapunov function candidate (4.14) as in Section 4.1.2.1, the derivatives along the trajectories become

$$\begin{aligned} \dot{V} &= (M\dot{\nu} + K_p(t)e)\nu \\ &= (\tau_{PD} + w - D\nu + K_p(t)e)\nu \end{aligned} \tag{4.34}$$

Again assuming that $w = 0$, and inserting the new control law (4.33) into (4.34) gives

$$\dot{V} = (-K_p(t)e - K_d(t)\nu - D\nu + K_p(t)e)\nu \tag{4.35}$$
$$= -(K_d(t) + D)\nu^2 \leq 0, \ \forall \nu \tag{4.36}$$

which proves that the origin of the system is GAS by applying Krasovskii-LaSalle's Theorem (A.1).

4.1.4 Controller Tuning

Again considering 1 DOF at a time, the DP model can be described by the scalar system

$$m\ddot{x} + d\dot{x} = \tau + w \tag{4.37}$$

where the control law is

$$\tau = -K_p\tilde{x} - K_d\dot{x} \tag{4.38}$$

where $\tilde{x} = x - x_d$, and the regulation from x to x_d is assumed to be constant, i.e. $\dot{x}_d = 0$. If the disturbance is neglected, then (4.37) becomes

$$m\ddot{x} + (d + K_d)\dot{x} + K_p\tilde{x} = 0 \tag{4.39}$$

Comparing (4.39) with the mass-damper-spring reference model

$$\ddot{x} + 2\zeta\omega_n\dot{x} + \omega_n^2 x = \omega_n^2 x_d \tag{4.40}$$

where ζ is the relative damping ratio and ω_n is the natural frequency, gives

$$\omega_n = \sqrt{\frac{K_p}{m}} \tag{4.41}$$

$$\zeta = \frac{d + K_d}{2m\omega_n} = \frac{d + K_d}{2m\sqrt{\frac{K_p}{m}}} = \frac{d + K_d}{2\sqrt{mK_p}} \tag{4.42}$$

Pole placement can then be used to make the DP system behave like the reference model, by specifying ζ and ω_n. Solving (4.41) and (4.42) for K_p and K_d yields

$$K_p = \omega_n^2 m \tag{4.43}$$

$$K_d = 2\zeta\omega_n m - d \tag{4.44}$$

If integral action is applied, a rule of thumb according to [1] is to use an integrator that is 10 times slower than the natural frequency, which yields

$$K_i = \frac{\omega_n}{10}K_p = \frac{\omega_n^3}{10}m \tag{4.45}$$

4.1.4.1 Control Bandwidth

The control bandwidth ω_b is defined as the frequency where the closed loop gain equals -3 dB, which yields the formula [1]

$$\omega_b = \omega_n \sqrt{1 - 2\zeta^2 + \sqrt{4\zeta^4 - 4\zeta^2 + 2}} \tag{4.46}$$

and thus

$$\omega_n = \omega_b \frac{1}{\sqrt{1 - 2\zeta^2 + \sqrt{4\zeta^4 - 4\zeta^2 + 2}}} \tag{4.47}$$

For a critically damped system, i.e. $\zeta = 1$, (4.46) reduces to

$$\omega_n = \omega_b \frac{1}{\sqrt{\sqrt{2} - 1}} \tag{4.48}$$

This means that the only parameters needed to tune the controller are ω_b and ζ.

4.1.4.2 Tuning with Nonlinear Stiffness and Damping

When it comes to tuning the gains in front of the nonlinear stiffness and damping terms, the previous mass-damper-spring reference model cannot be applied directly as it is a linear system. In addition, traditional pole placement cannot be used as it only applies to linear systems. However, there does exist pole placement techniques for nonlinear systems, e.g. by the use of neural networks to model the nonlinear systems [37].

An easier method is to use the same tuning technique as above, but with the added stiffness and nonlinear damping in the reference model, such that

$$\ddot{x} + 2\zeta\omega_n\dot{x} + K_{d3}\dot{x}^3 + \omega_n^2\tilde{x} + K_{p3}\tilde{x}^3 = 0 \tag{4.49}$$

By exploring the step responses of different setpoints x_d, appropriate values for K_{p3} and K_{d3} can be found. It is then proposed to choose the gains as

$$K_{p3} = \gamma_p K_p \tag{4.50}$$
$$K_{d3} = \gamma_d K_d \tag{4.51}$$

where $\gamma_p \geq 0$ and $\gamma_d \geq$ are design parameters.

Notice that the added nonlinear terms invalidate the chosen relative damping ratio and controller bandwidth, but as the linear terms will dominate the nonlinear terms for small deviations, it is still a useful property for stationkeeping purposes.

4.2 Acceleration Feedback

The PID controller can now be augmented with acceleration feedback, to take advantage of the properties discussed in Chapter 3.

4.2.1 Disturbance Rejection by Acceleration Feedforward

Introducing Disturbance Rejection by Acceleration Feedforward (hereby denoted as AFF), the control law now takes the form

$$\boldsymbol{\tau} = \boldsymbol{\tau}_{PID}(t) - \boldsymbol{\tau}_{FF}(t) \tag{4.1}$$

where $\boldsymbol{\tau}_{PID}$ is adopted from (4.6). The term $\boldsymbol{\tau}_{FF}$ can be viewed as an acceleration feedforward term, and it is provided by [26] as

$$\boldsymbol{\tau}_{FF}(t) = \boldsymbol{M}\dot{\hat{\boldsymbol{\nu}}}(t-\delta) + \boldsymbol{D}\hat{\boldsymbol{\nu}}(t-\delta) - \boldsymbol{\tau}(t-\delta) \tag{4.2}$$

where $\delta > 0$ is the time delay from the when actual acceleration occurs, to when the estimated acceleration is available. $\boldsymbol{\tau}_{FF}$ thus acts like an estimate of the unknown external disturbances, which is made clear by recalling the 3 DOF DP model (4.2)

$$\boldsymbol{M}\dot{\boldsymbol{\nu}}(t) + \boldsymbol{D}\boldsymbol{\nu}(t) = \boldsymbol{\tau}(t) + \boldsymbol{w}(t) \tag{4.3}$$

such that

$$\boldsymbol{\tau}_{FF}(t) = \hat{\boldsymbol{w}}(t) = \boldsymbol{w}(t-\delta) \tag{4.4}$$

By defining the disturbance estimation error $\tilde{\boldsymbol{w}}(t)$ as

$$\tilde{\boldsymbol{w}}(t) := \boldsymbol{w}(t) - \hat{\boldsymbol{w}}(t) = \boldsymbol{w}(t) - \boldsymbol{w}(t-\delta) \tag{4.5}$$

it can be noticed that fast measuring and processing leads to a fast estimate with a small delay δ, and as $\delta \to 0$ the estimation error $\tilde{\boldsymbol{w}}(t) \to 0$, which would imply that the acceleration feedforward perfectly cancels out the disturbance. However, this is not possible as $\delta = 0$ would violate causality [26]. It can also be noticed that the estimate will encapsulate model uncertainties, as their contribution to the system will be interpreted as disturbances. This property is further explored with simulations in Chapter 7.

The resulting closed-loop system can then be found by inserting (4.1) and (4.4) into (4.3) such that

$$\boldsymbol{M}\dot{\boldsymbol{\nu}}(t) + \boldsymbol{D}\boldsymbol{\nu}(t) = \boldsymbol{\tau}_{PID}(t) + \tilde{\boldsymbol{w}}(t) \tag{4.6}$$

If the disturbance rejection was to be perfect, it would remove the need for integral action in the PID controller. However, some integral effect is recommended to take care of the residues of the feedforward cancellation [26].

4.2.1.1 Stability with Disturbance Rejection

Under the same assumptions as in Section 4.1.2, and if $\tilde{\boldsymbol{w}}(t) = 0$, the system will be identical to the one analyzed in Section 4.1.2.1, and thus the origin is GAS. In the case where the feedforward term is just a fixed-gain AFB, such that $\boldsymbol{\tau}_{FF} = -\boldsymbol{K}_m\dot{\boldsymbol{\nu}}$ as explored in Section 3.2.2, the system inertia matrix is the only thing that changes, i.e. $\boldsymbol{H} = \boldsymbol{M} + \boldsymbol{K}_m$. As $\boldsymbol{H} = \boldsymbol{H}^T > 0$, the origin is still GAS. In the case where the AFB is dynamic such that $h_m(s)$ is e.g. a low-pass filter, the stability analysis becomes much more complex, and will not be explored in this thesis.

Chapter 5

Predictive Feedforward Control

5.1 Motivation

As previously mentioned in Section 1.1, a proactive control strategy is a possible measure against some of the ice-related challenges in arctic DP operations. As proposed in [23], a predictive system with inputs from an ice observation system, e.g. as described in [20], can be used to produce a feedforward compensation control. An advanced ice observation system can be used to measure and estimate the local time-varying ice characteristics, such as [23]

- *ice concentration*
- *floe size distribution*
- *ice floe identification*, i.e. position, area, shape, mass, etc.
- *ice thickness*
- *ice drift velocity, direction, etc.*

A predictive system using numerical simulation tools can then be used to predict near future incoming ice disturbances. An important application of the information provided by the predictive system, is the opportunity to prepare the DP controller for the incoming disturbance. The information can also be used as an input to the navigation system to guide the vessel efficiently through, or if necessary, around the ice to minimize applied thrust.

If the DP controller was aware of the incoming ice some time before impact, it could be designed to prepare the thruster system for the upcoming incident. One measure would be to position the direction of the thrusters, such that they would be able to apply thrust in the direction of the incoming ice immediately after impact. As thrusters require several seconds to rotate or reverse, a poorly positioned

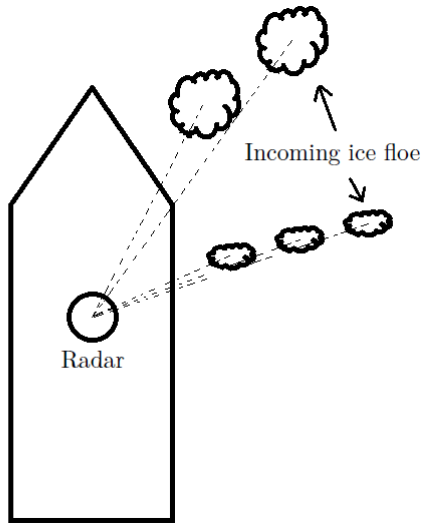

Figure 5.2.1: Illustration of the use of a 360° scanning radar to detect incoming ice floes.

thruster allocation can yield poor stationkeeping performance from an unfortunate point of ice impact. Another measure would be to position the thrusters, and then apply compensating force before impact. Imagine that the ice load would move the vessel e.g. 2 meters off position before the controller corrects the deviation. If some predictive force was applied, the vessel could e.g. move 1 meter toward the ice, to then move only 1 meter off position the other way. This can be of significant difference if the allowable operating circle is e.g. 1 meter.

5.2 Ice Floe Detection

To determine what kind of predictive force that is to be set up, the possibility of compensating thrust must be explored. The predictive thrust will have a general force vector $\boldsymbol{\tau}_p = \begin{bmatrix} X_p & Y_p & N_p \end{bmatrix}^T$ and a duration t_p, where $\boldsymbol{\tau}_p$ represents force in surge and sway, and moment in yaw, respectively, while t_p is the amount of time before impact the thrust is to be applied. To determine these values, the properties of the incoming ice floes must be evaluated. As illustrated in Figure 5.2.1, a 360° scanning radar can be used to detect incoming ice floes. As proposed in [20] the radar can be aided by thermal IR (infrared) sensors and pattern recognition to better monitor the ice moving close to the vessel. If the radar is implemented with a tracking algorithm to tag and distinguish between each incoming ice floe, the basic Algorithm 5.2.1 can be used to estimate the direction, point of impact, velocity and time of impact of an incoming floe.

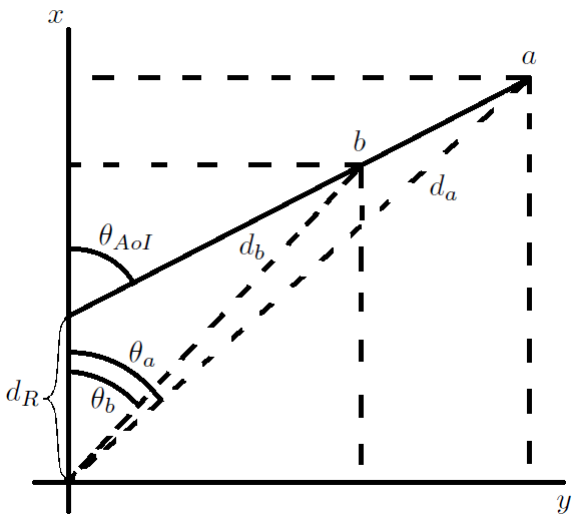

Figure 5.2.2: Ice floe detection.

5.2.1 Ice Floe Detection Algorithm

Figure 5.2.2 illustrates the geometry behind the ice floe detection algorithm. By assuming that the radar is placed in the vessel center of origin (CO), the coordinate system of Figure 5.2.2 will coincide with the BODY frame. Let a be the position of the part of the ice floe that is closest to the vessel at time t_a, and let b be the position at time t_b. Assuming that ice floes are considered one at a time, the radar sensor will output a distance d and a heading θ to the floe, such that d_a, d_b are the distances at time t_a and t_b, and θ_a, θ_b are the angles at time t_a and t_b. With these variables it is possible to calculate the angle of impact, θ_{AoI}, and the distance between the radar and the point of impact interpolated along the trajectory of the ice floe, d_R.

By defining the position vectors $\boldsymbol{p}_a^b = \begin{bmatrix} x_a & y_a \end{bmatrix}^T$ and $\boldsymbol{p}_b^b = \begin{bmatrix} x_b & y_b \end{bmatrix}^T$ where

$$\boldsymbol{p}_a^b = \begin{bmatrix} x_a \\ y_a \end{bmatrix} = \begin{bmatrix} d_a \sin(\theta_a) \\ d_a \cos(\theta_a) \end{bmatrix}, \quad \boldsymbol{p}_b^b = \begin{bmatrix} x_b \\ y_b \end{bmatrix} = \begin{bmatrix} d_b \sin(\theta_b) \\ d_b \cos(\theta_b) \end{bmatrix} \tag{5.1}$$

then basic trigonometry yields

$$\theta_{AoI} = -\text{atan2}(x_a - x_b, y_a - y_b) + \frac{\pi}{2} \tag{5.2}$$

where $\text{atan2}(y, x) \in [-\pi, \pi]$ is the four-quadrant version of $\arctan(y/x) \in [-\frac{\pi}{2}, \frac{\pi}{2}]$, and where the negative sign and the addition of $\frac{\pi}{2}$ is to adapt to yaw, which is defined clockwise from the x-axis.

The distance d_R can then be found as

$$\begin{aligned} d_R &= x_a - y_a \tan\left(-\theta_{AoI} + \frac{\pi}{2}\right) \\ &= x_b - y_b \tan\left(-\theta_{AoI} + \frac{\pi}{2}\right) \end{aligned} \tag{5.3}$$

As the point of interest is the distance between the point of impact and the center of gravity (CG), a mapping of the vessel hull must be included as well as a mapping from the placement of the radar to CG. When considering the simplified vessel shape in Figure 5.2.1, the lateral distance between the radar and the hull $y_{R,beam}$ will be half the ships beam. Incorporating this distance into (5.3) yields

$$d_{beam} = x_a - (y_a - \operatorname{sgn}(\theta_{AoI})\, y_{R,beam}) \tan\left(-\theta_{AoI} + \frac{\pi}{2}\right) \tag{5.4}$$

where d_{beam} is the distance between the radar and the point of impact, parallel shifted to the side hull of the vessel. The $\operatorname{sgn}(\theta_{AoI})$ term is to parallel shift to the side of the incoming floe. The point of impact $\boldsymbol{p}_I^b = \begin{bmatrix} x_I & y_I \end{bmatrix}^T$ then becomes $\boldsymbol{p}_I^b = \begin{bmatrix} d_{beam} & y_{R,beam} \end{bmatrix}^T$. If d_{beam} exceeds the distance between the stern (the rear) or the start of the bow (the sloped side of the front), the distance must be corrected to find the point of impact. In the stern, the distance becomes

$$d_{stern} = y_a + \operatorname{sgn}(\theta_{AoI}) \frac{(x_a + x_{R,stern})}{\tan\left(\theta_{AoI} - \frac{\pi}{2}\right)} \tag{5.5}$$

where $x_{R,stern}$ is the distance from the radar to the stern. The point of impact then becomes $\boldsymbol{p}_I^b = \begin{bmatrix} x_{R,stern} & d_{stern} \end{bmatrix}^T$. The same method can be used to find the point of impact on the sloped side of the bow, where the point will be the intersect between the floe trajectory and the sloped line representing the bow.

The point of impact can now conveniently be used to calculate its distance to CG, to then find the torque produced by the incoming ice floe. The torque $\boldsymbol{T} = \begin{bmatrix} T_x & T_y & T_z \end{bmatrix}^T$ is given as the cross product between the force and the displacement vector between the point of impacting force and the point which the vessel rotates about, i.e. CG [38]. This yields

$$\boldsymbol{T} = \boldsymbol{r}_{I,CG}^b \times \boldsymbol{F}_I \tag{5.6}$$

where $\boldsymbol{r}_{I,CG}^b = \begin{bmatrix} x_I - x_g & y_I & 0 \end{bmatrix}$ is the Cartesian position displacement vector in (x, y, z), where x_g (as described in Section 2.1.3) is the distance from the origin of the BODY-frame to the center of gravity (also recall the assumption $y_g = 0$ in Section 2.4). $\boldsymbol{F}_I = \begin{bmatrix} X_I & Y_I & 0 \end{bmatrix}$ is the force of the incoming ice (assuming no angular motion), which is to be determined later. The moment of the disturbance, N_{dist}, can now be extracted as the T_z term in the torque vector as it represents the torque about the z axis, i.e. the yaw moment, such that

$$N_{dist} = T_z \tag{5.7}$$

In addition, the velocity of the ice floe $\boldsymbol{\nu}_{ice} = \begin{bmatrix} u_{ice} & v_{ice} & r_{ice} \end{bmatrix}^T$ will be given by

$$\boldsymbol{\nu}_{ice} = \begin{bmatrix} \frac{x_b - x_a}{t_b - t_a} \\ \frac{y_b - y_a}{t_b - t_a} \\ 0 \end{bmatrix} \tag{5.8}$$

assuming no angular velocity, and thus the speed becomes

$$U_{ice} = \sqrt{u_{ice}^2 + v_{ice}^2} \tag{5.9}$$

The distance to impact, d_I, can now be calculated as the distance from $\boldsymbol{p}_b^b$, i.e. the position of the ice floe at time t_b, to the point of impact $\boldsymbol{p}_I^b$, as

$$d_I = \sqrt{(x_b - x_I)^2 + (y_b - y_I)^2} \tag{5.10}$$

such that the time to impact t_I can be found as

$$t_I = \frac{d_I}{U_{ice}} \tag{5.11}$$

The estimated velocity can now be fused with information provided by an ice observation system as explained in [20]. A dynamic ice model can be used to estimate the forces acting on the ice floe, i.e. $\boldsymbol{F}_I$, by the use of Newton's law of motion.

5.3 Predictive Box

Using the algorithm in Section 5.2.1, an estimate of the incoming disturbance vector as well as the time of impact is obtained. The remaining issue is to determine what compensating force that should be applied, and how long before impact it should be applied. Two different approaches could e.g. be: apply some force a while before impact, or apply much force right before impact. As the estimates will be far from perfect, it is important to explore what kind of proactive action that will improve the stationkeeping performance, and what kind that will degrade it. Trivially, if proactive thrust is applied in the same direction as the incoming force, the performance could only get worse.

The estimate for the incoming disturbance consists of the four variables F_I, x_I, y_I and θ_{AoI}, where

$$F_I := ||\boldsymbol{F}_I||_{x,y} = \sqrt{X_I^2 + Y_I^2} \tag{5.1}$$

where F_I is defined as the magnitude of the impact force, and where it is assumed that the contribution from angular motion is negligible. The fifth variable will be the time of impact t_I. A simulation of five different variables will yield a problem in five dimensions, and will thus be hard to illustrate. Therefore, by considering

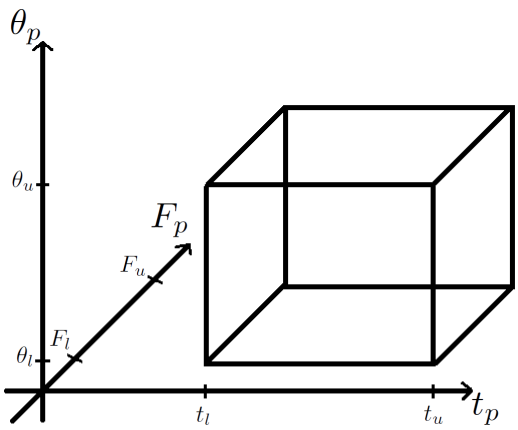

Figure 5.3.1: Predictive box.

one point of impact at a time, the problem is reduced to three dimensions, which is easier to visualize. A predictive box is then proposed as illustrated in Figure 5.3.1, where $\bullet_u$, $\bullet_l$ are the upper and lower test limits, respectively. The predictive thrust force $\boldsymbol{\tau}_p$ can now be expressed as a function of F_p and θ_p, such that

$$\boldsymbol{\tau}_p(F_p, \theta_p) = \begin{bmatrix} X_p \\ Y_p \\ N_p \end{bmatrix} = \begin{bmatrix} F_p \cos(\theta_p) \\ F_p \sin(\theta_p) \\ F_p\left(x_p \sin(\theta_p) - y_p \cos(\theta_p)\right) \end{bmatrix} \tag{5.2}$$

where $\boldsymbol{p}_p^b = \begin{bmatrix} x_p & y_p \end{bmatrix}^T$ is the predicted point of impact with respect to CG. The moment N_p is the torque about the z axis given by (5.6) as

$$N_p = T_z = \begin{bmatrix} 0 & 0 & 1 \end{bmatrix} \left(\begin{bmatrix} x_p & y_p & 0 \end{bmatrix}^T \times \begin{bmatrix} X_p & Y_p & 0 \end{bmatrix}^T \right) \tag{5.3}$$

$$= F_p\left(x_p \sin(\theta_p) - y_p \cos(\theta_p)\right) \tag{5.4}$$

or equivalently by using the formula [38]

$$T_z = \|\boldsymbol{F}_p\| \left\|\boldsymbol{p}_p^b\right\| \sin(\alpha) \tag{5.5}$$

where α is the angle between the force vector $\boldsymbol{F}_p = \begin{bmatrix} X_p & Y_p \end{bmatrix}^T$ and $\boldsymbol{p}_p^b$. The angle between two vectors can be found by the dot product rule [38]

$$\cos(\alpha) = \frac{\boldsymbol{p}_p^b \cdot \boldsymbol{F}_p}{\left\|\boldsymbol{p}_p^b\right\| \|\boldsymbol{F}_p\|} \tag{5.6}$$

By applying the rule [39]

$$\sin(\arccos(x)) = \sqrt{1 - x^2} \tag{5.7}$$

(5.5) becomes

$$T_z = \|\boldsymbol{F}_p\| \left\|\boldsymbol{p}_p^b\right\| \sqrt{1 - \left(\frac{\boldsymbol{p}_p^b \cdot \boldsymbol{F}_p}{\left\|\boldsymbol{p}_p^b\right\| \|\boldsymbol{F}_p\|} \right)^2} \tag{5.8}$$

$$= \sqrt{\left(F_p \left\|\boldsymbol{p}_p^b\right\|\right)^2 - \left(\boldsymbol{p}_p^b \cdot \boldsymbol{F}_p\right)^2} \tag{5.9}$$

where $\|\boldsymbol{F}_p\| = F_p$.

5.4 Simulations

The predictive box in Figure 5.3.1 can now be simulated along each axis to test the effect of applied predictive force. To keep the problem in three dimensions, the point of impact relative to CG, i.e. $\boldsymbol{p}_p^b$, was kept constant for each box, such that $\boldsymbol{\tau}_p$ is only a function of the magnitude F_p and the angle θ_p. The actual disturbance will be simulated as a step, representing a sudden incoming disturbance caused by an incoming ice floe or ice berg. A constant disturbance was chosen over an ice-inspired varying force, as the behavior of the vessel after impact is not a relevant part of the simulation, since the predictive force will only influence the effect of the impact. The constant disturbance can then be specified using the same technique as the calculated proactive force, such that it is a function of the magnitude F_I, with incoming angle θ_{AoI}, impact point $\boldsymbol{p}_{I,CG}^b$ and at the time t_I. The ice force vector then becomes

$$\boldsymbol{\tau}_{ice}(F_I, \theta_{AoI}, \boldsymbol{p}_{I,CG}^b) = - \begin{bmatrix} F_I \cos(\theta_{AoI}) \\ F_I \sin(\theta_{AoI}) \\ F_I \left(x_{I,CG} \sin(\theta_{AoI}) - y_{I,CG} \cos(\theta_{AoI})\right) \end{bmatrix} \tag{5.1}$$

where $\boldsymbol{p}_{I,CG}^b = \begin{bmatrix} x_I - x_g & y_I \end{bmatrix}^T$ is the point of impact with respect to CG and where the negative sign is to direct the disturbance toward the vessel. This yields the disturbance vector

$$\boldsymbol{\tau}_{disturbance}(t) = \begin{cases} \boldsymbol{\tau}_{ice}(F_I, \theta_{AoI}, \boldsymbol{p}_{I,CG}^b) & \text{if } t \geq t_I \\ 0 & else \end{cases} \tag{5.2}$$

The limits of the predictive box can now be chosen as functions of the applied disturbance, such that

$$F_l = \gamma_1 F_I, \quad F_u = \gamma_2 F_I \tag{5.3}$$

$$\theta_{u,l} = \theta_{AoI} \pm \gamma_3 \tag{5.4}$$

$$t_l = t_I - \gamma_4, \quad t_u = t_I - \gamma_5 \tag{5.5}$$

where $\gamma_2 \geq \gamma_1 > 0$, $0 < \gamma_3 \leq \pi$ and $\gamma_5 \geq \gamma_4 > 0$ are design parameters. The axes of the cube can then be vectorized from the point of the cube that is closest to the origin, i.e. (t_l, F_l, θ_l), such that

$$t_p = \left[t_l : \frac{t_u - t_l}{\Delta - 1} : t_u \right]^T \tag{5.6}$$

$$F_p = \left[F_l : \frac{F_u - F_l}{\Delta - 1} : F_u \right]^T \tag{5.7}$$

$$\theta_p = \left[\theta_l : \frac{\theta_u - \theta_l}{\Delta - 1} : \theta_u \right]^T \tag{5.8}$$

where **:** represents an operator that creates a vector of Δ equally distanced points between the lower and upper limits. Δ is a non-zero integer representing the number of simulations per axis, which yields the resolution of the box to become Δ^3.

The applied proactive thrust vector can now be expressed as

$$\boldsymbol{\tau}_p(t) = \begin{cases} \boldsymbol{\tau}_p(F_p, \theta_p) & \text{if } t_p \leq t < t_I \\ 0 & else \end{cases} \tag{5.9}$$

which makes it act like a pulse from time t_p, to the time of impact t_I. It is assumed that t_I is available from the ice floe detection algorithm (Section 5.2.1), or that it can be obtained from the disturbance detection in Algorithm 6.2 if it was augmented to not regard the predictive force as a disturbance. The force vector (5.9) was calculated using the attached Matlab function *pred_force.m.*

5.4.1 Finding the Limits

As opposed to finding the appropriate limits by trial and error, which would be time consuming due to the number of possible parameters, it is proposed to simulate the predictive box with overestimated limits in order to find suiting γ values. The attached algorithm *find_box_limits.m* (see Appendix C) is then used to calculate if the Integral Square Error (ISE) (as explained in Section 7.1.7) is increased or reduced compared to without proactive action. Figure 5.4.1 was created with *predictive_sim_find_box_limits.m*, where the simulated vessel model is the same as the one that is used throughout the thesis (see Appendix B). The simulation model was *sim_prediction_report_test.slx* with a simulation length of 700 seconds. The controller used in every simulation in this chapter is the same as the PID+AFF controller in Chapter 7, and the applied wave is a JONSWAP spectrum created with the toolbox from [32], with modal frequency $\omega_0 = 1.1$ rad/s for each DOF, and significant wave height $H_s = 2.4$ meters. To focus on stationkeeping, $\boldsymbol{\eta}_d = 0$ was chosen throughout this chapter.

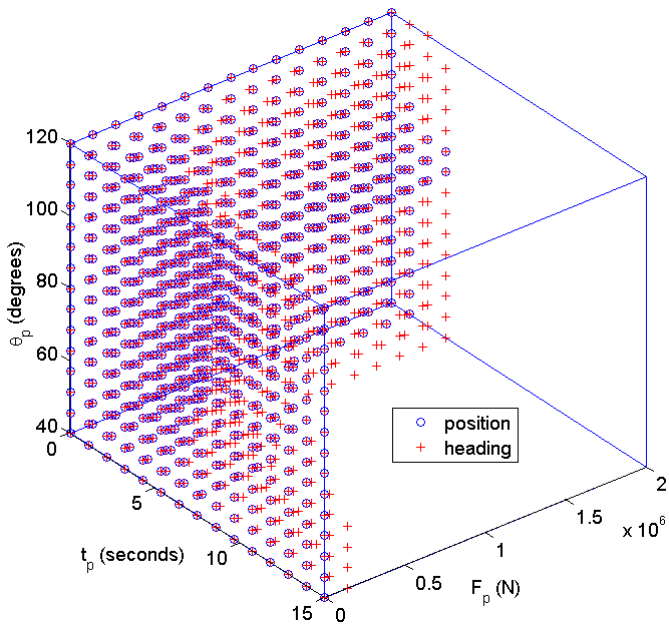

Figure 5.4.1: Simulation of predictive box with $\Delta = 15$, where the blue and red points represent coordinates that yield an improvement in position and heading ISE, respectively, subject to the disturbance force: $F_I = 1e5$, $\boldsymbol{p}^b_{I,CG} = \begin{bmatrix} 40 & 9 \end{bmatrix}^T$, $\theta_{AoI} = 80°$ at $t = 400$.

Figure 5.4.1 shows a simulation of the predictive box, where the following parameters were used: $\gamma_1 = .01$, $\gamma_2 = 20$, $\gamma_3 = .7$ (40 degrees), $\gamma_4 = .05$ and $\gamma_5 = 15$. As the vessel actuator time constant is 10 seconds (see Appendix B), t_p was thus chosen to vary from immediately before impact to 15 seconds before impact. F_p was varied from a small fraction of, to 20 times the incoming disturbance. θ_p was varied between $\theta_{AoI} \pm 40$ degrees as it should be enough to be well inside a plausible estimate error range.

The points in Figure 5.4.1 represent the combination of predictive variables that yields an improvement in position and heading ISE. It is shown that the predictive action generally improves both position and heading ISE when F_p is around the lower limit F_l for every t_p, as well as when t_p is around the lower limit t_l for every F_p. It can also be seen that the angle θ_p is relatively uninfluencing, expect for when F_p becomes large and t_p is not close to zero, where the position ISE is only improved in the range around $\theta_p = \theta_{AoI} \pm 10$ degrees.

It should be mentioned that at this angle and point of impact, an incoming disturbance with a magnitude of $F_I = 1e4 = 10$kN, or below, will barely affect the vessel as it would be a smaller disturbance than the applied wave forces. On the other hand, a magnitude of $F_I = 5e5 = 500$kN will make the system unstable, as the cor-

rective force required exceeds the limits of the thrusters. To explore the difference between a large and small incoming ice disturbance, two additional simulations are presented in Figures 5.4.2 and 5.4.3. Intuitively, for the large disturbance in Figure 5.4.2, a high F_p within a few seconds before impact yields improvements as the disturbance approaches the thruster limits, and thus maximum thrust is needed. For the small disturbance in Figure 5.4.3 however, too much force too long before impact, will be overcompensating. As shown in all simulations this far, the angle θ_p has little effect, and as shown in the figures in Appendix D.1.1, the effect of the predicted point of impact is also negligible compared to the choice of F_p and t_p. Therefore, by holding θ_p and $\boldsymbol{p}_p^b$ constant as they can be assumed to be measured with high accuracy, the proactive time and force can then be simulated against the magnitude of the incoming force.

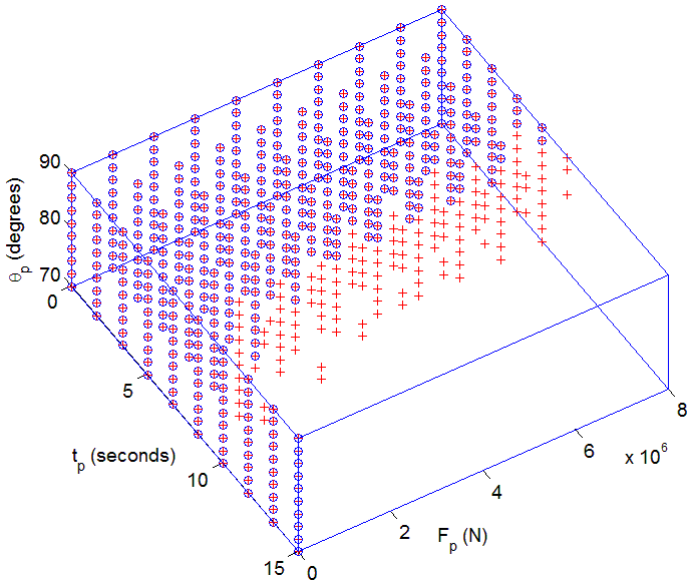

Figure 5.4.2: Simulation of predictive box with $\Delta = 10$, and with the disturbance force: $F_I = 4e5$, $\boldsymbol{p}_{I,CG}^b = \begin{bmatrix} 40 & 9 \end{bmatrix}^T$, $\theta_{AoI} = 80°$.

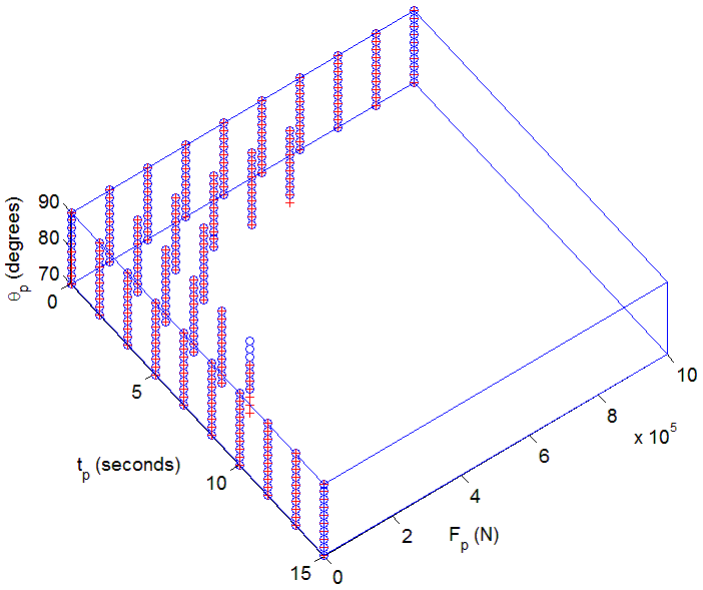

Figure 5.4.3: Simulation of predictive box with $\Delta = 10$, and with the disturbance force: $F_I = 5e4$, $\boldsymbol{p}^b_{I,CG} = \begin{bmatrix} 40 & 9 \end{bmatrix}^T$, $\theta_{AoI} = 80°$.

Figure 5.4.4 shows that the proactive action improves both position and heading ISE for both small and large disturbances when force is applied shortly before the disturbance occurs. The box is thus reduced, such that $\gamma_5 = 5$ seconds, while the limits $\gamma_{1,2}$ for F_p are left unchanged, since for small disturbances, a large γ_2 yields full thrust; while for large disturbances, everything from $\gamma_2 > 1$ to $\gamma_2 \gg 1$ will yield full thrust. Figure 5.4.5 created with the *find_box_limits_worse* algorithm, shows where the proactive action worsens either the position or heading ISE. It also illustrates that either t_u or γ_2 must be reduced to end up with a predictive box that yields improvements for all magnitudes F_I. To decide whether to reduce t_p, γ_2, or both, Figure 5.4.6 shows a contour plot (created with *predictive_sim_time_vs_force_contour.m*) of the position ISE for a disturbance of magnitude $F_I = 4e4$, since as shown in Figure 5.4.5, the small disturbance is more sensitive to the predictive force. Figure 5.4.6 shows that the wrong combinations of proactive action yields almost 20 times worse performance than without. It also shows that the maximal advantage lies somewhere below $t_p = 1$ or $\gamma_2 = 5$, where the white curved range in the middle represents the bottom as it has no contour lines. As t_p is already relatively small, and since a too high γ_2 will eventually saturate the thrusters, the box was reduced by choosing $\gamma_2 = 5$.

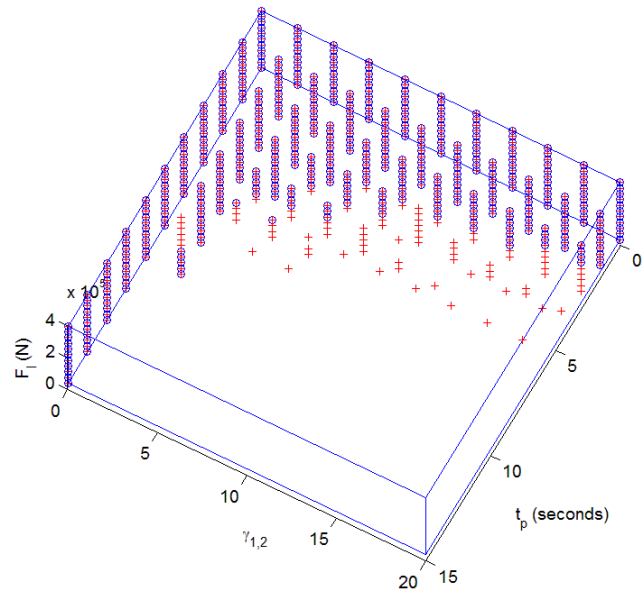

Figure 5.4.4: Simulation of predictive box with $\Delta = 11$, and with varying disturbance force: from $F_I = 4e4$ to $F_I = 4e5$, $\boldsymbol{p}^b_{I,CG} = \begin{bmatrix} 40 & 9 \end{bmatrix}^T$, $\theta_{AoI} = 80°$.

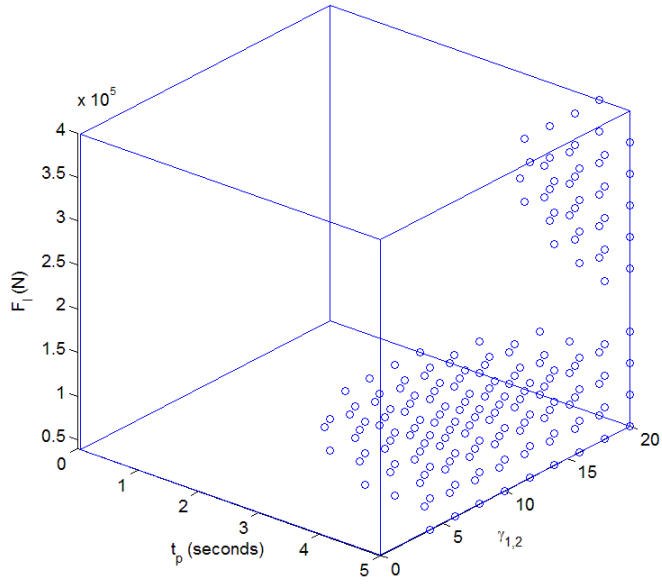

Figure 5.4.5: Simulation of predictive box, $\Delta = 11$, with varying disturbance force: $F_I = 4e4$ to $F_I = 4e5$, $\boldsymbol{p}^b_{I,CG} = \begin{bmatrix} 40 & 9 \end{bmatrix}^T$, $\theta_{AoI} = 80°$. The points represent the coordinates where the predictive action worsens the position or heading ISE.

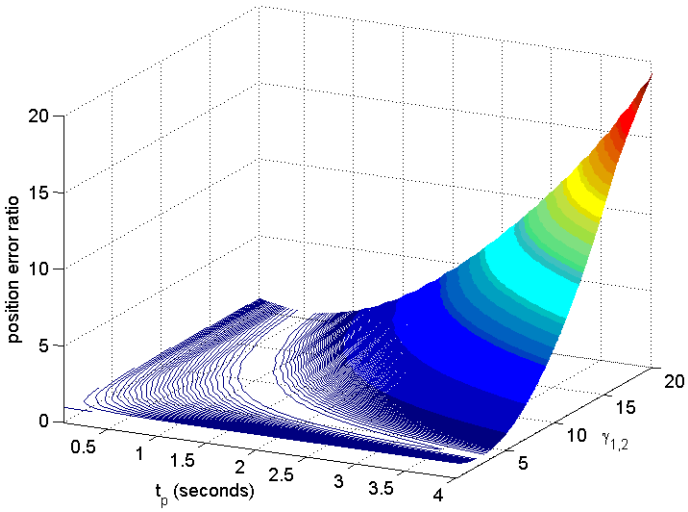

Figure 5.4.6: Contour plot of the position ISE for t_p vs F_p, $\gamma_2 = 20$, where the z axis represents the ratio of the position ISE without and with proactive action, such that a height less than 1 represents an improvement. Ice disturbance force: $F_I = 4e4$, $\boldsymbol{p}^b_{I,CG} = \begin{bmatrix} 40 & 9 \end{bmatrix}^T$, $\theta_{AoI} = 80°$.

The contour plot of the reduced predictive box is shown in Figure 5.4.7, where it can be seen that every value of the position ISE ratio lies beneath 1, i.e. every combination of t_p and F_p yields an improvement. However, it becomes clear that the lower limits, t_l and γ_1 can be raised as they barely yield improvements, represented by the red contours in the figure. It can also be seen that the error steeply rises in the upper corner (t_u,F_u), so the new limits are now proposed as $\gamma_4 = 1.5$, $\gamma_4 = 3.5$, $\gamma_1 = 1$ and $\gamma_2 = 3.5$. Figure 5.4.8 shows the contour plot of the final predictive time and force. By choosing the fixed time and force $t_p = t_I - \gamma_t = t_I - 2.5$ and $F_p = \gamma_f F_I = 2.25 F_I$, where γ_t and γ_f are the fixed predictive parameters for time and force, respectively, the proactive action will lie in the middle of the box. This means that an underestimate of the incoming ice force yields an error ratio that goes toward 1, i.e. the effect of the predictive action goes toward zero, while an overestimate of the incoming force yields an error ratio that goes toward the minimal error ratio. Choosing $\gamma_f = 2.25$ means that an estimate of F_I within $\pm 55\%$ of the actual incoming ice force will yield results within the box. Underestimates below -55% are not of concern, as they will yield a ratio that approaches 1, while overestimates over 55% will yield ratios that may rise above 1. A safer choice of γ_f, e.g. $\gamma_f = 1$ such that $F_p = F_I$, will have overestimates of F_I up to 350% inside the box, but will then have a reduced effect from the proactive action for more accurate estimates. This means that γ_f must be tuned according to the observed accuracy of the estimated incoming ice force, e.g. by letting

$$\gamma_f = \frac{\gamma_2}{1 + \alpha} \tag{5.10}$$

where α can e.g. be chosen as twice the standard deviation of an observed ice

magnitude estimate distribution, which will ensure that the predictive force lies within the box with a confidence of about 95%.

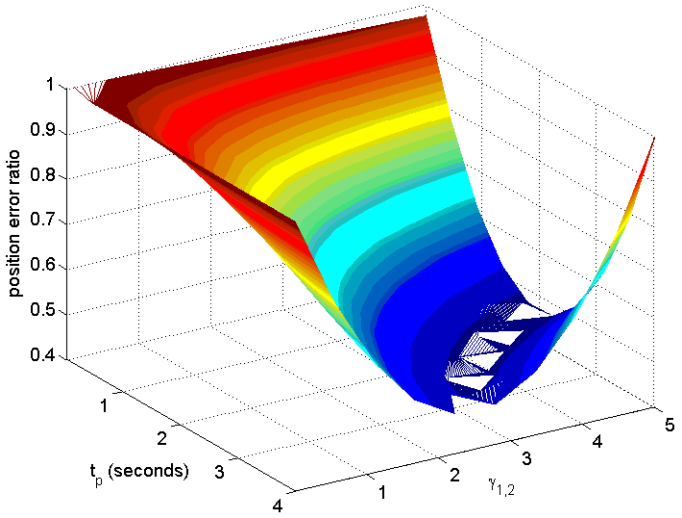

Figure 5.4.7: Contour plot of the position ISE for t_p vs F_p, $\gamma_2 = 5$. Ice disturbance force: $F_I = 4e4$, $\boldsymbol{p}^b_{I,CG} = \begin{bmatrix} 40 & 9 \end{bmatrix}^T$, $\theta_{AoI} = 80°$.

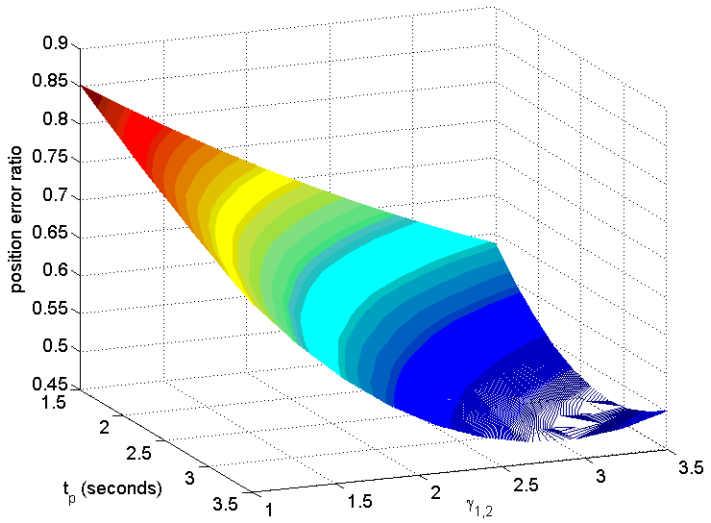

Figure 5.4.8: Contour plot of the position ISE for t_p vs F_p, $\gamma_1 = 1$, $\gamma_2 = 3.5$, $\gamma_4 = 1.5$, $\gamma_4 = 3.5$. Ice disturbance force: $F_I = 4e4$, $\boldsymbol{p}^b_{I,CG} = \begin{bmatrix} 40 & 9 \end{bmatrix}^T$, $\theta_{AoI} = 80°$.

5.4.2 Verifying the Limits

Additional contour plots of ice incoming almost straight on the corner of the stern, and almost straight on the beam near CG, are shown in Appendix D.1.2, to illustrate the performance of the predictive box in other cases. Contour plots of position and heading ISE are also found in Appendix D.1.2.3, showing the error ratios for predictive heading vs force with a fixed t_p. As expected, the plots illustrate that a choice of $\theta_p = \theta_{AoI}$ yields the best results, as also visualized in Figure 5.4.9. However, an issue arises when the ice floe hits straight on the beam near CG. This kind of impact will produce force in sway, but little torque is produced as the lever arm is short. This means that the position is very susceptible to predictive force, while the heading is not. This can be seen in Figure 5.4.10, where an accurately applied predictive force only yields about 4% improvement on the heading, while for poor estimates of θ_{AoI}, the resulting heading is worsened by proactive action. This is due to the fact that around CG, poor estimates can cause the predictive moment to be applied in the wrong direction. A possible solution could be to not apply any proactive torque if the estimated $\boldsymbol{p}^b_{I,CG}$ lies within a range around CG, or in general if the combination of $\boldsymbol{p}^b_{I,CG}$ and θ_{AoI} yields a small predicted torque.

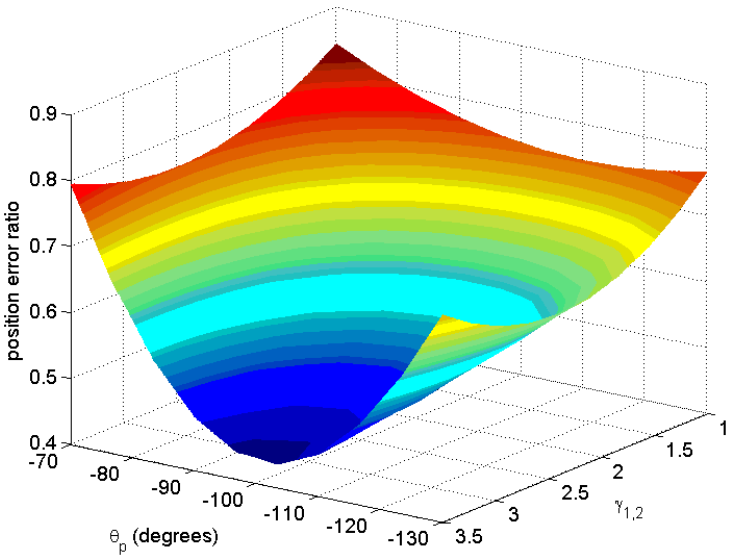

Figure 5.4.9: Contour plot of the position ISE for θ_p vs F_p, $t_p = 2.5$. Small ice disturbance force: $F_I = 5e4$, $\boldsymbol{p}^b_{I,CG} = \begin{bmatrix} -5 & -9 \end{bmatrix}^T$, $\theta_{AoI} = -100$.

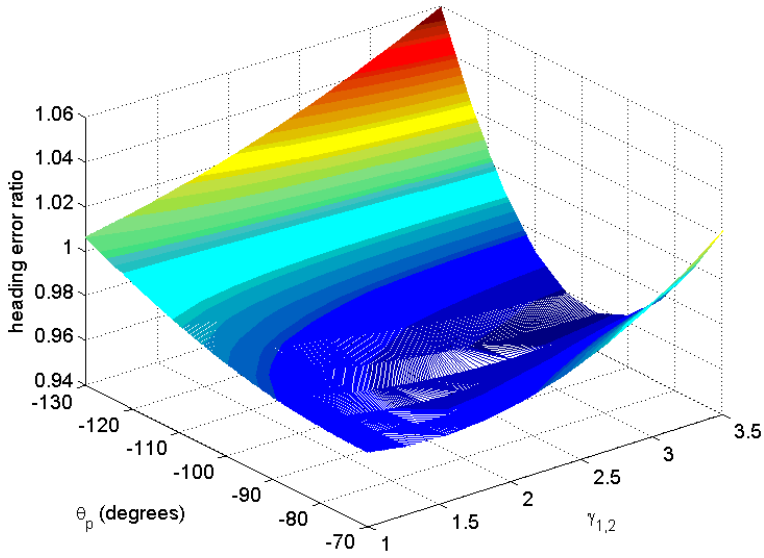

Figure 5.4.10: Contour plot of the heading ISE for θ_p vs F_p, $t_p = 2.5$. Small ice disturbance force: $F_I = 5e4$, $\boldsymbol{p}^b_{I,CG} = \begin{bmatrix} -5 & -9 \end{bmatrix}^T$, $\theta_{AoI} = -100$.

The last step is to verify the early assumption stating that the predicted point of impact and angle were not very influential. As seen in Figure 5.4.11, for an impact near the corner of the beam, the proactive action will yield improvements for both heading and position as long as θ_p is within $\theta_{AoI} \pm 40$ degrees. Concerning the predicted point of impact, $\boldsymbol{p}^b_p$, Figure 5.4.12 illustrates that the only area where the predictive force does not improve neither position nor heading ISE, is the small box from approximately beneath -20 meters off $\boldsymbol{p}^b_{I,CG}$, beneath -50 degrees off θ_{AoI} and above $\gamma_2 \approx 2.5$. In the other areas where θ_p is outside of $\theta_{AoI} \pm 40$ degrees, Figure 5.4.12 shows that either the position ISE, heading ISE or sometimes both, were improved. Notice that $\boldsymbol{p}^b_p$ was varied from -30 to only 10 meters, as any further would yield an impact point in front of the vessel.

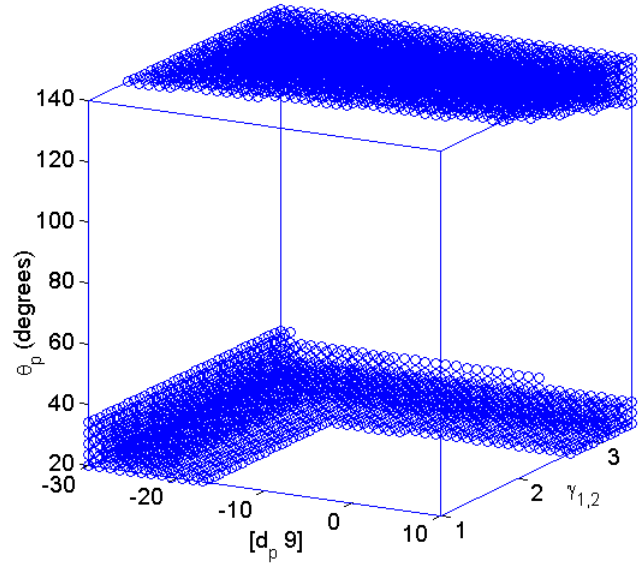

Figure 5.4.11: Simulation of predictive box with fixed time $t_p = 2.5$, $\Delta = 35$, disturbance force: $F_I = 4e4$, $\boldsymbol{p}^b_{I,CG} = \begin{bmatrix} 40 & 9 \end{bmatrix}^T$, $\theta_{AoI} = 80°$. The points represent coordinates where the predictive action worsens the ISE.

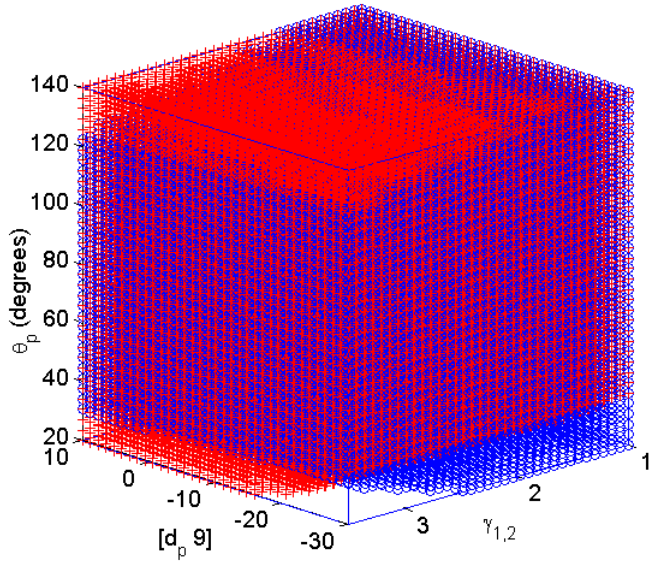

Figure 5.4.12: Simulation of predictive box with fixed time $t_p = 2.5$, $\Delta = 35$, disturbance force: $F_I = 4e4$, $\boldsymbol{p}^b_{I,CG} = \begin{bmatrix} 40 & 9 \end{bmatrix}^T$, $\theta_{AoI} = 80°$. The blue points represent position ISE improvements, while the red represent heading ISE improvements.

As mentioned above, a more challenging case is when $\boldsymbol{p}^b_{I,CG}$ is close to CG, and as shown in Figure 5.4.13, the accuracy of $\boldsymbol{p}^b_p$ only influences the improvement of the heading. Figure 5.4.14 shows that the heading is only improved for certain combinations of predicted heading and position, while it is significantly worsened for the wrong combinations. This again suggest the need for withholding predictive moment when the combination of the predicted point of impact and the angle of impact leads yields a small moment.

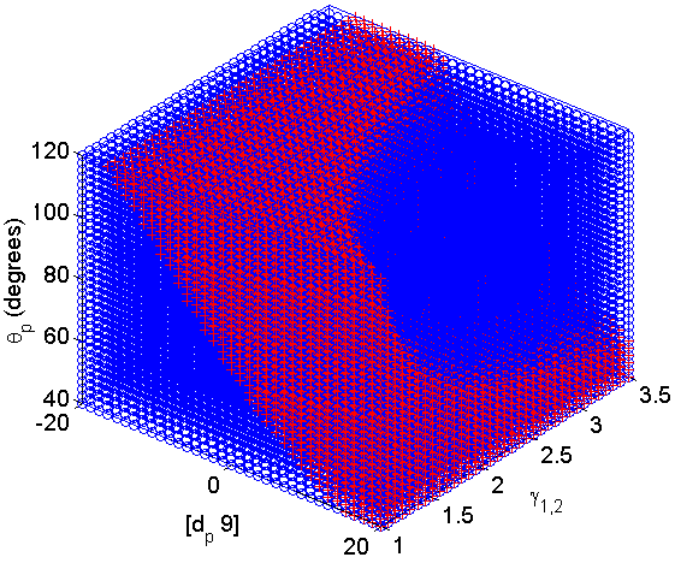

Figure 5.4.13: Simulation of predictive box with fixed time $t_p = 2.5$, $\Delta = 35$, disturbance force: $F_I = 4e4$, $\boldsymbol{p}^b_{I,CG} = \begin{bmatrix} 4 & 9 \end{bmatrix}^T$, $\theta_{AoI} = 80°$. The blue points represent position ISE improvements, while the red represent heading ISE improvements.

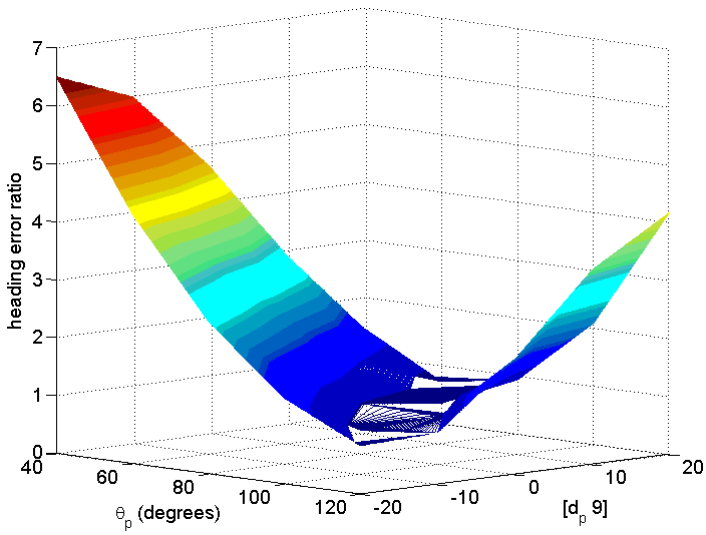

Figure 5.4.14: Contour plot of the heading ISE for θ_p vs $\boldsymbol{p}_p^b$, and predictive time and force fixed at $t_p = 2.5$ $\gamma = 2.25$. Small ice disturbance force: $F_I = 4e4$, $\boldsymbol{p}_{I,CG}^b = \begin{bmatrix} 4 & 9 \end{bmatrix}^T$, $\theta_{AoI} = 80$.

Chapter 6

Wave Filtering

As previously mentioned, the total motion of a marine vessel can be modeled as the sum of low-frequency (LF) and wave-frequency (WF) motions. The LF motion represents the motion of the vessel and slow-varying disturbances, while the WF motion represents a high-frequency wave-induced motion. The WF motion is a rapidly oscillating, zero mean motion with the same frequency as the incoming wave train, and it is thus a useless task to try to compensate for these motions [25]. In addition, attempts to compensate would lead to excessive wear and tear on actuators and rudders, which in turn will lead to increased fuel consumption. Including wave-filtering to cancel out these motions is therefore a very important part of a DP control system [31].

Wave filters are usually incorporated in model-based state observers, where linear models for first-order wave-induced motions are used to estimate WF motion. Earlier, wave filters consisted of low-pass or notch-filters to reduce thruster wear caused by WF motion. However, these techniques introduce phase lag around the cut-off frequency, which usually leads to limited controller performance due to a decreased phase margin [40].

This thesis was written with the intention of using state estimates provided by [41]. The observer in [41] is a model-free IMU-based Dynamic Positioning state estimator, which by this date does not include a wave filter. This means that wave filtering had to be done between the observer and the applied feedback, such that WF motions would not enter the feedback loop. If the controller was linear, the wave filter could be implemented either before or after the controller, but because of the nonlinearities in the controller, this would not yield the same result. Consequently, the placement of the wave filter will be explored and discussed through this chapter.

Introducing model-based wave filtering of estimates from a model-free observer will in a way defeat the purpose of the model-free observer, as it would estimate the total motion twice. Therefore, a model-free wave-filter will be explored and

simulated.

6.1 Simple Wave Filtering

6.1.1 Low-pass Filter

The simplest form of wave filtering is done using a low-pass filter. Introducing a first-order low-pass filter as

$$h_{lp}(s) = \frac{1}{1+Ts} \tag{6.1}$$

where $T = 1/\omega_c > 0$ is the time constant and ω_c is the cut-off frequency. The low-pass filter will suppress forces over the cut-off frequency ω_c, while introducing a phase lag that approaches 90 degrees. The problem with first-order low-pass filters arises when the wave frequency falls close to the control bandwidth of the vessel. Wave frequencies typically lie in the interval [1]

$$0.05 \text{ Hz} < f_0 < 0.2 \text{ Hz} \tag{6.2}$$

or equivalently

$$0.3 \text{ rad/s} < \omega_0 < 1.3 \text{ rad/s} \tag{6.3}$$

where f_0 is the wave-frequency in Hertz and ω_0 is the wave-frequency in rad/s. As the control bandwidth is typically chosen around 0.1 rad/s for large marine vessels [1], it will fall below the wave frequency. However, the bandwidth of the actuators typically lies in the frequency range of the wave forces, so filtering must be applied to reduce wear and tear. The problem with first-order low-pass filtering comes from the fact that their frequency response is relatively flat. To sufficiently attenuate the wave-forces, the cut-off frequency must be placed way below the wave frequency. This is better visualized in Figure 6.1.1, where the frequency response of two first-order low-pass filters with different cut-off frequencies have been plotted against an inverted JONSWAP wave spectrum with significant wave height $H_s = 4.8$ meters, modal frequency $\omega_0 = 0.3$ rad/s and peakedness factor $\gamma = 3.3$. The JONSWAP spectrum was found by the second-order transfer function approximation in (2.1) where the constants σ and λ were found using *wavespec.m* from the MSS Toolbox [32]. The frequency response was then inverted to illustrate how much suppression that is needed. It should be mentioned that the modal frequency was put far to the left to illustrate the possible impact on the controller bandwidth.

Figure 6.1.1 shows that a first-order low-pass filter with the same cut-off frequency as the dominating wave frequency (modal frequency), will barely attenuate the wave-induced forces. Moving the cut-off frequency down to $\omega_c = 0.1$ rad/s will be sufficient to suppress this wave spectrum, but then at the cost of moving into the control bandwidth. Although it would suppress the wave forces, it would also suppress some of the control forces, and thus lead to decreased performance. This problem can be solved by introducing a higher-order low-pass filter, as it would yield a steeper frequency response, such that the cut-off frequency could be placed closer to the modal frequency (as seen in Figure 6.1.1). However, a higher-order

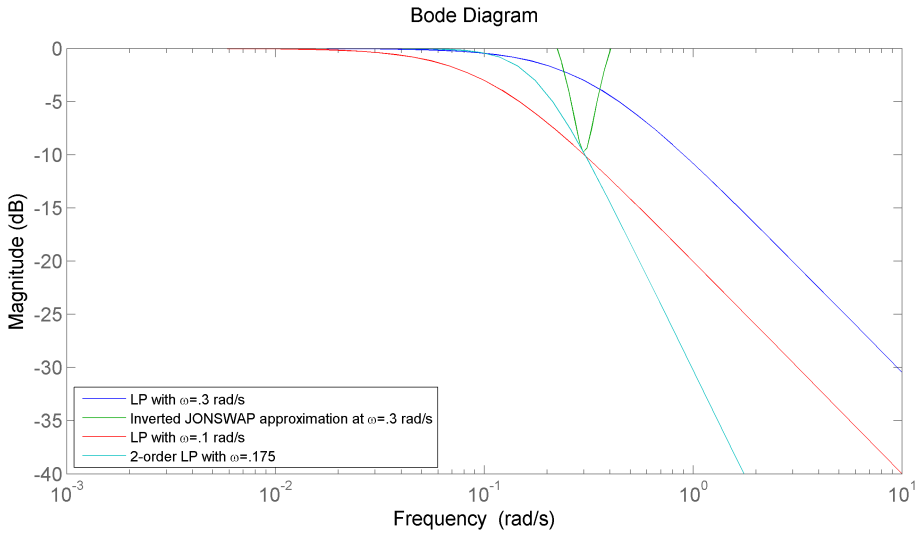

Figure 6.1.1: Bode plot of inverted JONSWAP wave spectrum vs low-pass filters.

filter comes with the cost of additional phase lag, as each order adds another 90 degrees.

6.1.2 Notch Filter

A better approach for wave filtering is the use of a notch filter. The notch filter is sometimes implemented in cascade with a low-pass filter to also remove frequencies that lie above the wave-frequency, but it is assumed that frequencies higher than waves will be removed by the observer. A notch filter will attenuate the frequency range around the notch frequency ω_n, while leaving other frequency unaltered. The lowest available order of notch filters is second-order, and may e.g. take the form [42]

$$h_{n1}(s) = \frac{s^2 + \omega_n^2}{s^2 + \frac{\omega_n}{Q_1}s + \omega_n^2} \tag{6.4}$$

or as [1]

$$h_{n2}(s) = \frac{s^2 + 2\zeta_2\omega_n s + \omega_n^2}{(s + \omega_n)^2} \tag{6.5}$$

where ζ_2 is the relative damping ratio, ω_n is the notch frequency and $Q_1 = 1/2\zeta_1$ is the quality factor that determines the width of the notch. Notice that the two filters will be equal for $\zeta_2 = 0$ and $Q_1 = 0.5$. By studying the Bode plot of the two filters in Figure 6.1.2, it can be noticed that the damping in the numerator of $h_{n2}(s)$ reduces the magnitude and phase of the notch, compared to $h_{n1}(s)$. As seen in the figure, both filters will attenuate the wave forces, but while $h_{n1}(s)$ will suppress more magnitude than what is needed, $h_{n2}(s)$ will also suppress a much wider frequency range, and thus also suppress more of the control forces. This

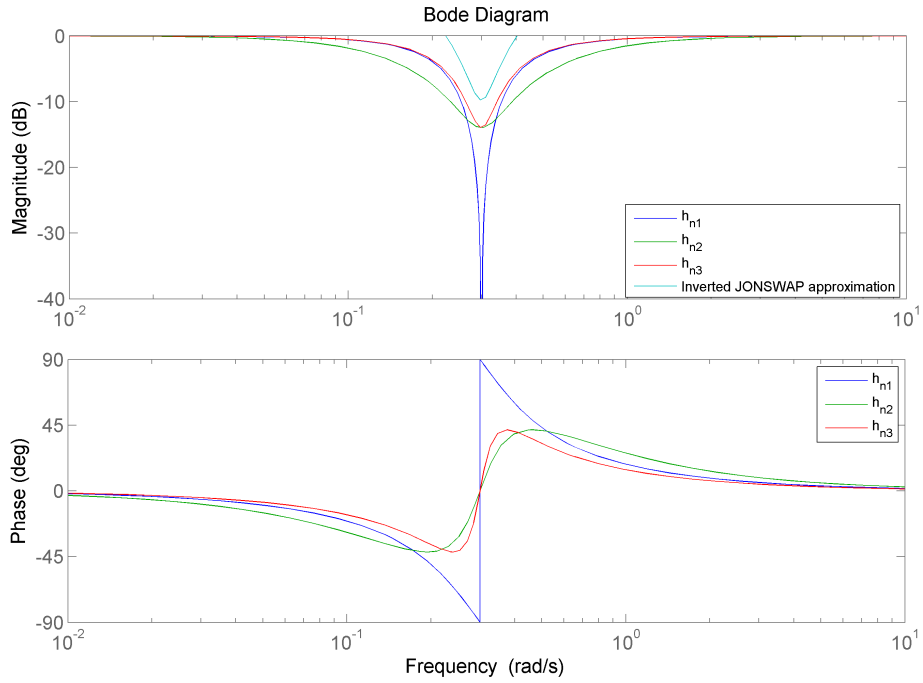

Figure 6.1.2: Bode plot of $h_{n1}(s)$, $h_{n2}(s)$ and $h_{n3}(s)$, with inverted JONSWAP approximation. $\omega_n = 0.3$ rad/s, $Q_1 = Q_3 = 1$, $\zeta_2 = 0.2$, $\zeta_3 = 0.1$ and same JONSWAP parameters as in Section 6.1.1.

resembles the first-order low-pass filters compared with the higher order ones, as $h_{n2}(s)$ has a flat magnitude response, while $h_{n1}(s)$ is much steeper at the cost of more phase. A possible compromise would then be to combine the properties, to form a third type of notch filter, proposed as

$$h_{n3}(s) = \frac{s^2 + 2\zeta_3\omega_n s + \omega_n^2}{s^2 + \frac{\omega_n}{Q_3}s + \omega_n^2} \tag{6.6}$$

which has the damping ratio ζ_3 in the numerator from (6.5) and the quality factor Q_3 from (6.4) to control the width. As seen in Figure 6.1.2, the depth of the magnitude and the maximal phase for $h_{n3}(s)$ is the same as for $h_{n2}(s)$, while the steepness of the magnitude is the same as for $h_{n1}(s)$ such that the control bandwidth is not attenuated as much. This is also visualized in the phase plot, where it is shown that the phase of $h_{n3}(s)$ is lower around the control bandwidth frequency.

6.1.2.1 Cascaded Notch Filter

The problem with the notch filter is that it only covers a small frequency range. As the actual wave-frequency is uncertain, the problem of where to place the notch

frequency ω_n arises. One alternative is to use a cascaded filter structure, where two or more notch filters with different frequencies are cascaded to form the filter

$$h_{n4}(s) = \prod_i \frac{s^2 + 2\zeta_i \omega_i s + \omega_i^2}{s^2 + \frac{\omega_i}{Q_i} s + \omega_i^2} \tag{6.7}$$

As seen in Figure 6.1.3, three notch filters with logarithmic increasing frequency are cascaded to cover a wider frequency band. Around the control bandwidth, the magnitude of the notch is unchanged, while the phase has dropped by roughly 10 degrees compared to $h_{n3}(s)$. The notch has now become so wide that it will attenuate wave-frequencies from about 0.3 rad/s to 0.83 rad/s, at the cost of some added phase. The range could be widened to cover the whole expected wave-frequency range, but then even more phase would be added, as it would either require a smaller damping ratio ζ or one or more additional filters in cascade, to sufficiently suppress the wave force. For a higher sea state, i.e. increased significant wave height H_s, the damping could be reduced to deepen the magnitude of the notch, but then again at the price of added phase.

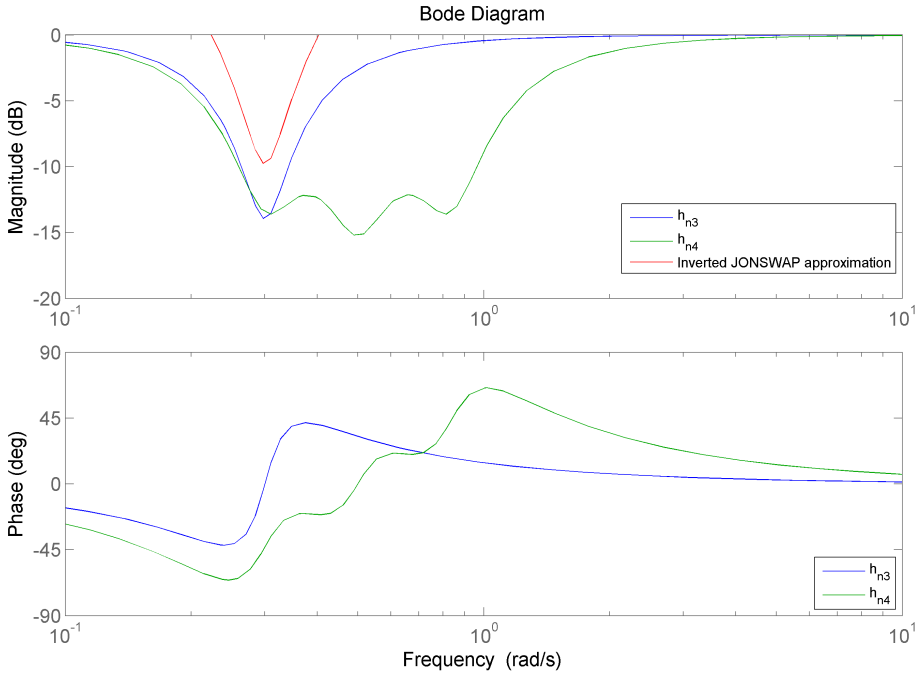

Figure 6.1.3: Bode plot of $h_{n3}(s)$, $h_{n4}(s)$, and inverted JONSWAP approximation. $\omega_n = 0.3$ rad/s, $Q_3 = 1$, $\zeta_3 = 0.1$. For $h_{n4}(s)$, $\omega_1 = 0.3$, $\omega_2 = .5$, $\omega_3 = .83$ rad/s, and $Q = 1$ and $\zeta = 0.15$ were chosen in each of the three cascaded filters.

6.2 Adaptive Notch Filtering

Another way to handle the problem of where to place the notch frequency, is to adapt ω_n using e.g. a frequency tracker. If the estimate is good, a single notch filter with a relatively narrow notch can be applied to attenuate the wave forces, which would lead to a small phase lag. A frequency tracker algorithm is proposed as follows:

Algorithm 6.1 Frequency Tracker Algorithm for estimation of the wave-frequency

1. Run the signal through a high-pass filter with cut-off frequency $\omega_c = 0.3$ rad/s
2. Differentiate the high-pass filtered signal
3. Mark when filtered signal goes from positive to negative as $temp1$
4. Mark when filtered signal goes from negative to positive as $temp2$
5. Set $\omega_n = \pi|\frac{1}{temp2-temp1}|$
6. Saturate the output as $0.3 < \omega_n < 1.3$ rad/s
7. Run the saturated frequency through a low-pass filter, where the initial condition of the integrator is ω_n

6.2.1 Explanation of Algorithm 6.1

The purpose of first two steps in the algorithm is to pre-process the signal, to extract the WF component from the signal. The first step is a high-pass filtering of the signal, which will extract the wave-frequency component from the total force or motion. The signal is then differentiated to determine where the signal rises and fall due to the waves, as some LF residues will still exist. This can be seen in Figure 6.2.2.

Step 3-5 is the frequency counter, which by the use of flags and temporary variables, measures the period T of the wave by marking when it switches from negative to positive and vice versa. As the period of a sine wave is twice the duration of one zero-crossing to the next, and as the frequency f is the inverse of the period, the frequency estimate becomes

$$f = \frac{1}{T} = \frac{1}{2}\left|\frac{1}{temp2 - temp1}\right| \tag{6.1}$$

where the absolute value is to prevent negative frequency estimates. The angular frequency ω is defined as

$$\omega = 2\pi f \tag{6.2}$$

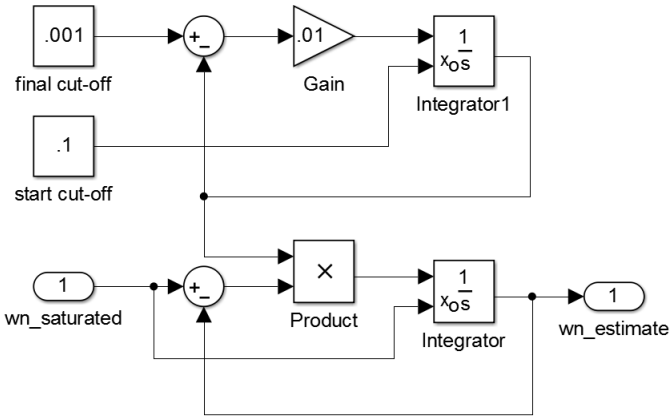

Figure 6.2.1: Low-pass smoothing filter with decreasing cut-off frequency from 0.1 rad/s to 0.001 rad/s.

such that the angular frequency estimate becomes

$$\omega_n = 2\pi f = \pi \left| \frac{1}{temp2 - temp1} \right| \tag{6.3}$$

Step number 6 is to prevent the estimate from traveling outside the predefined wave-frequency range, i.e. $0.3 < \omega_0 < 1.3$ rad/s. The saturation also has the advantage that when external disturbances influence the motion of the vessel, the wave-frequency estimate is not that affected (as seen in Figure 6.2.3).

The purpose of the low-pass filter in step 7 is to smooth out the discrete estimate, and as seen in Figure 6.2.3, the estimate quickly converges to the applied wave-frequency. The filter is implemented with a decreasing cut-off frequency (as illustrated in Figure 6.2.1), such that it initializes by quickly converging to the correct frequency, and then slows down to better hold the estimate. Notice that every form of phase lag due to filtering in this algorithm will not affect the feedback loop. The only phase lag that enters the feedback loop, is the phase that comes from the actual notch wave filter.

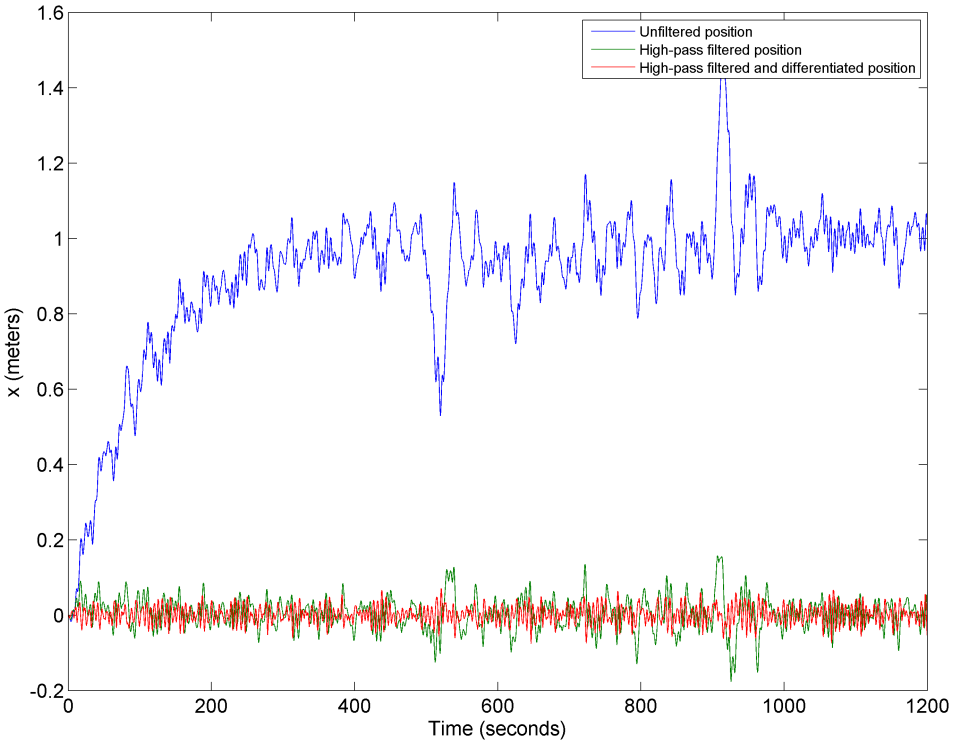

Figure 6.2.2: The first two steps of the Frequency Tracker algorithm, where the top figure is the unfiltered total motion of the position in the x direction, vs the high-pass filtered and differentiated extracted wave-frequency component. An external disturbance is added from $t = 500$ to $t = 900$.

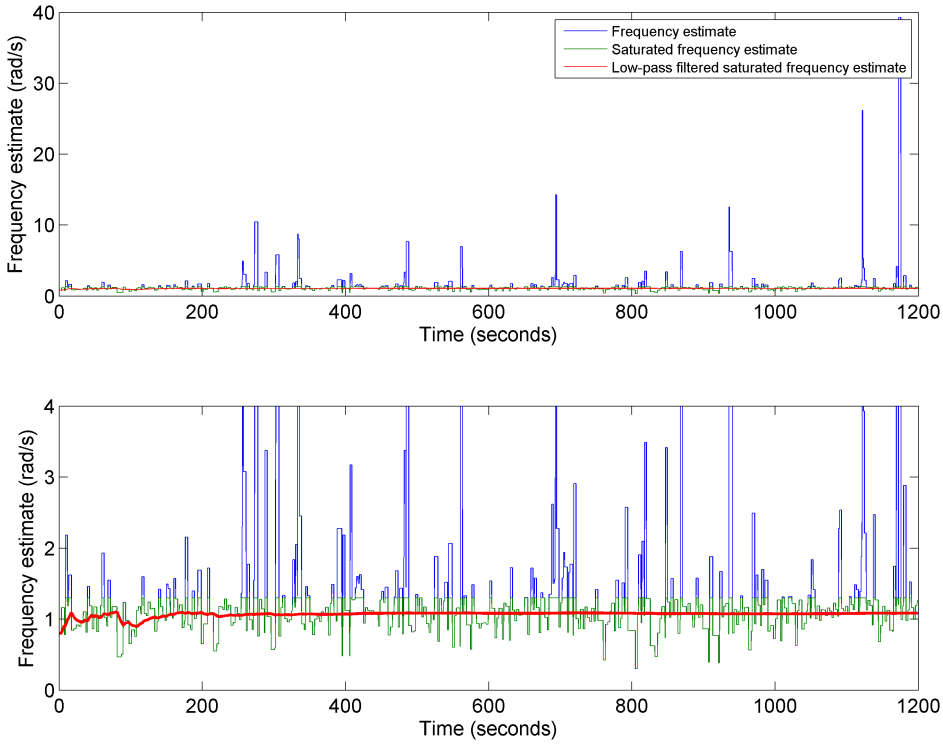

Figure 6.2.3: Steps 3-7 of the Frequency Tracker algorithm, where the top figure is the wave-frequency estimate vs the saturated and low-pass smoothed estimate, and the bottom figure is a snippet to illustrate the advantage of the saturation and the low-pass smoothing. The applied wave is a JONSWAP distribution with modal frequency $\omega_0 = 1.1$ rad/s and significant wave height $H_s = 2.4$ m. An external disturbance is added from $t = 500$ to $t = 900$.

6.2.2 Effect of the Adaptive Notch Filter

As the proposed algorithm display good estimates for the wave-frequency, the applied notch wave filter can then be chosen to be narrow, to only attenuate a small frequency range around the estimate, and thus provide minimal phase-lag. To explore how the wave filter affects the applied thrust and posture (i.e. position and heading) of the vessel, a simulation was executed without external disturbances, with $\eta_d = 0$ and where the applied wave is a JONSWAP distribution with modal frequency $\omega_0 = 1.1$ rad/s for each DOF, and significant wave height $H_s = 2.4$ meters. This H_s represents a sea state code 4 (moderate), which according to [43] is the most commonly experienced sea state worldwide as well as in the North Sea.

As seen in Figure 6.2.4, the applied thrust is significantly reduced in surge and sway, while it is smoothed out in yaw. This is caused by the decreased amplitude of the wave component in each measurement of $\boldsymbol{\eta}$, due to the attenuation of

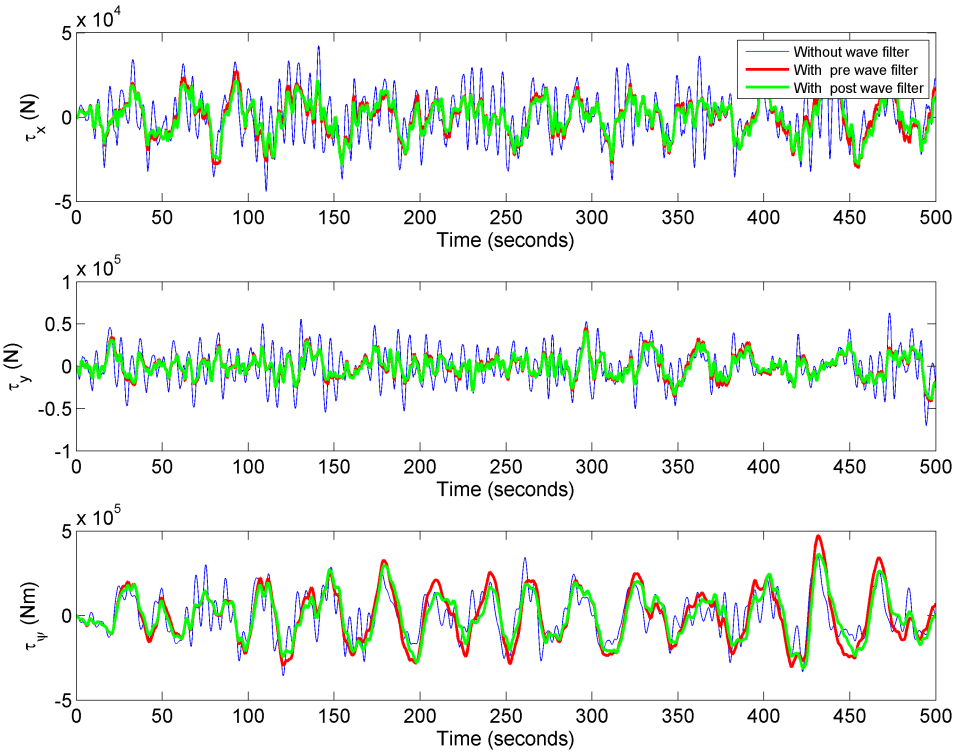

Figure 6.2.4: Plot of applied thruster force without and with wave filtering, subject to a wave disturbance.

wave forces. As residues of the wave-frequency will always endure, there are still oscillations in the thrust, but the actual wear and tear of actuators will be reduced.

The effect of the wave filter on the posture is shown in Figure 6.2.5, where it can be seen that the difference between the filtered and unfiltered signals is of small magnitude. The phase lag introduced by the notch filter causes the slowly varying oscillations. These oscillations are not wave-frequency induced, but as the plot displays the difference between the non-filtered and filtered posture, the oscillations represent the buildup of phase lag induced errors at the occurrence of large amplitude waves. It can also be noticed that the post-controller wave filtered posture lags behind the pre-controller signal. This is due to the thruster feedback into the acceleration feedforward controller, which means that the control output is filtered twice, thus leading to twice the phase lag.

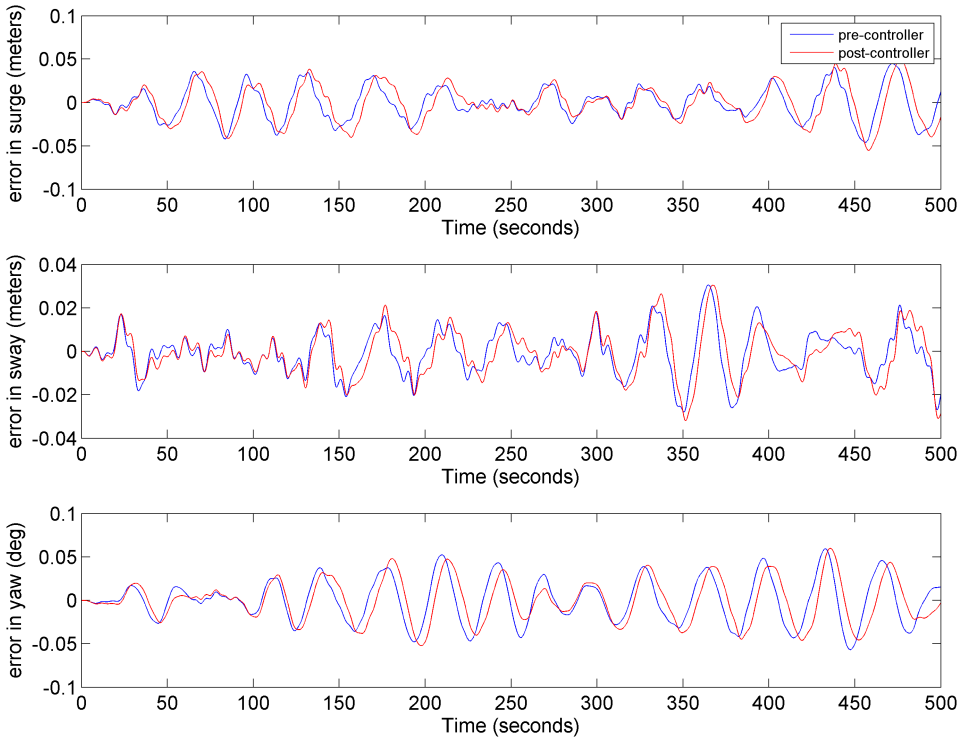

Figure 6.2.5: Plot of the difference between unfiltered and wave filtered posture (position and heading), subject to a wave disturbance.

6.2.2.1 ISE Comparison

The effect of the notch filter can also be illustrated by looking at the Integral Square Error (ISE) and Integral Square Output (ISO) (as more elaborately explained in Section 7.1.7). A high-pass filter, similar to the one used in the wave-filter, was applied to the thrust output, such that only the excessive thrust applied to counteract the waves was measured. Without this, a thrust compensation of an error that does not oscillate around zero, would dominate the ISO, and thus invalidate the analysis. The applied thrust that is of interest, is that which oscillates due to waves and the influence of other external forces, and thus a high-pass filtered thrust output will reflect the wear and tear on the actuators.

As seen in Table 6.2.1, the wave filtering caused the ISE for x, y and ψ to increase for both placements of the wave filter. The maximal position error, i.e. $\max\left(\sqrt{(x(t)-x_d)^2+(y(t)-y_d)^2}\right)$, was also affected with an increase. However, the thrust ISO was greatly reduced for surge and sway, while the yaw moment for the pre-controller placement was not that affected. The post-controller placement experienced a significant reduction in ISO for all DOFs. The different placement performances were similar concerning ISE, while the post-controller placement was

overall better for ISO. This illustrates the essence of the wave filter, where the applied thrust is greatly reduced at the cost of some loss of position and heading performance due to added phase lag.

	x ISE	y ISE	ψ ISE	max pos error	τ_x ISO	τ_y ISO	τ_N ISO
pre-controller	1.67	1.40	1.74	1.26	0.33	0.29	0.99
post-controller	1.71	1.40	1.59	1.25	0.28	0.25	0.73

Table 6.2.1: Ratio between ISE with and without wave filtering for position and heading, maximal position error and ratio between ISO with and without wave filtering for high-pass filtered applied forces and moments, when vessel is influenced by waves. A ratio below 1 represents an improvement.

6.3 Selective Wave Filtering

The challenge of wave filtering arises when unknown external disturbances are introduced. By adding some ice-inspired forces (as more elaborately explained in Section 7.1.1) from $t = 150$ to $t = 300$, with the ice-disturbance gain $\begin{bmatrix} 4e4 & 4e4 & 4e6 \end{bmatrix}^T$ and offset $\begin{bmatrix} -2e5 & 3.5e5 & 5e6 \end{bmatrix}^T$, it can be seen in Figure 6.3.1 that the wave filtered thrust increases as the ice hits and leaves the vessel, compared to the unfiltered thrust. The phase lag becomes a problem when sudden external disturbances occur, as the controller does not respond quickly enough. This is also illustrated in Figure 6.3.2, where the wave filtering causes the difference between the unfiltered and filtered posture to increase considerably. Some underdamped behavior can be also observed in the non-filtered thrust response, which is amplified by the filters due to the added phase. This may suggest a too aggressive proportional gain or a too soft damping gain.

The effect of the ice disturbance is even more clearly portrayed in Table 6.3.1, where the ISE and ISO are increased. While the ISO was greatly reduced by the wave filter in the last case, when ice is introduced, the thrust ISO is greatly increased. This is also considering that the applied thrust was reduced before the disturbing ice forces. The post-controller performance was generally poorer in ISE and maximal offset, while slightly better in ISO. It can be noticed in Figure 6.3.1 that the better ISO performance for the post-controller placement is due to a more filtered thrust. It is best seen in yaw, where the magnitude is lower, although it lags behind the pre-controller placement. As mentioned earlier, this is due to double filtering of the feedback.

	x ISE	y ISE	ψ ISE	max pos error	τ_x ISO	τ_y ISO	τ_N ISO
pre-controller	1.40	1.40	1.67	1.13	1.55	1.50	2.67
post-controller	1.67	1.60	1.73	1.20	1.44	1.36	1.86

Table 6.3.1: Ratio between ISE with and without wave filtering for position and heading, maximal position error and ratio between ISO with and without wave filtering for high-pass filtered applied forces and moments. Ice-disturbance gain $\begin{bmatrix} 4e4 & 4e4 & 4e6 \end{bmatrix}^T$ and offset $\begin{bmatrix} -2e5 & 3.5e5 & 5e6 \end{bmatrix}^T$.

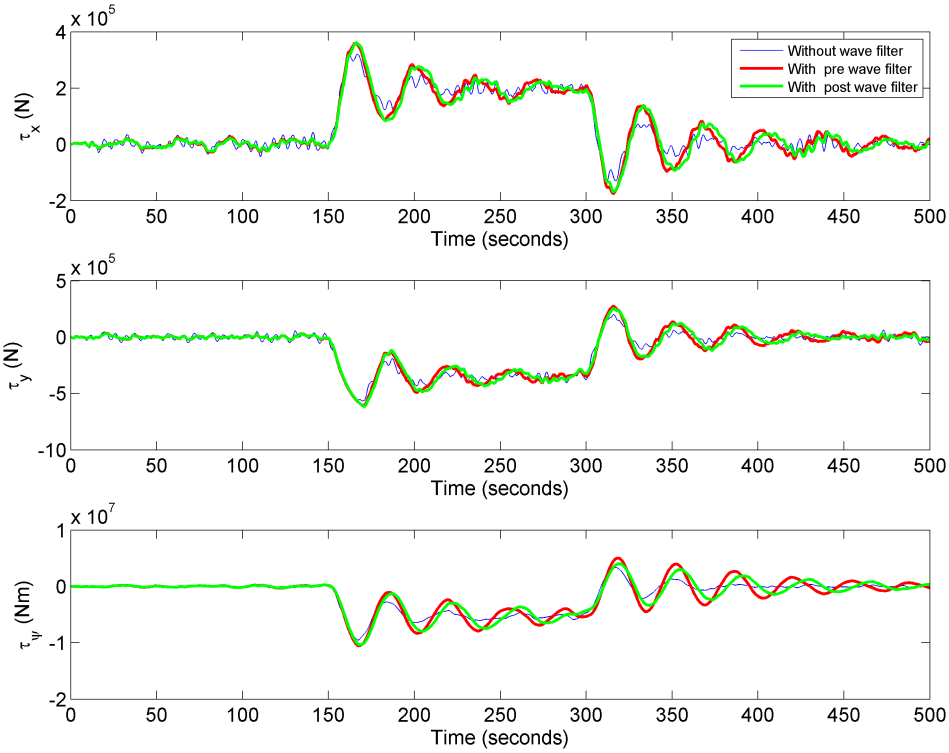

Figure 6.3.1: Plot of applied thruster force without and with wave filtering. Ice-disturbance gain $\begin{bmatrix} 4e4 & 4e4 & 4e6 \end{bmatrix}^T$ and offset $\begin{bmatrix} -2e5 & 3.5e5 & 5e6 \end{bmatrix}^T$.

One possible solution is to introduce a selective wave filter, which can be turned off when a sudden unknown external disturbance occurs. A selective wave filter algorithm is proposed as follows:

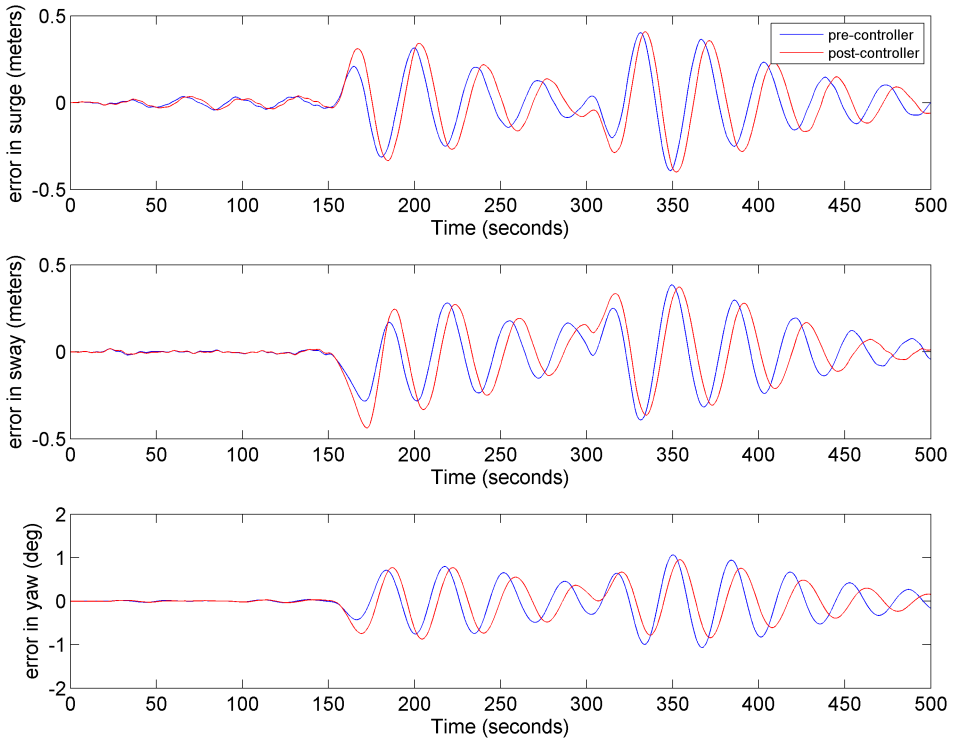

Figure 6.3.2: Plot of the difference between unfiltered and wave filtered posture. Ice-disturbance gain $\begin{bmatrix} 4e4 & 4e4 & 4e6 \end{bmatrix}^T$ and offset $\begin{bmatrix} -2e5 & 3.5e5 & 5e6 \end{bmatrix}^T$.

Algorithm 6.2 Selective Wave Filter Algorithm for switching between unfiltered and wave filtered signals to handle sudden unknown external disturbances

1. Differentiate the acceleration estimate to calculate the jerk
2. Let the filter be off until the frequency tracker has initialized, i.e. after a predefined time t_{init}, then turn on
3. If the jerk exceeds the predefined limits, mark the time as $t_{disturbance}$ and turn filter off
4. Keep filter off until the time equals the time of the last disturbance plus a predefined settle time, i.e. $t = t_{disturbance} + t_{settle}$, then turn on

6.3.1 Explanation of Algorithm 6.2

The first step in the algorithm is to calculate the jerk $\ddot{\boldsymbol{\nu}}$ of the vessel by differentiating the acceleration estimate. The reason for this is to be able to determine when an unknown external disturbance acts on the vessel. As the wave forces are oscillatory, the acceleration estimate will also contain oscillations. When a disturbance occurs, the force will influence the acceleration of the vessel, but not necessarily by a factor that is larger than the wave oscillations. Had the notch filter been perfect, the change in acceleration caused by the disturbance could be recognized from the filtered signal. However, by calculating the jerk, the sudden change in acceleration will distinguish itself as a spike in the jerk, as opposed to the oscillating jerk forces.

The second step is to let the frequency tracker initialize and converge to a frequency estimate before the wave filter is turned on.

The third step is to identify a sudden unknown disturbance. The time of occurrence is marked as $t_{disturbance}$ and the filter is turned off. The predefined jerk limits are calculated by measuring the maximal impact the waves have on the jerk, such that spikes caused by ice disturbances will be detectable. The predefined jerk limits in this implementation were found as ± 0.8 m/s^3 for surge and sway, where the significant wave height was chosen to represent sea state 7 (high), i.e. $H_s = 7.8$ meters, such that rough sea will not turn off the filter.

The fourth step keeps the filter off until a predefined settle time t_{settle} has passed after the last measured disturbance. This is to keep the filter from turning on and off again during the disturbance, and unless the vessel settles while the disturbance is ongoing, i.e. in the case of a constant ongoing disturbance, waits until the vessel settles after the disturbance before turning the filter back on.

Figure 6.3.3 illustrates how the algorithm turns the filter on after $t = t_{init}$, turns it off at $t = 500$ when the ice disturbance occurs, and turns it back on again t_{settle} seconds after the last disturbance that surpassed the jerk limit at $t = 900$.

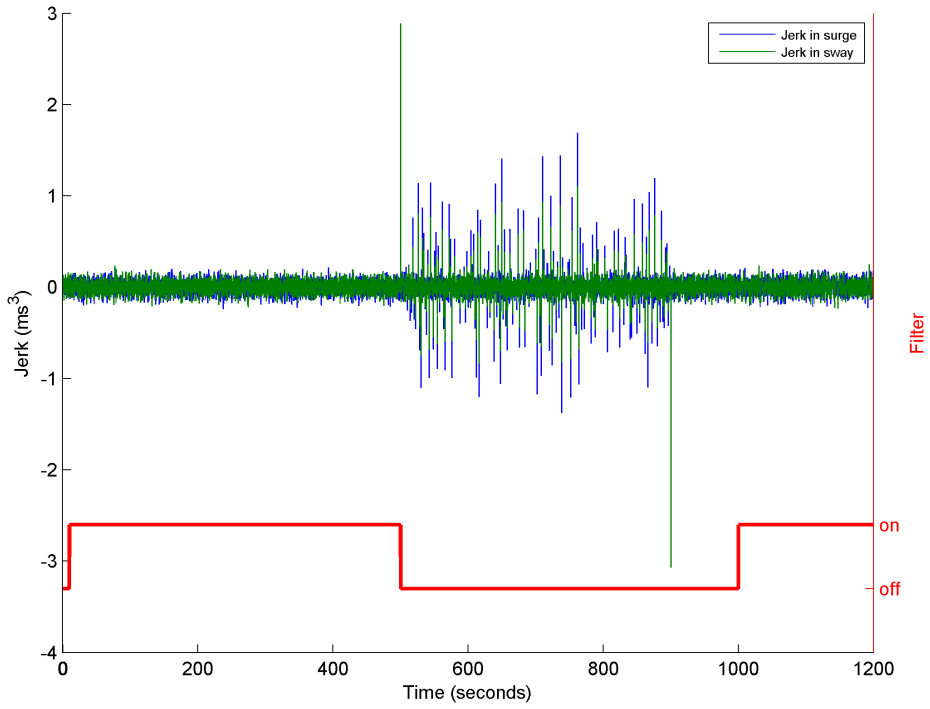

Figure 6.3.3: Plot to illustrate the jerk in surge and sway when influenced by ice-inspired forces, and the result of the selective wave filter algorithm. Here $t_{init} = 10$ and $t_{settle} = 100$.

6.3.2 Effect of Selective Wave Filter

As seen in Figure 6.3.4, the selective wave filter only reduces the applied thrust in the calm range before and after the disturbance, while the highly responsive thrust needed to handle the disturbance is intact. Figure 6.3.5 shows that the magnitude of the difference in posture is reduced significantly with the selective wave filter. The small deflections are due to the switch between the unfiltered and filtered signals, as the switch causes a phase shift in the feedback signal, as well as phase lag influencing the wave-induced control response. Table 6.3.2 shows that the applied thrust is reduced for surge and sway, while the posture and yaw moment are more or less unaffected for both placements of the filter. This illustrates the advantage of the selective filter, when compared to the non-selective.

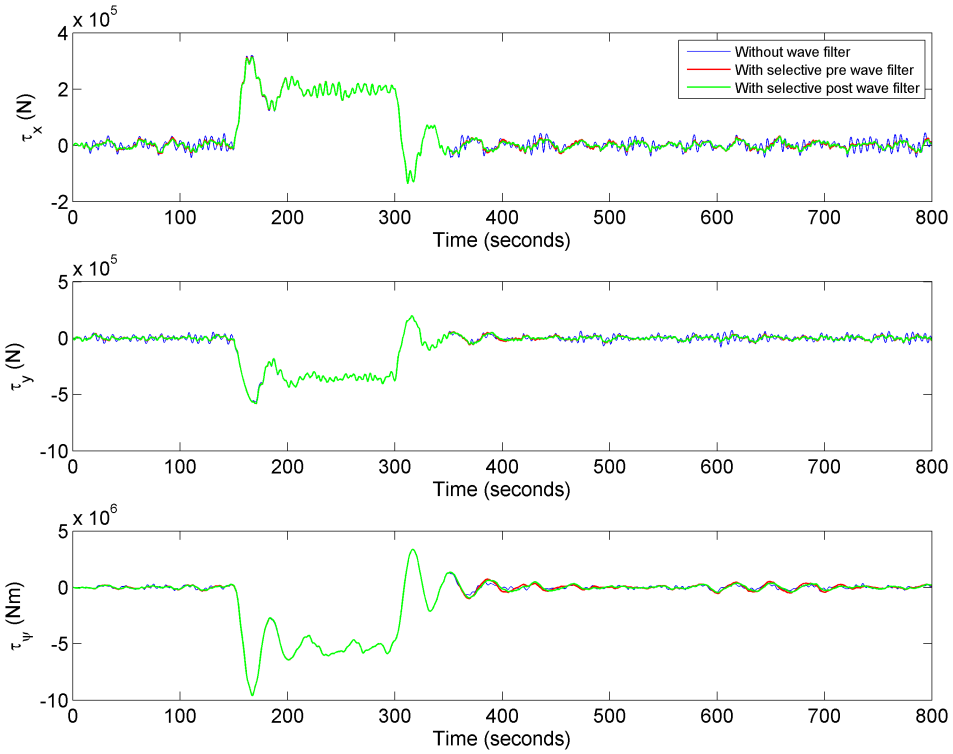

Figure 6.3.4: Plot of applied thruster force without and with selective wave filtering. Ice-disturbance gain $\begin{bmatrix} 4e4 & 4e4 & 4e6 \end{bmatrix}^T$ and offset $\begin{bmatrix} -2e5 & 3.5e5 & 5e6 \end{bmatrix}^T$.

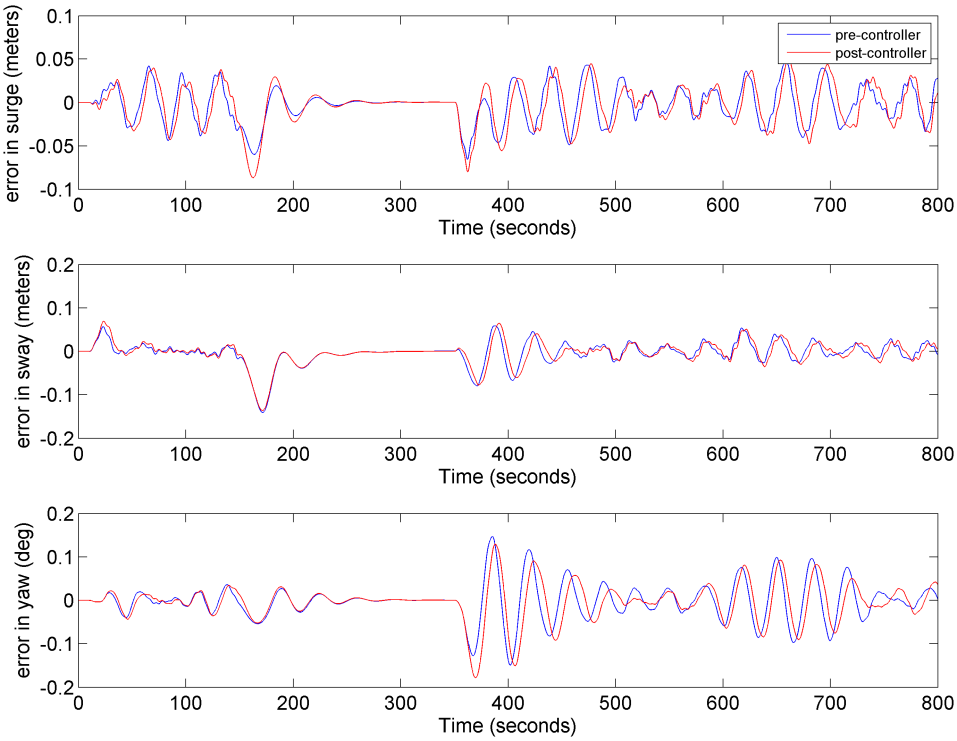

Figure 6.3.5: Plot of the difference between unfiltered and selective wave filtered posture. Ice-disturbance gain $\begin{bmatrix} 4e4 & 4e4 & 4e6 \end{bmatrix}^T$ and offset $\begin{bmatrix} -2e5 & 3.5e5 & 5e6 \end{bmatrix}^T$.

	x ISE	y ISE	ψ ISE	max pos error	τ_x ISO	τ_y ISO	τ_N ISO
pre-controller	0.99	1.10	1.03	1.03	0.77	0.80	1.03
post-controller	0.97	1.10	1.02	1.03	0.74	0.79	1.02

Table 6.3.2: Ratio between ISE with and without selective wave filtering for position and heading, maximal position error and ratio between ISO with and without selective wave filtering for high-pass filtered applied forces and moments. Ice-disturbance gain $\begin{bmatrix} 4e4 & 4e4 & 4e6 \end{bmatrix}^T$ and offset $\begin{bmatrix} -2e5 & 3.5e5 & 5e6 \end{bmatrix}^T$.

To demonstrate when the selectiveness becomes crucial, a more extreme scenario is considered. If the disturbance becomes too aggressive, the phase lag in the wave filter may cause instability. By letting the ice-disturbance gain be raised to

$\begin{bmatrix} 5e5 & 5e5 & 5e7 \end{bmatrix}^T$ and offset $\begin{bmatrix} -5e5 & 3e5 & 8e6 \end{bmatrix}^T$, then as seen in Figures 6.3.6 and 6.3.7, the wave filters make the system unstable as they cannot follow the aggressive disturbance. The selective wave filters, however, have no problems with these ice-forces and as seen in Table 6.3.3, they again reduce the applied thrust while hardly affecting the posture. Both filter placements yield very similar results.

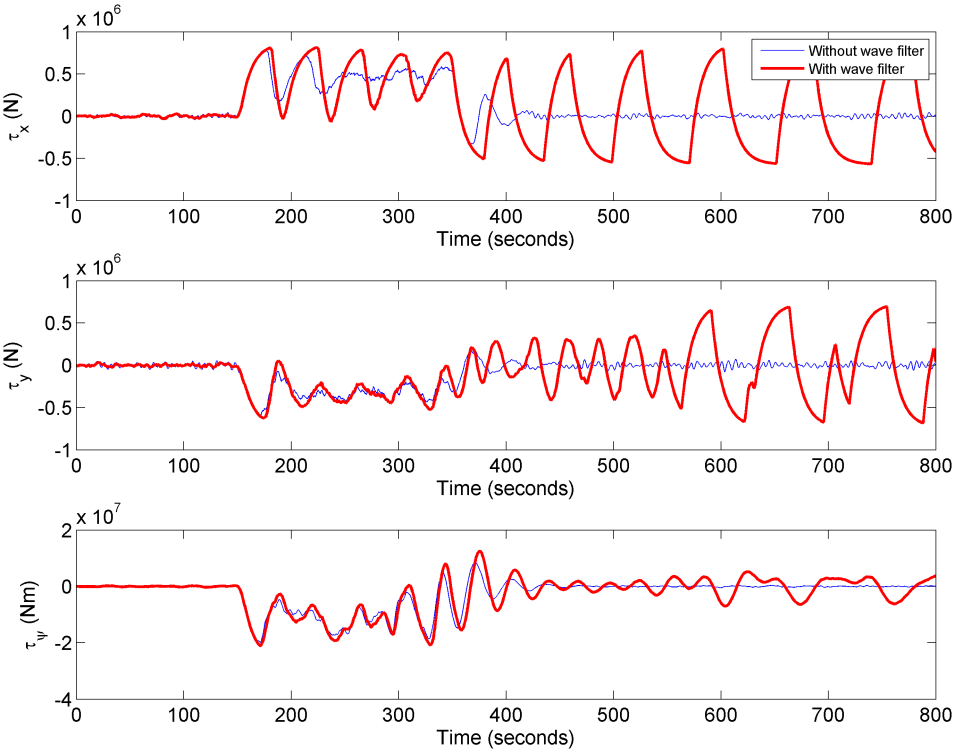

Figure 6.3.6: Plot of applied thruster force without and with selective wave filtering. Ice-disturbance gain $\begin{bmatrix} 5e5 & 5e5 & 5e7 \end{bmatrix}^T$ and offset $\begin{bmatrix} -5e5 & 3e5 & 8e6 \end{bmatrix}^T$.

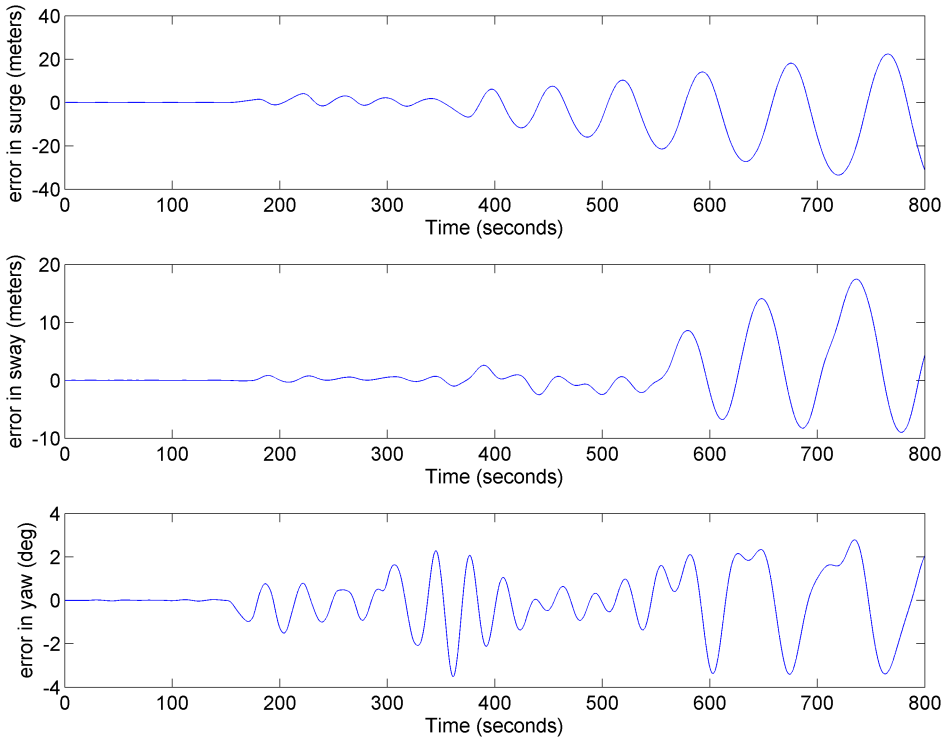

Figure 6.3.7: Plot of the difference between unfiltered and selective wave filtered posture. Ice-disturbance gain $\begin{bmatrix} 5e5 & 5e5 & 5e7 \end{bmatrix}^T$ and offset $\begin{bmatrix} -5e5 & 3e5 & 8e6 \end{bmatrix}^T$.

	x ISE	y ISE	ψ ISE	max pos error	τ_x ISO	τ_y ISO	τ_N ISO
pre-controller	0.97	1.07	1.02	0.99	0.95	0.85	1.02
post-controller	0.95	1.07	1.02	0.98	0.94	0.84	1.01

Table 6.3.3: Ratio between ISE with and without wave filtering for position and heading, maximal position error and ratio between ISO with and without wave filtering for high-pass filtered applied forces and moments. Ice-disturbance gain $\begin{bmatrix} 5e5 & 5e5 & 5e7 \end{bmatrix}^T$ and offset $\begin{bmatrix} -5e5 & 3e5 & 8e6 \end{bmatrix}^T$.

Chapter 7

Case Study

7.1 Simulink Simulations

To test the performance of the proposed measures against sudden unknown external disturbances, a vessel was modeled in Simulink and tested in different scenarios. The simulated vessel was chosen as a supply vessel created by the MSS toolbox [32]. A more detailed description of the vessel model can be found in Appendix B.

To explore how the vessel handles sudden unknown external disturbances, the following scenarios were considered:

- Sideways constant disturbance, Section 7.1.2.
- Head-on constant disturbance, Section 7.1.3.
- Varying ice disturbance, Section 7.1.4.
- Varying ice disturbance with selective wave filter, Section 7.1.5.
- Constant disturbance with predictive action and selective wave filter, Section 7.1.6.

The purpose of first two cases was to test the performance and robustness of the vessel when subjected to different sudden and unknown, but constant external forces. The purpose of the third and fourth case was to explore how the different control strategies were affected by varying ice disturbances, with and without selective wave filtering. The last case explores the effect on robustness and performance when all proposed measures against external disturbances are applied at once.

7.1.1 Case Outline

The first three cases were tested with the PID controller in combination with the Disturbance Rejection by Acceleration Feedforward controller (AFF), the PID with cubic stiffness (PIDP^3), the PID with cubic stiffness and damping (PIDP^{3}D^3), and with the PID controller alone for comparison. The last two cases were tested

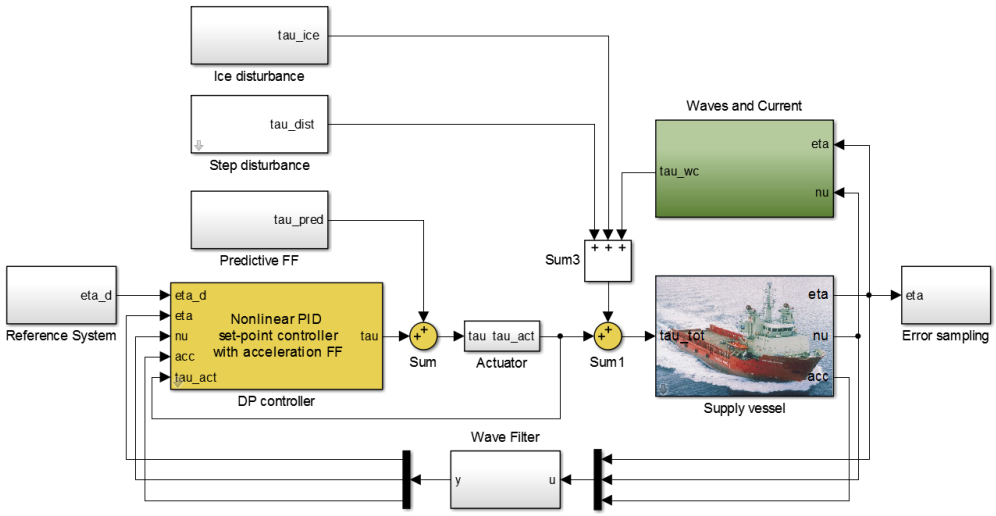

Figure 7.1.1: Simulink model.

with the AFF and the AFF with model errors against the PID controller. The PID controller was tuned as proposed in Section 4.1.4, with the exceptions that $\boldsymbol{K}_d = 2\zeta\omega_n\boldsymbol{M} - \boldsymbol{D}$ was tuned as $\boldsymbol{K}_d = 2\zeta\omega_n\boldsymbol{M}$ as it yielded better performances, and that the integral gain was reduced to $\boldsymbol{K}_i = \frac{0.03^3}{10}\boldsymbol{M}$ for the AFF controller, as further explained in Section 4.2.1. The integral gain for the PID controller was chosen according to the methods in Section 4.1.4. The cubic terms were chosen as $\boldsymbol{K}_{p3} = .2\boldsymbol{K}_p$ and $\boldsymbol{K}_{d3} = 5\boldsymbol{K}_d$ after some testing. The controller bandwidth was chosen such that $\omega_n = 0.1$ rad/s and the relative damping ratio to $\zeta = 1.5$. The AFF controller was implemented as in (4.2) with a measurement delay $\delta = 0.1$ seconds. As the IMU sensor only provides linear accelerations, the control force from the AFF became

$$\boldsymbol{\tau}_{FF} = \begin{bmatrix} M_{11}\hat{a}_x + D_{11}\hat{\nu}_x - \tau_x \\ M_{22}\hat{a}_y + D_{22}\hat{\nu}_y + D_{23}\hat{\nu}_\psi - \tau_y \\ D_{32}\hat{\nu}_y + D_{33}\hat{\nu}_\psi - \tau_\psi \end{bmatrix} \tag{7.1}$$

where the parameters for $\boldsymbol{M}$ and $\boldsymbol{D}$ are given in Appendix B.

The reference model in Figure 7.1.1 was chosen as a simple first order low-pass filter, to create a smooth trajectory to eventual changing setpoints. As seen in Figure 7.1.1, the wave filter was placed before the controller, after reflecting on the results in Chapter 6.

The constant disturbance was modeled as a step, representing a sudden but constant ongoing or slowly varying disturbance. The varying ice disturbance was created in an attempt to resemble the ice disturbance presented in [26], which is a version of the findings in [14], scaled to fit the same vessel model used in this

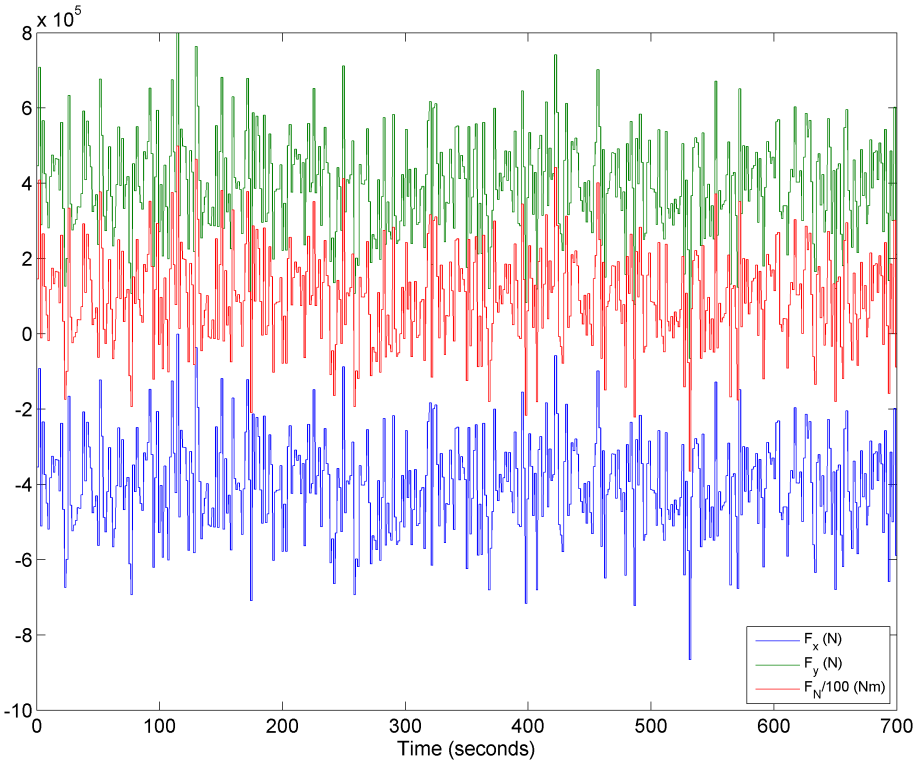

Figure 7.1.2: Ice disturbance with gain $\begin{bmatrix} 5e5 & 5e5 & 5e7 \end{bmatrix}^T$ and offset $\begin{bmatrix} -4e5 & 4e5 & 1e7 \end{bmatrix}^T$.

thesis. As this time-series was not available, white noise subjected to a gain and an offset were used to mimic the behavior of the disturbance in [26]. An example of the ice disturbance can be seen in Figure 7.1.2.

In each simulation, the vessel was initialized in $\boldsymbol{\eta} = \begin{bmatrix} 0 & 0 & 0 \end{bmatrix}^T$, and subjected to a disturbance after some time. A JONSWAP wave distribution with $\omega_0 = 1.1$ rad/s in each DOF, and significant wave height $H_s = 2.4$ meters was applied in every case. No other external disturbances such as current or wind were turned on, as they can be viewed as constant disturbances that will be handled by integral action or wind-feedforward. $\boldsymbol{\eta}_d = 0$ was chosen in every case to focus on stationkeeping. The duration of the simulation was set to 700 seconds for each case.

7.1.2 Case 1: Sideways Constant Disturbance

The vessel was subjected to an external force with magnitude $F_I = 4e5$, point of impact $\boldsymbol{p}^b_{I,CG} = \begin{bmatrix} 40 & 9 \end{bmatrix}^T$ and angle of impact $\theta_{AoI} = 80$ degrees at time $t = 200$. This represents a disturbance impacting on the right corner of the bow.

The function *pred_force.m* from Section 5.4 was used to calculate the force vector, which became $\boldsymbol{\tau}_{disturbance} = \begin{bmatrix} \text{-6.9e4} & \text{-3.9e5} & \text{-1.5e7} \end{bmatrix}^T$ (N, N, Nm).

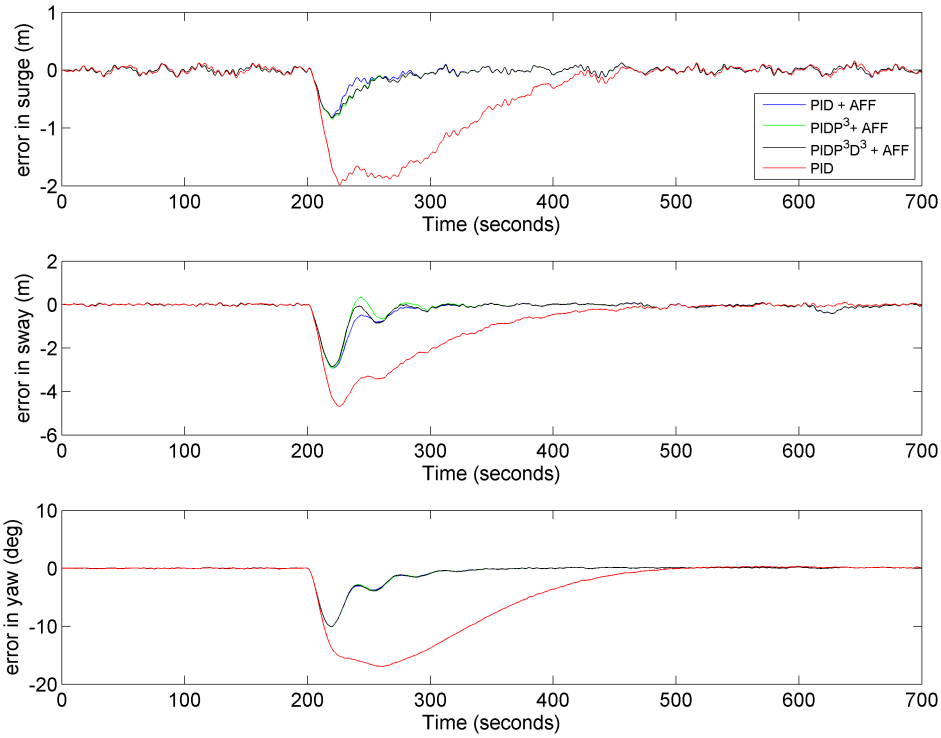

Figure 7.1.3: Case 1, position and heading deviations for four different control strategies.

As illustrated in Figure 7.1.3, all three proposed control approaches yield better results than the PID alone. It can be noticed in sway that the cubic controllers are a little more aggressive and thus oscillate a little more than the AFF alone, which may indicate a too aggressive tuning. Compared to the PID controller, the maximal error in surge is reduced by approximately 1.5 meters in surge, 2 meters in sway and 7 degrees in yaw. In addition, the PID controlled posture converges significantly slower in all DOFs.

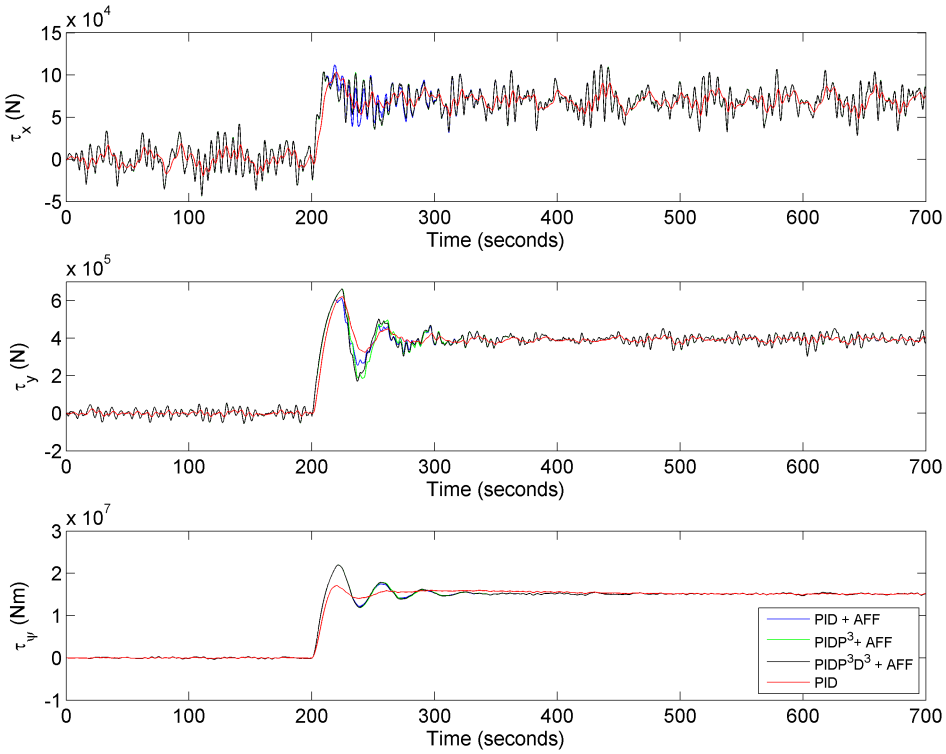

Figure 7.1.4: Case 1, thruster feedback for four different control strategies.

Figure 7.1.4 shows the corresponding thruster feedback, where it can be seen that the AFF strategies applies thrust more rapidly than the PID controller, which reflects the theory on disturbance rejection, i.e. in contrast to the PID, it does not wait for the error build up to produce control force. The oscillatory behavior in yaw may suggest that the PID controller could have been tuned softer when used in combination with the AFF controller. The wave influenced control force is best seen in surge due to the scaling of the magnitude in each plot, where it can be noticed that the AFF strategies are much more influenced by wave forces. This is due to the acceleration feedback, which amplifies the wave forces from the first-order wave loads. This behavior suggests the need for a wave-filter.

7.1.3 Case 2: Head-on Constant Disturbance

The vessel was subjected to an external force with magnitude F_I = 6e5, point of impact $\boldsymbol{p}^b_{I,CG} = \begin{bmatrix} 40 & 4 \end{bmatrix}^T$ and angle of impact $\theta_{AoI} = 10$ degrees at time $t = 200$. This represents a disturbance impacting on the right corner of the bow. The function *pred_force.m* from Section 5.4 was used to calculate the force vector, which became $\boldsymbol{\tau}_{disturbance} = \begin{bmatrix} \text{-5.9e5} & \text{-1.0e5} & \text{-1.8e6} \end{bmatrix}^T$ (N, N, Nm).

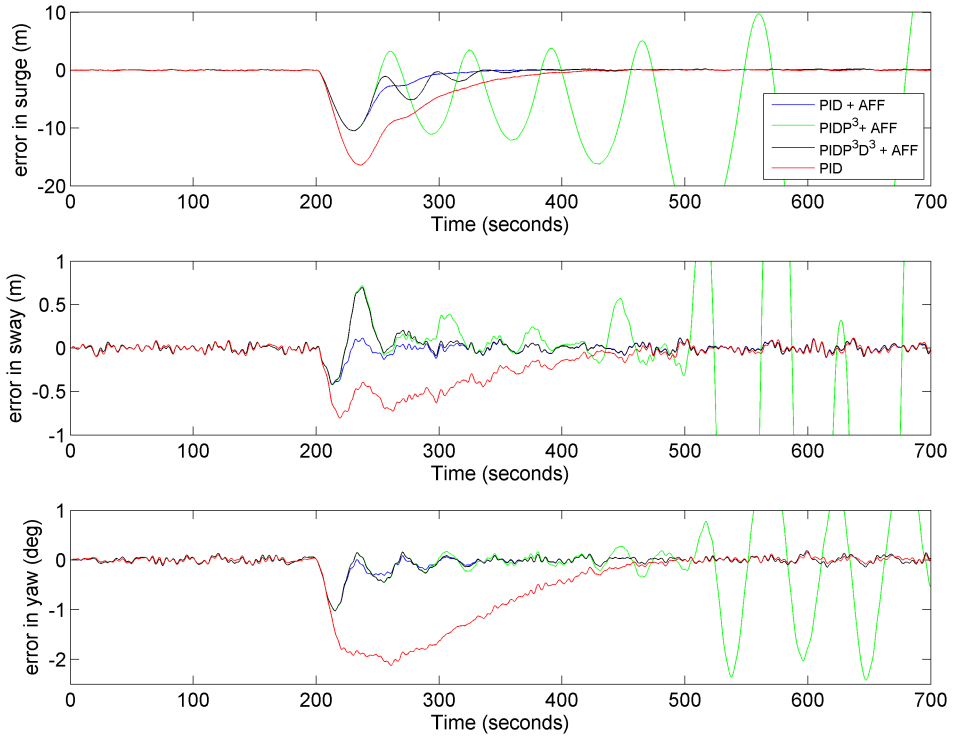

Figure 7.1.5: Case 2, position and heading deviations for four different control strategies.

As seen in Figure 7.1.5, the AFF and AFF with both cubic stiffness and damping perform better than the PID controller, while the cubic stiffness controller becomes unstable due to too large errors in surge. The cubic stiffness and damping + AFF controller has some more oscillating motions in surge and slightly larger offset in sway, compared to the AFF controller alone, which thus has the best performance. Compared to the PID controller, the AFF reduced the heading offset with about 1 degree, while the offset in surge is reduced from approximately 16 meters to 10 meters. The sway is as expected not very affected by the head-on disturbance, but the AFF still performs best. Again, the AFF converges a lot faster than the PID.

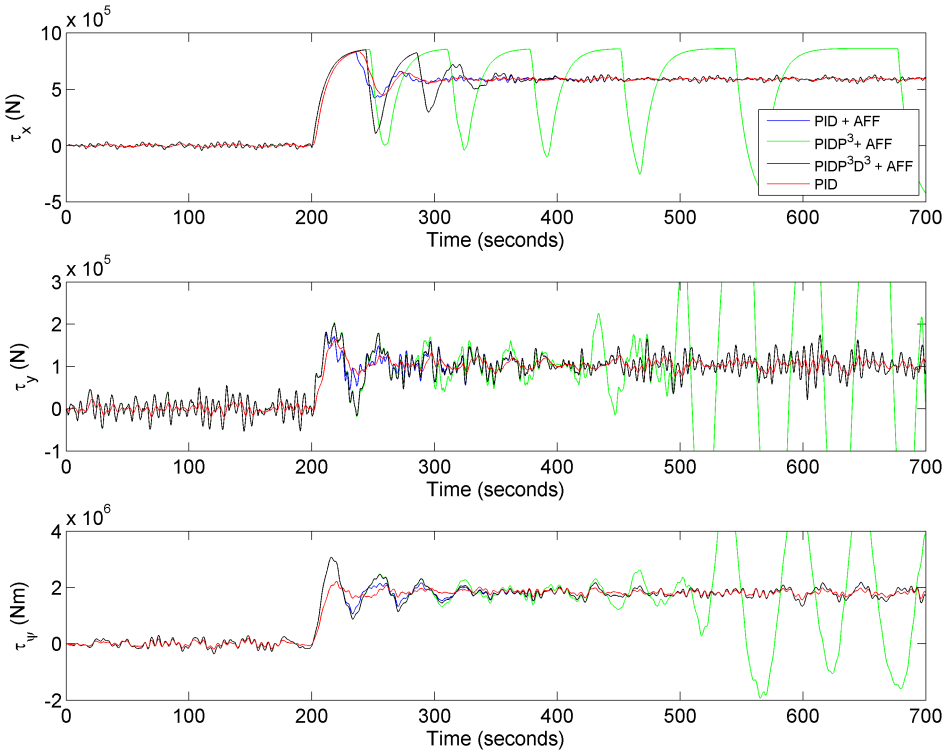

Figure 7.1.6: Case 2, thruster feedback for four different control strategies.

Figure 7.1.6 again demonstrates that the cubic stiffness controller becomes unstable as it hits the thruster limits. The AFF strategies are more aggressive in yaw, while the AFF controller in surge is very similar to the PID, though it applies thrust more rapidly and converge faster to the value of the disturbance.

7.1.4 Case 3: Varying Ice Disturbance

The vessel was subjected to a varying ice-inspired external force with gain $\begin{bmatrix} 2e5 & 2e5 & 4e7 \end{bmatrix}^T$ and offset $\begin{bmatrix} -3e5 & 4e5 & 1e7 \end{bmatrix}^T$. The disturbance impacts at $t = 200$ and discharges at $t = 400$. This represents a disturbance impacting on the left side of the vessel.

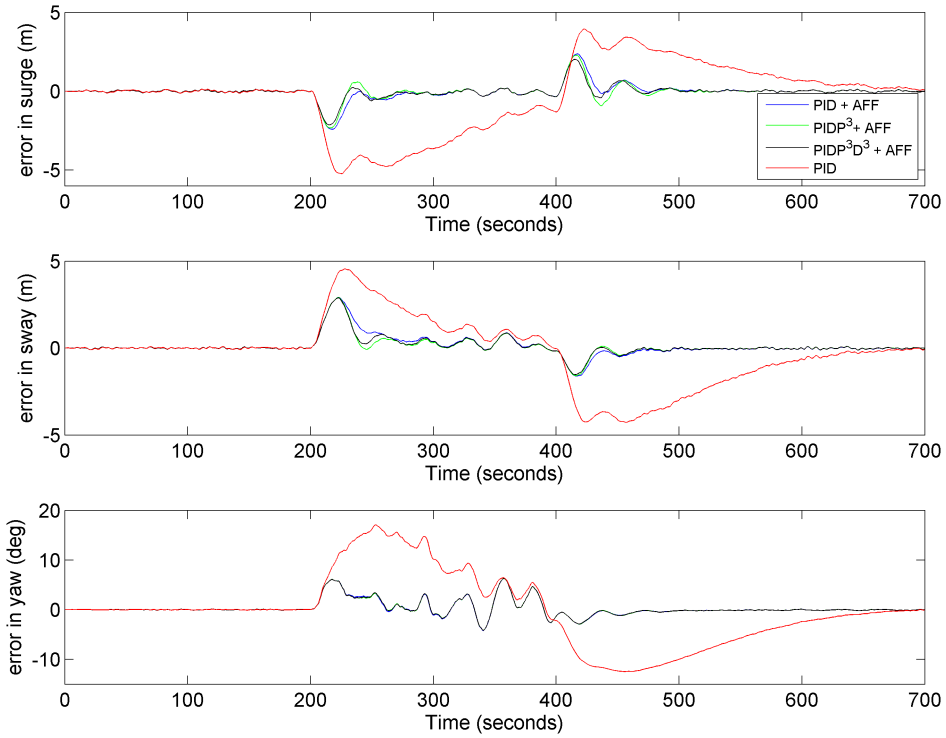

Figure 7.1.7: Case 3, position and heading deviations for four different control strategies.

As illustrated in Figure 7.1.7, the AFF strategies greatly improve the performance compared to the PID controller in all DOFs. Although the cubic controllers converge slightly quicker after the incoming disturbance, the AFF controller yields the overall best performance. The PID controller cannot keep up with the varying disturbance and does not converge before the ice discharges, and thus experiences a large offset yet again. The initial offset was reduced with about 3 meters in surge, 2 meters in sway and 10 degrees in yaw, when comparing the AFF with the PID controller.

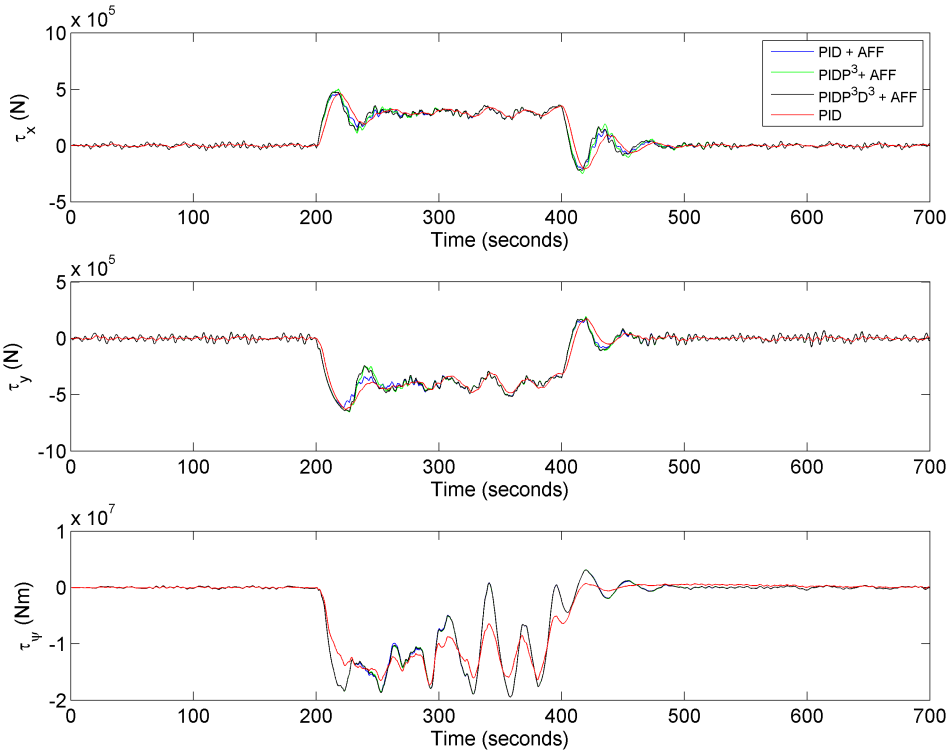

Figure 7.1.8: Case 3, thruster feedback for four different control strategies.

The corresponding thruster feedback can be seen in Figure 7.1.8. All control strategies have very similar performance in surge and sway, while the AFF strategies have higher amplitudes in yaw. This illustrates the lack of angular acceleration feedback, which as seen in Figure 7.1.7, results in heading errors of up to approximately 6 degrees.

7.1.5 Case 4: Varying Ice Disturbance with Selective Wave Filter

The vessel was subjected to the same varying ice-inspired disturbance as in the last case, but with selective wave filtering turned on. As reflected in the discussion in Chapter 8, the AFF controller yields the best results, resulting in the rejection of the cubic controllers. Instead, an AFF controller with model errors have been introduced to illustrate its robustness. As the weight of a real vessel will vary with loading conditions, the actual mass and damping matrices will be uncertain [26]. The AFF with model errors was implemented with the adjusted parameters $\bar{\boldsymbol{M}} = 0.75\boldsymbol{M}$ and $\bar{\boldsymbol{D}} = 0.9\boldsymbol{D}$.

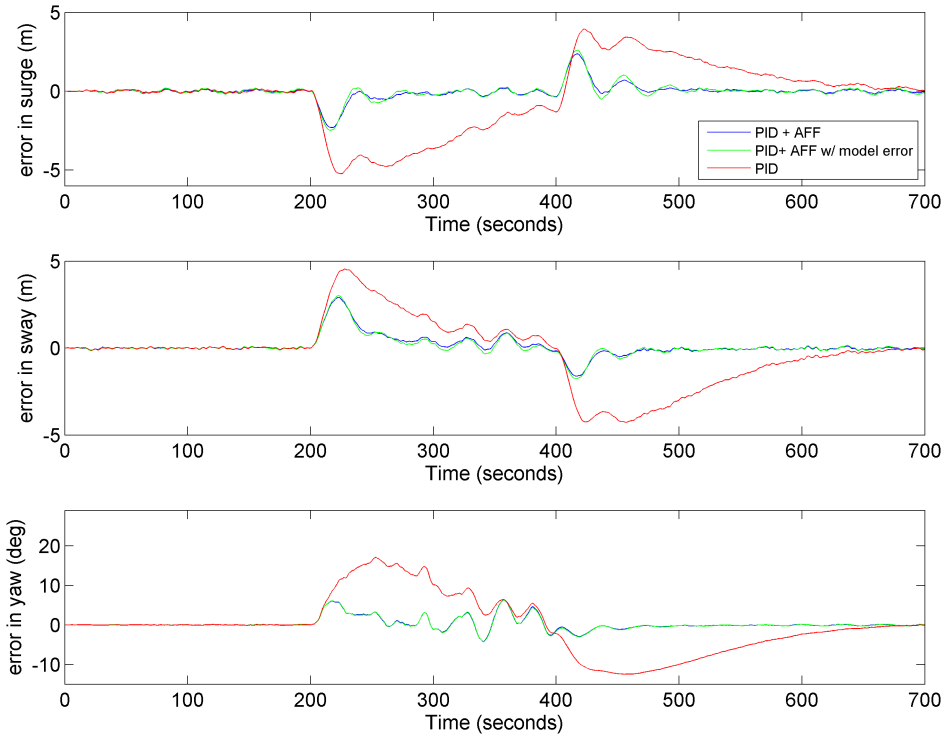

Figure 7.1.9: Case 4, position and heading deviations for four different control strategies.

As seen in Figure 7.1.9, the uncertain AFF performs almost as well as the certain AFF, with the exceptions of some slightly higher amplitude on the deflections at the occurrence of the impacting and discharging disturbance. Otherwise, it is observed that the selective wave filter does not affect the position and heading noticeably.

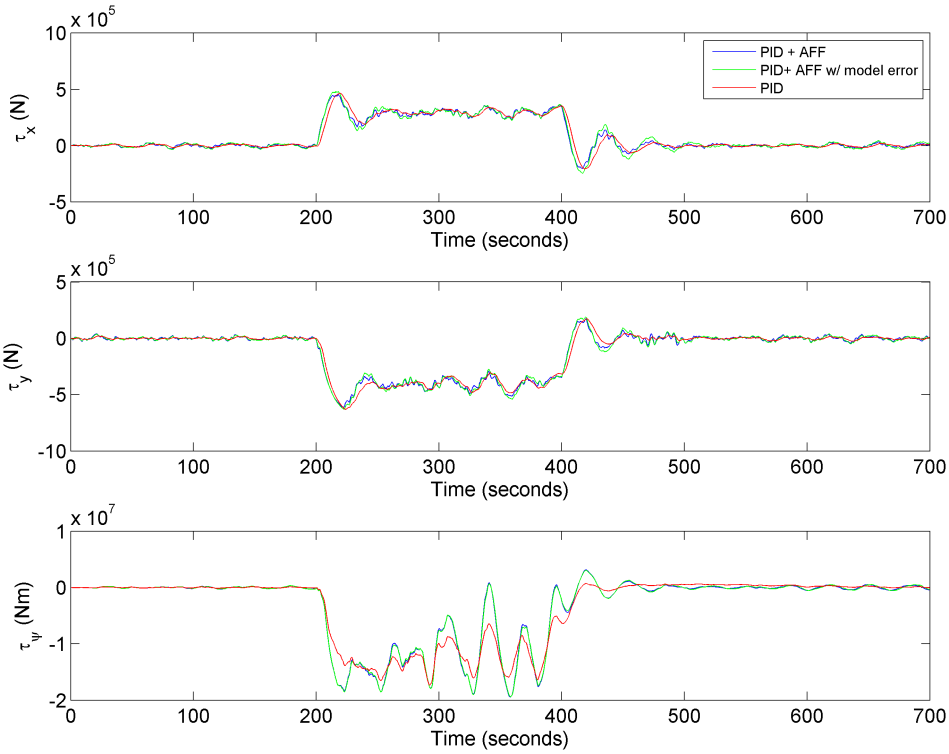

Figure 7.1.10: Case 4, thruster feedback for four different control strategies.

Figure 7.1.10 shows the corresponding thrust, which is very similar to the last case. A slightly more aggressive thrust can be observed for the uncertain AFF, where the amplitudes in surge and sway are a little higher than the AFF at the times right after the disturbance impacts and discharges. This explains the higher deflections in position as mentioned above. The effect of the selective wave filter can be seen in all DOFs, where in comparison with Figure 7.1.8 from the last case, the thrust is much calmer before and after the disturbance. Upon close observation, it can be seen that the wave filter is turned back on at approximately $t = 500$, which represents a time $t_{settle} = 100$ seconds after the last detected disturbance. The visual effect of the selective wave filter disappears in yaw due to the large magnitude of thruster feedback. The problem with the wave influence on the AFF controller mentioned in Section 7.1.2, has been attenuated when the selective wave filter is turned on.

7.1.6 Case 5: Constant Disturbance with Predictive Action and Selective Wave Filter

The vessel was subjected to the same disturbance as in Case 1, i.e. an external force with magnitude $F_I = 4e5$, point of impact $\boldsymbol{p}^b_{I,CG} = \begin{bmatrix} 40 & 9 \end{bmatrix}^T$ and angle of

impact $\theta_{AoI} = 80$ degrees at time $t = 200$. In addition, the selective wave filter is turned on, and a predictive force with $F_p = 2.25F_I$ was applied $t_p = 2.5$ seconds before the disturbance, according to the results found in Chapter 5. The predictive angle and displacement vector were the same as with the disturbance.

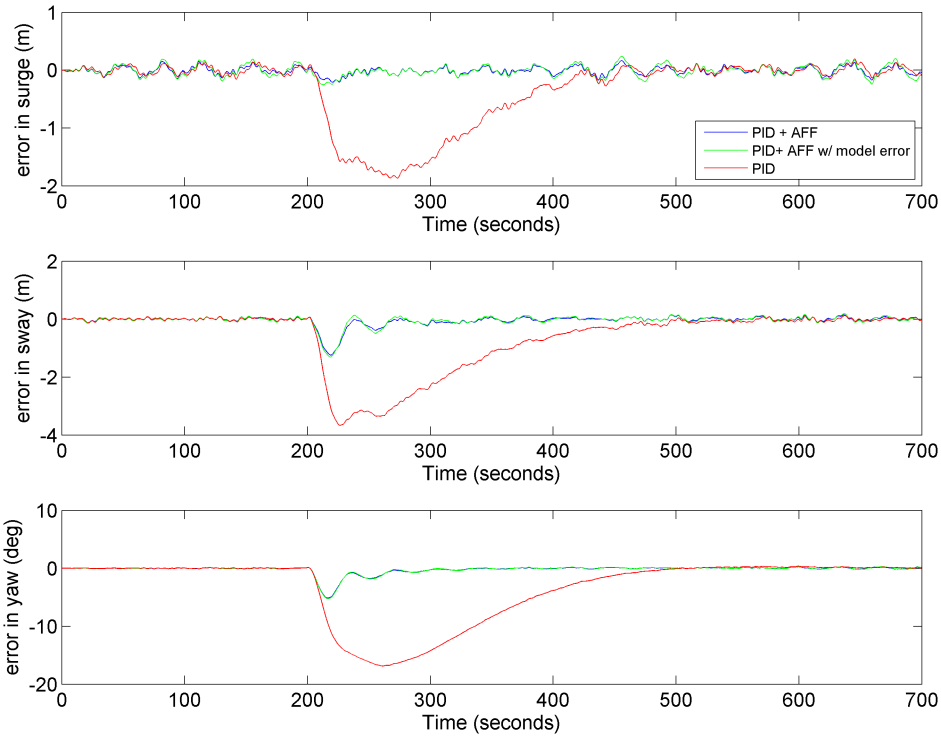

Figure 7.1.11: Case 5, position and heading deviations for four different control strategies.

As can be seen in Figure 7.1.11, the PID controller benefits very little from the proactive action, except from about a meter less offset in sway, compared to Figure 7.1.3 from Case 1. The AFF controllers, however, perform very well as especially seen in surge, where the disturbance is completely canceled out. In sway, the offset is reduced from about 2.5 meters in Case 1, to approximately 1 meter, and the heading deflection is reduced from about 10 degrees in Case 1, to about 5 degrees. This demonstrates the benefits of combining all the measures against sudden unknown external disturbances proposed in this thesis. Although, it should be mentioned that a more accurately based predictive force would yield even better cancellation of the disturbance, but it is limited by the previously discussed accuracy of the ice observation system (see Section 5.4.1).

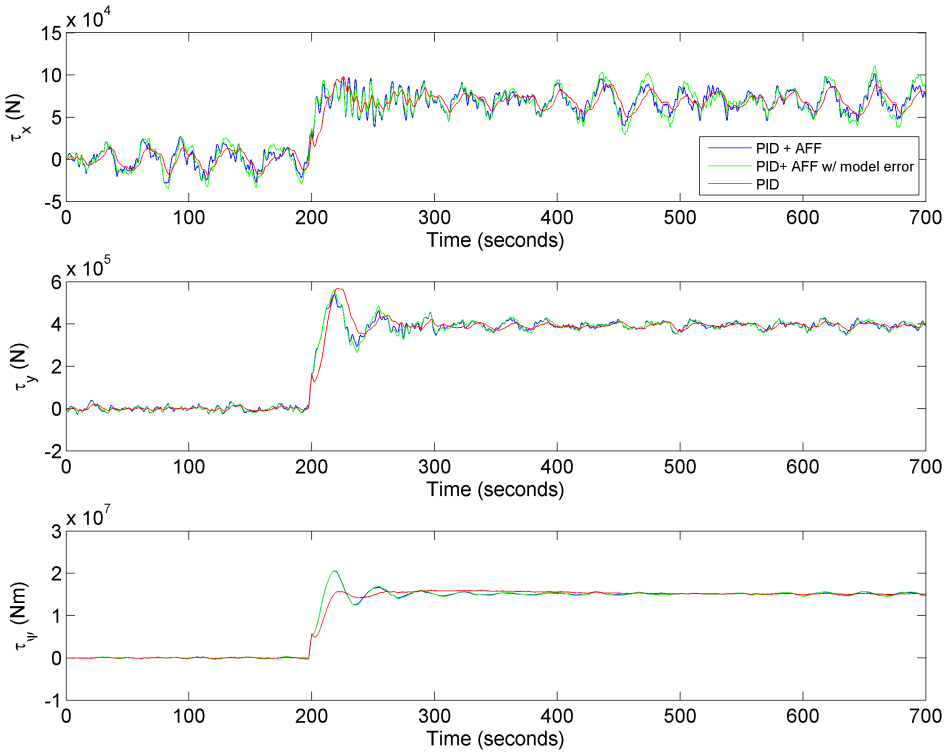

Figure 7.1.12: Case 5, thruster feedback for four different control strategies.

The corresponding thrust is shown in Figure 7.1.12, which is depicted as very similar to the applied thrust in Case 1. The wave filter has attenuated the wave forces to some degree, which have become less oscillating for all three controllers. The effect of the proactive action can be noticed as a small dip in thrust for the PID controller in all DOFs, whereas the AFF controllers continues to apply thrust to handle the disturbance.

7.1.7 ISE

To compare the actual magnitude of the controller errors and the use of thrust, a measurement called Integral Squared Error (ISE) was logged from the simulations. The ISE can be expressed as

$$ISE = \int_0^t e^2(\kappa) d\kappa \tag{7.2}$$

where $e(t)$ is the error between the desired and the actual controlled variable, κ is the integration variable and t is the time span of the simulation. To measure the use of thrust, the same method was used by substituting $e(t)$ with $\tau(t)$. The measurement of the squared thrust has been labeled as the Integral Squared Output (ISO) in this thesis.

ISE is a measurement that will penalize large errors more than small errors, due to the square [44]. This implies that the errors in Table 7.1.1 are dominated by the larger errors, and does not necessarily reflect how good the controllers perform during steadier states.

	x ISE	y ISE	ψ ISE	τ_x ISO	τ_y ISO	τ_N ISO
Case 1:						
AFF	0.03932	0.1466	0.0749	4.925	1.900	1.924
AFF+CS	0.05110	0.1270	0.0746	4.901	2.284	1.984
AFF+CS+CD	0.0490	0.1259	0.07461	4.918	2.330	1.987
Case 2:						
AFF	0.2866	0.03793	0.02945	1.234	6.313	3.107
AFF+CS	1.094	0.1411	0.02825	9.917	6.434	3.156
AFF+CS+CD	0.3024	0.1348	0.02835	3.204	6.455	3.145
Case 3:						
AFF	0.05582	0.09928	0.04978	1.317	1.458	2.944
AFF+CS	0.04814	0.07967	0.04920	1.654	1.715	2.924
AFF+CS+CD	0.03794	0.08040	0.04947	1.576	1.750	2.937
Case 4:						
AFF	0.05353	0.09988	0.04957	1.192	1.228	2.948
AFF w/ error	0.06261	0.1001	0.05029	1.562	1.439	2.863
Case 5:						
AFF	0.01076	0.02449	0.01535	2.604	1.333	2.292
AFF w/ error	0.02051	0.02717	0.01597	2.932	1.496	2.362

Table 7.1.1: ISE and ISO ratios between different control strategies and PID controller.

7.1.7.1 ISE Comparison

Table 7.1.1 presents the ISE/ISO ratios between the proposedly improved controllers and the PID controller, such that a ratio below 1 represents an improvement and vice versa. The ISE in all DOFs was greatly reduced each case, except for the unstable AFF + cubic stiffness controller in Case 2, to only a couple percent of the PID ISE. The applied thrust however, was increased in every case compared to the PID controller. Notice that the thrust ISO is high-pass filtered before it is squared and integrated, such that only the thrust applied to counteract the disturbances was measured. This implies that a ratio of e.g. 4.925 does not mean that five times more thrust was applied, but rather that the squared area between the disturbance value and the applied thrust was five times higher. So rather than focusing on the magnitudes of the values in Table 7.1.1, the focus should be placed on the comparison between each control strategy in each case.

In Case 1, all controllers yield similar results, with the exception of better ISO

Figure 7.2.1: Control Computer (CC) provided by Marine Technologies.

in sway for the AFF controller. In Case 2, the AFF also have better ISE in sway and ISO in surge compared to the AFF + cubic stiffness and damping controller, while the cubic stiffness controller can be recalled to be unstable. For Case 3, the AFF has slightly better ISO performance in surge and sway, while the remaining measurements are similar. In Case 4 and 5, the AFF slightly outperforms the uncertain AFF controller in surge and sway ISO and surge ISE, while the other measurements are similar. One exception is the yaw ISO for the uncertain AFF controller in Case 4, which is slightly lower than the certain AFF controller.

7.2 MT Simulations

To execute Hardware-in-the-loop (HIL) testing of the performance of some of the proposed measures against sudden unknown disturbances, a case study was performed with a simulator provided by Marine Technologies (MT). The simulator consisted of a separate hardware Control Computer (CC) (see Figure 7.2.1) that was connected to a regular desktop computer via an Ethernet switch. An Operator Station (OS) ran the interface on the desktop computer (see Figure 7.2.2), while the actual simulations ran on the CC.

The simulated vessel was a basic vessel resembling a supply vessel, with a displacement of 5000 ton, a 6 meter draught and a length overall (LOA) of 85.2 meters. The thruster configuration consisted of one bow tunnel thruster, one bow azimuth thruster, one aft tunnel thruster and two main propellers with rudders in the port and starboard side of the stern. The thruster locations and capacities are described in Section B as they were used to limit the available thrust in the Simulink modeled vessel as well.

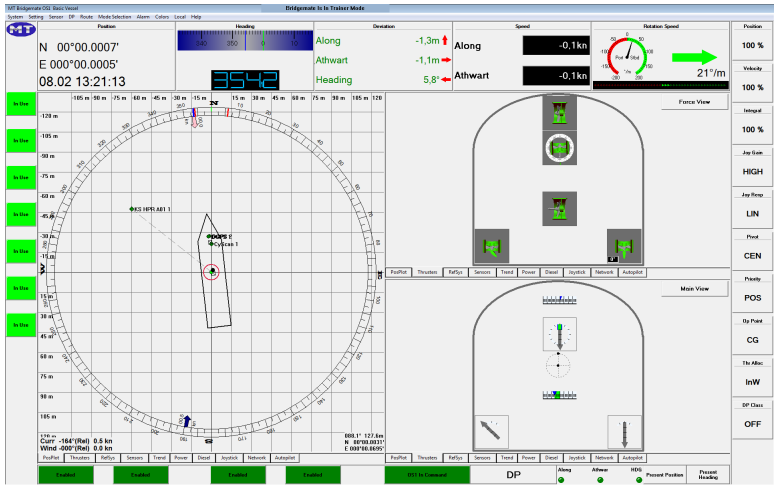

Figure 7.2.2: Operator Station (OS) interface provided by Marine Technologies.

Logging

The simulations were logged to a binary file, which was converted to comma-separated value (CSV) files (provided by MT), attached as *TestXXX.csv*. In the CSV-files, the decimal mark in the variable values were logged as comma separated instead of dot-separated, i.e. e.g. 0.004 was logged as 0,004, so the CSV file had to be processed with *csvfix.m*. Next, a data set was created by extracting the proper values corresponding to each logged variable (provided by [41]). To be more comparable with the Simulink case study, the data set was then rotated from BODY to NED-coordinates by $\boldsymbol{R}(\psi)$, i.e. the principal rotation about the z axis given in (2.7). In addition, the forces and moments were scaled from ton-force to Newton and Newton meters. As the logged data from time to time was induced with noise, a low-pass filter was also introduced, as attached in *lowpass.m*. Next, the data sets from the simulations that were to be compared, needed to be time synchronized as the simulation had to be started and stopped manually. The syncing is implemented in *plot_debug_dataset_final.m*, where the different data sets are synced to when the first occurring thrust exceeds a given limit, which represents the time of the applied disturbance. The logged data consisted of position and heading deviations, and applied thruster feedback, in surge, sway and yaw.

7.2.1 Case Outline

MT provided the opportunity to simulate with and without Disturbance Rejection by Acceleration Feedforward (AFF), as well as with and without cubic stiffness in the PID controller. Therefore the following scenarios were considered:

- Sideways unknown disturbance, Section 7.2.2
- Head-on unknown disturbance, Section 7.2.3

- Position change, Section 7.2.4

The purpose of first two cases was to test the performance and robustness of the vessel when subjected to different sudden unknown external forces. The purpose of the third case was to explore how the different control strategies affected a basic DP maneuver, when not exposed to external disturbances.

All cases were tested with four different control strategies: with added AFF, with added cubic stiffness, with both cubic stiffness and AFF, and with the existing MT PID controller.

In each simulation, the vessel was initialized in $\boldsymbol{\eta} = \begin{bmatrix} 0 & 0 & 0 \end{bmatrix}^T$, and subjected to a disturbance or reference change after some time. No other external disturbances such as wind or current was turned on, as to keep the focus on the sudden unknown disturbances. Simulated wave forces were not available, and thus not included in the simulations.

The AFF was implemented by MT as described in Section 4.2.1 with no additional measurement delay, i.e. $\delta = 0$, only with the exception that the mass and damping matrices $\boldsymbol{M}$ and $\boldsymbol{D}$ are diagonal in the MT simulator, such that the control force from the AFF reduced to

$$\boldsymbol{\tau}_{FF} = \begin{bmatrix} M_{11}\hat{a}_x + D_{11}\hat{\nu}_x - \tau_x \\ M_{22}\hat{a}_y + D_{22}\hat{\nu}_y - \tau_y \\ D_{33}\hat{\nu}_\psi - \tau_\psi \end{bmatrix} \tag{7.1}$$

The cubic stiffness term was implemented by MT as $\boldsymbol{K}_{p3}\boldsymbol{e}^3$ where $\boldsymbol{e}$ is the position and heading deviation vector. In the Simulink case study, the heading deviation is given in radians, while MT calculated the deviation in degrees, thus making the cubic term much more responsive against heading errors. The gains were thus chosen after some trail and error as $\boldsymbol{K}_{p3} = \text{diag}\left(\left[1, 1, \frac{\pi}{180}\right]\right) = \text{diag}\left(\left[\frac{1}{3}, \frac{1}{3}, \frac{\pi}{378}\right]\right)\boldsymbol{K}_p$, where $\boldsymbol{K}_p$ is the proportional gain matrix of the PID controller in the simulator.

7.2.2 Case 1: Sideways Unknown Disturbance

The vessel was simulated with $\boldsymbol{\eta}_d = 0$, such that the logged deviation vector represented the position and heading in the NED-frame. The vessel was subjected to an external force with magnitude F_I = 1e5, point of impact $\boldsymbol{p}^b_{I,CG} = \begin{bmatrix} 40 & 9 \end{bmatrix}^T$ and angle of impact $\theta_{AoI} = 80$ degrees. This represents a disturbance impacting on the right corner of the bow. The function *pred_force.m* from Section 5.4 was used to calculate the force vector, which became $\boldsymbol{\tau}_{disturbance} = \begin{bmatrix} \text{-1.7e4} & \text{-9.9e4} & \text{-3.8e6} \end{bmatrix}^T$ (N, N, Nm).

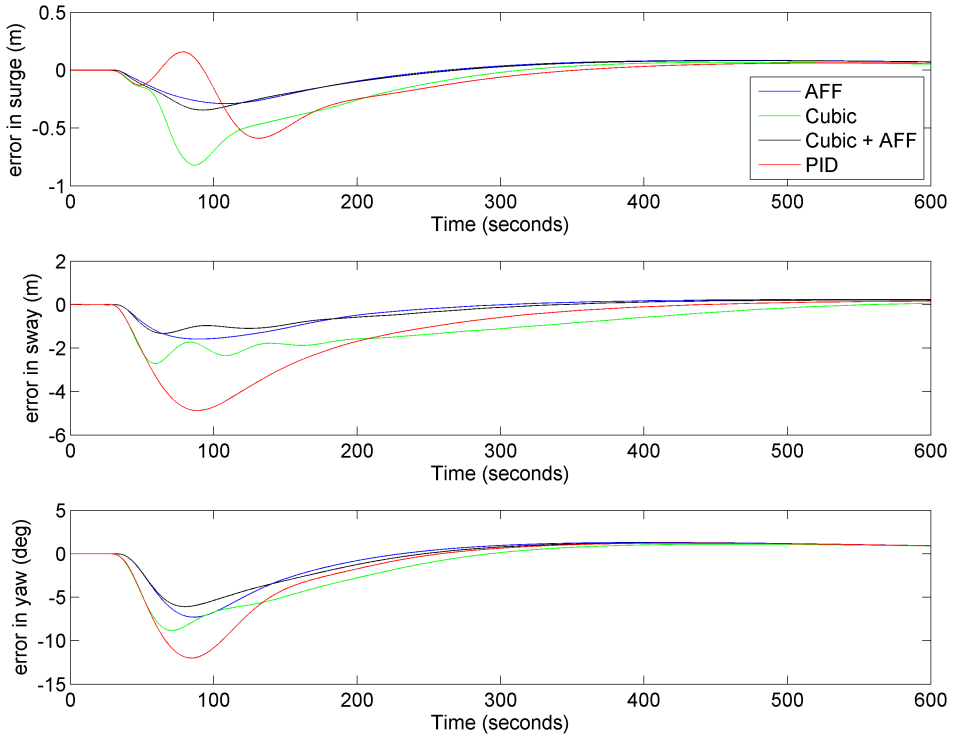

Figure 7.2.3: Case 1, position and heading deviations for four different control strategies.

As seen in Figure 7.2.3, the control strategies with AFF yield the best performances, while the cubic controller yields less offset in sway and yaw at the expense of slower convergence. The AFF controller yields the smoothest performance in all DOFs, while the cubic+AFF has slightly better performance in yaw and similar performance in surge, although with some oscillating behavior in sway. This may imply a too aggressive tuning of the cubic gain. As the disturbance impacts on the side of the vessel, it can be seen that the sway and heading are most affected. Compared to the PID controller, the AFF reduces the heading offset with about 5 degrees, while the offset in surge is reduced from approximately 5 meters to 1 meter. In surge, the oscillating deflection experienced with the PID controller is removed with the control strategies that include AFF.

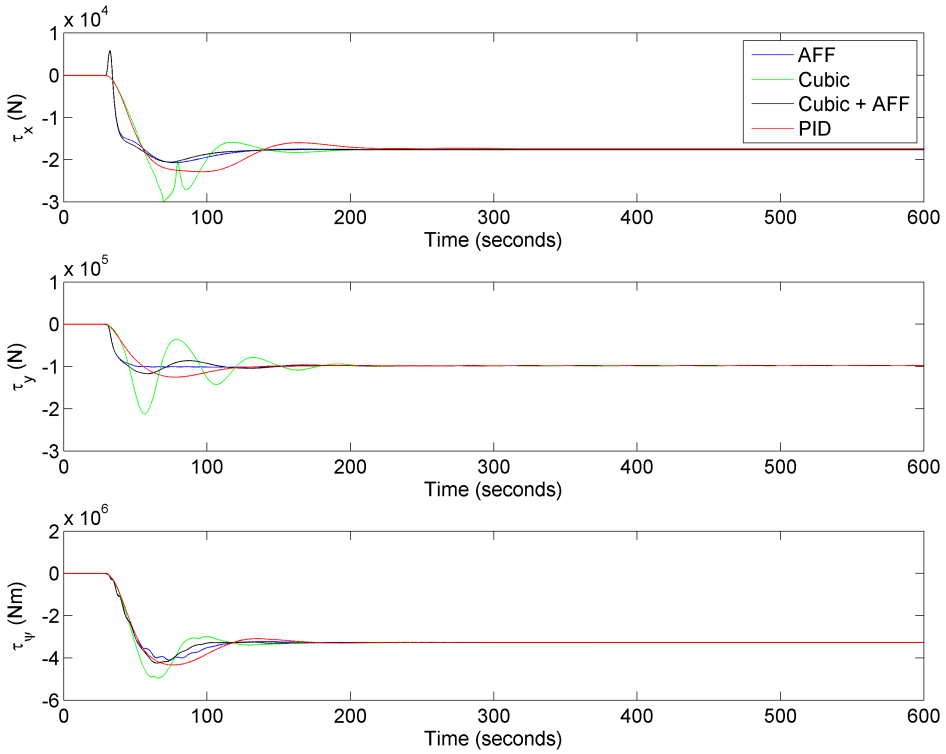

Figure 7.2.4: Case 1, thruster feedback for four different control strategies.

Figure 7.2.4 shows the corresponding thruster feedback from Case 1. It can be seen that the AFF control strategies immediately applies thrust to handle the sudden external disturbance in surge and sway. As there is no angular acceleration measurements available, the heading moment will not respond as quickly, but will still handle the disturbance by quickly converging to the value of the disturbing moment. The spike seen in the start of the surge force represents the corrective action by the AFF to damp the oscillating motion in surge illustrated in Figure 7.2.3. In addition, both AFF controllers apply less thrust than the PID as they have smaller maximal amplitudes and converge quicker to the disturbance value. The cubic controller applies the most thrust, and demonstrate a jerky thrust in surge as well as oscillating force in sway. Some rapid oscillatory behavior for the AFF controllers can be noticed in yaw, but this is most likely due to noise from the logging.

7.2.3 Case 2: Head-on Unknown Disturbance

The vessel was simulated with $\boldsymbol{\eta}_d = 0$, such that the logged deviation vector represented the position and heading in the NED-frame. The vessel was subjected to a large external force with magnitude $F_I = 4\text{e}5$, point of impact $\boldsymbol{p}^b_{I,CG} = \begin{bmatrix} 40 & 4 \end{bmatrix}^T$ and angle of impact $\theta_{AoI} = 10$ degrees. This represents a disturbance impacting

nearly head-on the bow. The function *pred_force.m* from Section 5.4 was used to calculate the force vector, which became $\boldsymbol{\tau}_{disturbance} = \begin{bmatrix} -3.9e5 & -7.0e4 & -1.2e6 \end{bmatrix}^T$ (N, N, Nm).

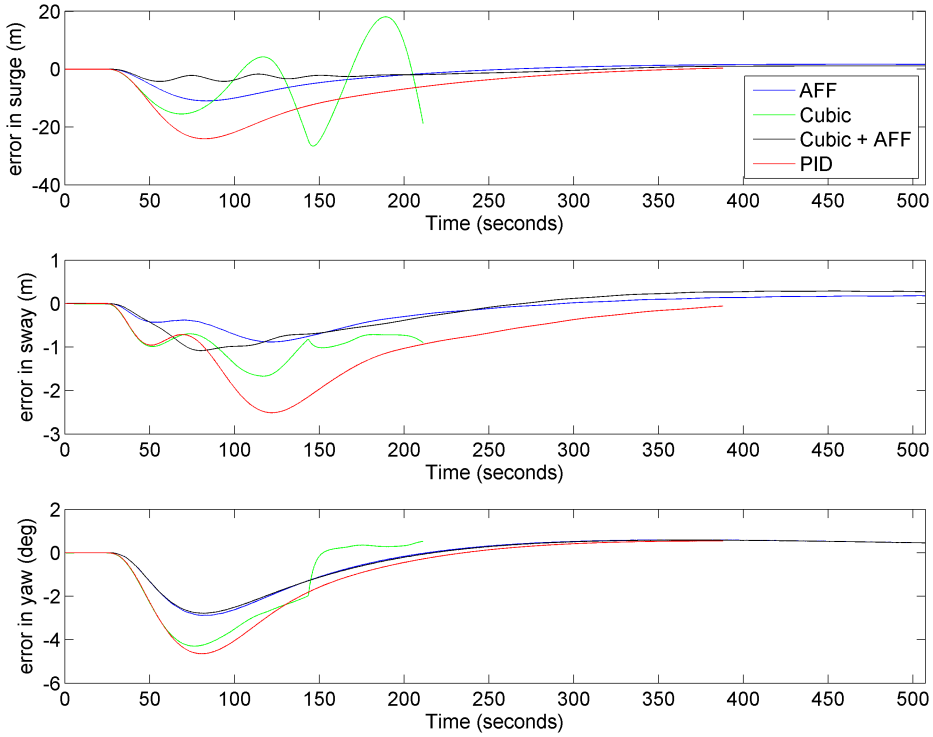

Figure 7.2.5: Case 2, position and heading deviations for four different control strategies.

As shown in Figure 7.2.5, the cubic+AFF combination has the overall best performance, while the cubic controller yields unstable results. The large disturbance yields such large errors in surge that the contribution from the cubic gain becomes too high, which may imply that the tuning of the cubic gain is too aggressive with respect to the dynamic capabilities of the thrusters. The aggressive tuning is also reflected in the cubic+AFF in surge, where some oscillations can be noticed. The AFF alone also yields satisfactory results. As the disturbance hits the vessel nearly head-on, the surge is most affected, and is thus also where the biggest improvements are found. The maximal offset from the reference is reduced from approximately 25 meters with the PID, to about 4 meters with the cubic+AFF approach. The AFF alone yields an offset of about 11 meters. In the sway axis, the AFF and cubic+AFF improves the offset with about 1.5 meters compared to the PID, while the heading is improved by approximately 2 degrees.

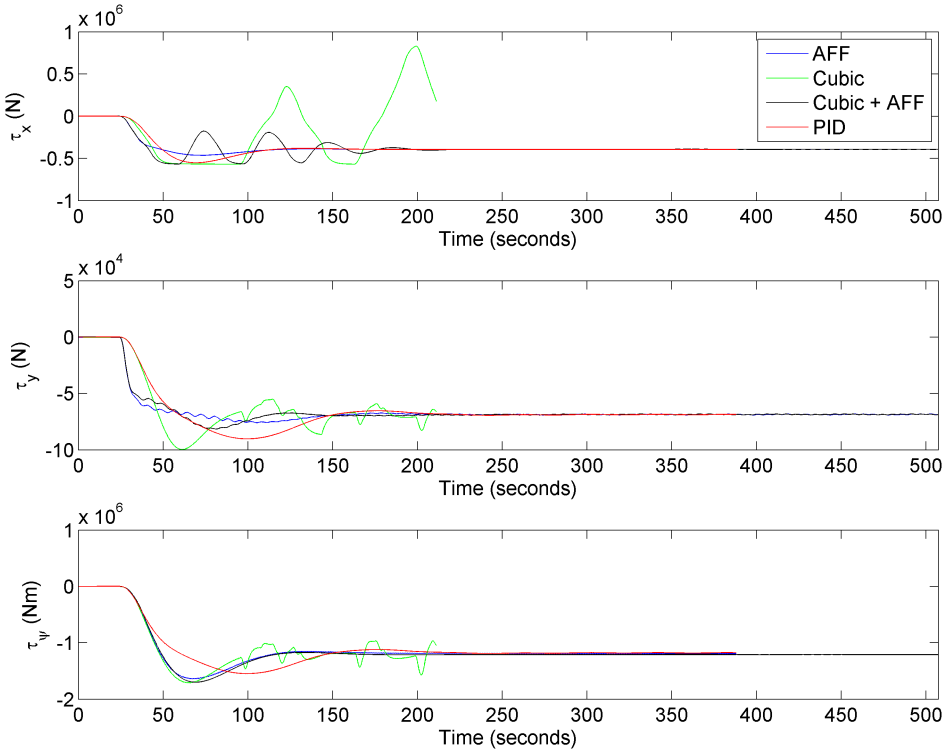

Figure 7.2.6: Case 2, thruster feedback for four different control strategies.

Figure 7.2.6 shows the corresponding thruster feedback from Case 2, where similarly as in Case 1, the control strategies with AFF respond more quickly to the disturbance in surge and sway, while the cubic is more aggressive and applies more thrust than the other combinations. The oscillations in surge from the cubic+AFF controller are more clearly represented, while the cubic thrust demonstrate some irregular behavior. Some rapid oscillatory behavior for the AFF controllers can be noticed in sway, but this is most likely due to noise from the logging.

7.2.4 Case 3: Position Change

The vessel was simulated with $\boldsymbol{\eta}_d = \begin{bmatrix} 5 & 5 & 0 \end{bmatrix}^T$ to explore how the different control strategies affect the vessel's ability to perform a simple low-speed maneuver. The plots for the yaw axis were left out due to some inconsistencies between the observed data and the logged data.

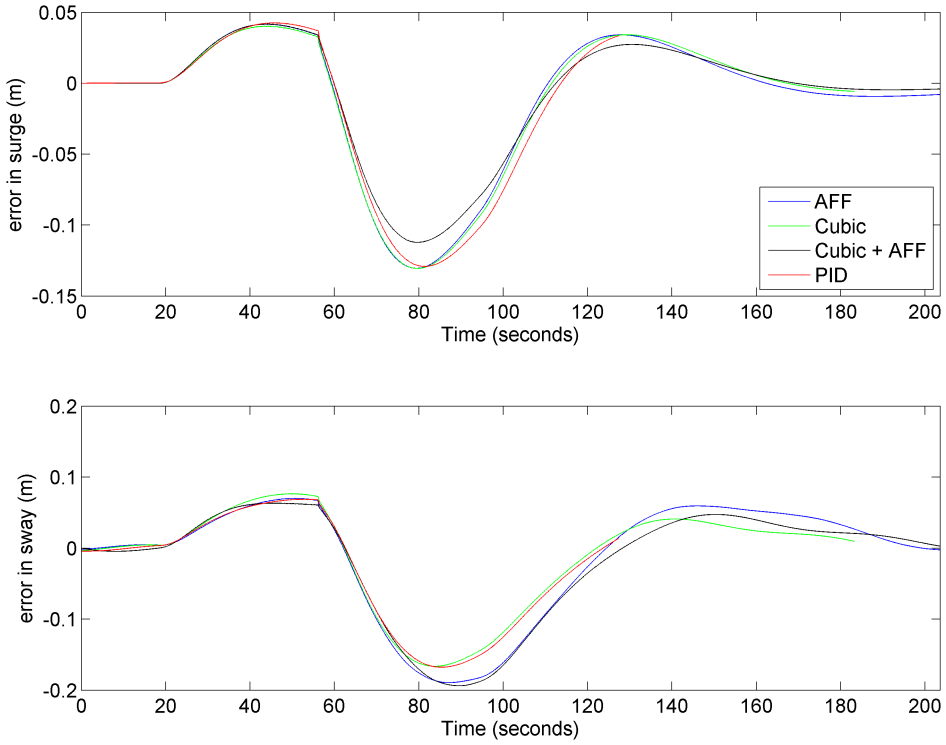

Figure 7.2.7: Case 3, position deviations for four different control strategies.

Figure 7.2.7 illustrates the deviations between the positions and the reference model, which generates a smooth time-varying reference signal. Apparently, the reference model is closely followed, such that the errors become very small. As expected, none of the control strategies affects the behavior significantly compared to the PID controller. This is due to the fact that there are no external disturbances, such that the AFF does not have any effect, and the fact that the error is so small that the cubic contribution becomes negligible.

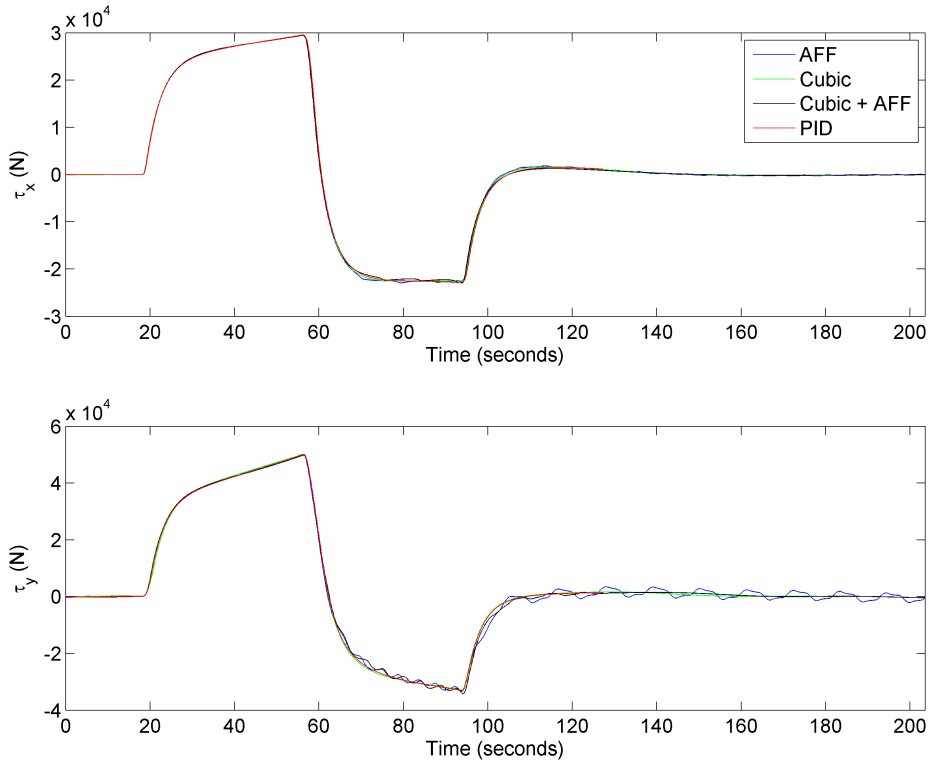

Figure 7.2.8: Case 3, thruster feedback for four different control strategies.

Figure 7.2.8 again illustrates that the different control strategies yield the same results when there are no large deviations due to sudden external disturbances. Again, some rapid oscillatory behavior for the AFF controllers can be noticed in sway, but this is likely due to noise from the logging.

7.2.5 ISE Comparison

As each simulation had varying duration, the ISE (see Section 7.1.7) was scaled by the simulation time to make the comparison valid, such that the ISE calculation (7.2) becomes

$$ISE = \frac{1}{t}\int_0^t e^2(\kappa)d\kappa \tag{7.2}$$

The ISO was high-pass filtered with the attached function *highpass_thrust.m* to only measure the excessive thrust applied to counteract the disturbances.

	x ISE	y ISE	ψ ISE	τ_x ISO	τ_y ISO	τ_N ISO
Case 1:						
AFF	0.3340	0.09526	0.3208	3.619	1.547	2.567
CS	1.53324	0.3752	0.5722	2.864	7.534	1.528
AFF+CS	0.3996	0.07159	0.2745	3.961	1.835	2.220
Case 2:						
AFF	0.1519	0.09894	0.3443	0.7304	1.952	1.447
CS	1.169	0.7023	1.486	67.97	16.07	10.86
AFF+CS	0.02544	0.1406	0.2657	3.782	1.454	1.875
Case 3:						
AFF	0.6314	0.9390	n/a	0.6380	0.6754	n/a
CS	0.7102	0.7382	n/a	0.7011	0.6940	n/a
AFF+CS	0.3624	0.6729	n/a	0.4748	0.4802	n/a

Table 7.2.1: ISE and ISO ratios between different control strategies and PID controller.

As can be seen in Table 7.2.1, for Case 1, the ISE for the AFF and the cubic+AFF have similar and good performance, while the cubic controller performs poorly. The ISE for the AFF and cubic+AFF have been greatly reduced, while the thrust ISO has increased for all DOFs. The cubic controller alone worsened compared to the PID in surge ISE as well as sway ISO. For Case 2, the cubic+AFF controller has the best ISE performance in surge, at the expense of higher surge ISO. The AFF has the overall best performance, with greatly reduced ISE and moderate increase in ISO, while the surge ISO is actually improved compared to the PID controller. As the cubic controller alone was unstable, the ISE/ISO measurements are very high. As recalled for the third case in Section 7.2.4, each control strategy demonstrated very similar performances. As the actual deviations were very small, the ISEs were also small. For instance, the surge ISE for the AFF was 0.0024 m^2 and 0.0039 m^2 for the PID, which makes the comparison invalid as the logged measurement noise may be dominant compared to the actual errors.

Chapter 8

Discussion

8.1 Predictive Feedforward Control

In Chapter 5, a predictive feedforward controller was implemented and tested against different disturbances. The controller was implemented as a pulse generator, providing proactive thrust at some time before an incoming external disturbance, such as an ice floe. For simplicity, only constant step disturbances were considered, as the purpose of the chapter was to explore what kind of accuracy that was needed for the estimate of the disturbance. In addition, as the predictive force was only applied up to the point of the disturbance, it would only influence how the impact of the disturbance affects the behavior of the vessel. After impact, the AFF controller would handle the disturbance and would thus not be influenced by the choice of a constant or varying disturbance. The same reason also applies to why the wave filter was not included in the predictive simulations, as it would only affect the behavior before and after the proactive action was applied. The selective wave filter however, would probably be triggered by the proactive force, but as it was only applied seconds before impact, the difference would be negligible. The general result of the simulations was that the proactive action showed promising possibilities of counteracting an incoming disturbance. It also showed that proactive force was not very effective for small disturbances, or that proactive moment would not be effective if the torque produced by the incoming disturbance was low. This is due to the fact that for small disturbing forces or produced torques, the room for improvement becomes small, while the room for worsening increases.

Concerning the prediction algorithm, the scenario where only one ice floe at a time was considered, is not a very realistic one. The algorithm could easily be augmented to handle several ice floes by calculating the total resulting disturbance vector, but this requires that there are few enough ice floes, and with distinctive enough movement patters such that a tracking algorithm can distinguish between them. It could also easily be augmented to fit a moving vessel, but stationkeeping has been the main focus in this thesis.

The next step in predictive feedforward control would be to investigate the possibility of correcting the position or heading, to handle large predicted disturbances. This would be applicable for situations when the DP operation allows a free heading or a large operating circle. However, as the yaw rate is slow (for the supply vessel modeled in Appendix B, a yaw rate of approximately 30 degrees/min was experienced), this kind of correction would require a more sophisticated observation and detection system. The detection of incoming disturbances must be available not seconds, but several minutes before the disturbance, such that if proactive action is decided to be taken by an ice intelligence system, the vessel will be able to reposition or change heading to better handle the disturbance. As the vessel is typically more slender in the longitudinal direction, ice impacting head-on would be a more desirable scenario. In addition, head-on impacting ice floes could be assumed to slide off the bow. The close-range proactive action methods from Chapter 5 could still be applied right before impact, to minimize the effect of the disturbance. In the cases of hazardous ice disturbances, such as ice bergs that surpass the DP capability, the danger must be identified in time, such that the impact can be avoided, either by aborting the DP operation or by towing the iceberg [20].

It should be mentioned that the limits for required accuracy of the estimated incoming disturbances are not very rigorous. They will vary with the choice of controller design and tuning, with the condition of other environmental forces such as waves, and with the properties of the incoming disturbance. They are also strongly coupled with the actuator dynamics with regards to rate limitations, turn times and capacities. As mentioned in Chapter 5, the choice of predictive parameters must be made with regards to the accuracy of the ice observation system. In the ideal case, where the accuracy is very good or perfect, the prediction parameters could in theory be optimized for a certain configuration, regarding control design, operation mode, sea state, etc.

It should also be mentioned that the shape of the hull should be more accurately modeled, to better determine how an incoming disturbance will influence the vessel. It can be noticed that all incoming disturbances in Chapter 5, impacted nearly normal to the hull. This was chosen as a simple set of cases to realize the constant disturbance. More realistic scenarios would include ice incoming at sharper angles, which could be assumed to slide along the hull, and thus produce varying and drifting forces that would eventually leave the vessel. This kind of disturbance is better realized as the varying ice-force used in Chapter 7 (see Figure 7.1.2).

8.2 Wave Filtering

In Chapter 6, a selective adaptive wave filter was proposed and tested. The filter consisted of a notch filter with a frequency that was adapted to fit the wave frequency, by estimates from a frequency tracker. The filter was made selective by using jerk measurements to identify sudden external disturbances. As perfect noise-free signals were used, differentiating the acceleration to find the jerk was not a problem. However, real measurements from the IMU will be noise-induced,

and even though they are fed through an observer, some noise residues will still remain. It is also commonly known that differentiating noise contaminated signals is not a good solution. A better approach would be to use the thruster feedback to identify the disturbance, as it would also reflect the presence of a disturbance. However, a problem of when to turn the wave filter back on again arises. When the disturbance has passed, the vessel will take some time to settle, but since the wave filter is off, the applied thrust will have a higher amplitude than before the disturbance occurred. This can be solved by setting the limits that trigger the selective part of the wave filter, large enough to guarantee that the unfiltered wave-induced thruster feedback will not be considered as a disturbance. This also makes sure that the wave filter is not turned off at the occurrence of an abnormally large wave or disturbances that are considered to be too small.

Regarding the placement of the wave filter, the two different approaches yield very similar results. The pre-controller placement experienced some overall better performance in ISE, while the post-controller performed better in ISO. As mentioned in Chapter 6, the reason for this is due to the fact that the pre-controller placement only filters the outer feedback loop, while the post-controller placement filters the inner feedback loop as well, where the inner loop is referred to as the thruster feedback loop to the AFF controller. The post-controller filter thus yields a more smooth applied thrust, at the expense of additional phase lag. This fact will in a way impair the comparison, as the tuning of the notch filter becomes the deciding factor. The tuning of the controller will also become an important factor, regardless of the AFF controller, as due to the nonlinearities in the PID controller, the pre-filtered control command will differ from the post-filtered commands. This issue makes it hard to conclude on the best performing placement of the filter. According to [45], the filter should be placed in front of the controller, while Section 11.1 in [1] suggests a post-controller placement. The general issue of tuning of the notch also arises, as there will be a compromise between phase lag and wave-force attenuation. As can be seen in Figure D.2.1 in Appendix D.2.1, there is a tradeoff between position ISE and thruster ISO. The user must decide on how to weight this tradeoff problem, and test several scenarios to end up with a suitable tuning. This would also involve the choice of the notch filter design, with regards to the structure of the transfer function, and if low-pass filters or additional notch filters should be included in a cascade.

It should also be mentioned that a high and low gain scheduling of the PID controller should be considered, as due to the phase lag introduced by the filter, the control bandwidth is affected. The scheduling variable could be chosen as the trigger variable in the selective wave filter Algorithm 6.2, where the gains could be set lower when the filter is turned on, and vice versa. Bumpless transfer techniques, as e.g. proposed in [46], can be used to facilitate smooth transitions between gain scheduled changes in the controller output. A more comprehensive gain scheduling approach to handle the varying sea state, as described in [47], could also be advantageously considered.

Some underdamped behavior was observed at the occurrences of the impacting and discharging disturbances, which leads to the questioning of correct PID tuning. Recalling the fact that the PID controller was tuned without incorporating thruster dynamics, can be assumed to be the most likely reason for the non-critical tuning. This unfiltered underdamped behavior was greatly amplified by the wave filter due to the added phase lag, which is especially seen in Figure 6.3.1. A control strategy with the AFF in combination with cubic damping alone could be considered as a possible measure, as it would provide additional and more aggressive damping.

The wave frequency tracker was implemented with a low-pass filter with decreasing frequency to stabilize the estimate. As it can be assumed that the modal wave-frequency is slowly varying over time, the final filter constant could be set very low to effectively lock the frequency estimate. However, this would make it vulnerable for changes in wave frequency, as it would very slowly converge to a new modal frequency, should the sea state change. This issue can be solved by resetting the frequency tracker from time to time, as it then would quickly converge to a new and more current estimate. In addition, it should be kept in mind that when using real noise-contaminated measurements, the differentiation of the high-pass filtered signal should be avoided due to the same reasons mentioned above.

Concerning the magnitudes of the ISEs and ISOs in Table 6.3.2, it should be mentioned that as long as the improved ISO ratios are lower than the ISE ratios worsen, the effect over time will increase in the general improvements favor. In addition, as long as the vessel stays inside the desired operating circle, the increased ISE will not matter, while the magnitude and modulation of the applied thrust are greatly reduced over time. This will in turn reduce both fuel consumption and actuator wear and tear.

8.3 Case Study

8.3.1 Simulink

In Section 7.1, five case studies are presented. The case studies represent Simulink simulations results of the different control strategies proposed in this thesis to improve the handling of sudden unknown external disturbances, compared to existing solutions, i.e. a nonlinear PID controller. The general result was that the Disturbance Rejection by Acceleration Feedforward (AFF) controller in combination with the nonlinear PID controller, had the overall best performance. The control strategy with an AFF controller in combination with a PID with cubic stiffness, was rejected after yielding unstable results in Case 2. This demonstrated the need for an added cubic damping term to compensate for the potential oscillating behavior from the aggressive stiffness term. The strategy with a PID + AFF + both cubic stiffness and damping, yielded very similar results to the AFF alone, but due to some oscillating performance in Case 2, this combination was also rejected. Although, it should be mentioned that an improved response could have been achieved with better tuning. As mentioned in Section 4.1.1, the proportional gain in the

PID controller could be reduced when adding cubic stiffness, which would reduce the control response for small deviations. For large errors however, the cubic term would quickly become dominating. The scenario without the AFF was also considered, but was rejected after demonstrating worse performance than the original PID (see figures in Appendix D.3.1). Furthermore, the three different proposed designs for acceleration feedback, i.e. constant gain, low-pass filtered gain and notch-filtered gain, were also examined. However, since the Disturbance Rejection by Acceleration Feedforward (AFF) method was the one that was implemented in the MT simulator, the same feedback was used in the Simulink simulation for more comparable results. A simulation of the three different feedbacks can found in Appendix D.3.2, where Figures D.3.3 and D.3.4 show that the performance is almost identical. An exception is that the notch-filtered AFF controller demonstrates a smoother thrust during the disturbance, although this is due fact that the selective wave filter is consequently turned off. As this seemingly does not delay the posture, this should maybe have been considered as the favorable approach.

Regarding the simulation results for the AFF controller, the stationkeeping capabilities were significantly improved compared to the PID controller. The ISEs were in some cases reduced by over 90%, at the slight drawback that the thruster feedback was more oscillatory. According to [25], the acceleration feedback should not increase the thrust use in the ideal case, but due to the rapidly oscillating wave disturbance, this was not the case. A possible solution would be to reduce the bandwidth of the PID controller, as since the AFF theoretically cancels out any external disturbance or unmodeled dynamics, the PID controller virtually experiences a calm sea state [26]. Thus a much less aggressive PID tuning could be used, which would lead to reduced wave-induced thruster use, which in turn would lead to lower fuel consumption and reduced actuator wear and tear. Additionally, it should also be mentioned that the AFF will also compensate for wind feedforward errors due to incorrect wind measurements, which according to [26] is a common issue in conventional DP systems.

8.3.2 MT

In Section 7.2, three cases from simulations with a simulator provided by Marine Technologies are presented. The general result coincided with the Simulink simulations as the AFF strategy yielded the best results. As the proposed control strategies were implemented by MT at an earlier stage, the possibility for cubic damping or filtered acceleration feedback was not included, and thus not available for testing. However, had the Simulink case study been executed sooner, the cubic controllers would already have been rejected, such that the focus could have been directed more in the direction of different acceleration feedback designs. In addition, as no wave-induced forces were available in the MT simulator, there was no need for including wave filter designs. As mentioned in Section 1.1, it is imperative to have the opportunity to run numerous simulations with an easily modifiable design, which is not the case with this simulator. This is due the fact that the simulations run in real time, such that numerous simulations would be very time demanding.

In addition, as the source code was not readily available for modifications, or that pre-designed script-based simulations were not possible, the requirement of an easy modifiable design was not met. The advantage of the MT simulator however, is a more realistic thruster response, as the actuation system is modeled with thruster allocation. Although, it could be observed that the thruster feedbacks were pretty similar in the Simulink simulations, suggesting that the first-order approximation of actuator dynamics in Section 2.5, was well suited.

The general result of the MT case study was that the AFF controller showed promising results, as it significantly reduced both the magnitude and the duration of the errors. As expected, the performance in surge and sway were most improved by the AFF, due to the use of the simulated linear acceleration measurements. The heading was also improved, but the applied moment did not respond as quickly due to the missing angular acceleration measurements. The ISE comparison was also consistent with the Simulink study, where the ISE was significantly reduced at the expense of slightly more aggressive thruster use. Some logging noise was experienced, but due to a not known, and thus not modifiable logging structure, the signals were low-pass filtered such that they coincided with the live trend-plots in the Operator Station (OS) interface. The logging noise can be assumed to originate from handling of UDP packages, as all exchange of information between the CC and the OS, goes through an Ethernet switch.

Chapter 9

Conclusion and Future Work

The main goals of this thesis were to evaluate opportunities for better handling of unknown external forces, compared to current DP controllers.

9.1 Conclusion

The following can be concluded based on the results in this thesis:

- A predictive feedforward control strategy for detection and counteraction of incoming disturbances has been proposed and tested in Simulink with promising results. As long as the force or torque exerted on to the vessel by the disturbance was predicted to be of significance, predictive action applied shortly before and in the general direction of the incoming disturbance, attenuated the impact. Regarding the predicted disturbance properties, the force was experienced to be the most influential, while it is also assumed to be the most difficult property to estimate.

- A selective notch wave filter with the frequency adapted by a wave-frequency tracker, has been implemented and tested in Simulink with good results. The selective wave filter greatly reduced the applied thrust force, while hardly affecting stationkeeping performances. With correct filter tuning such that the vessel is kept inside the operating circle, this approach would lead to significantly reduced fuel consumption and actuator wear and tear.

- A PID controller augmented with cubic stiffness was proposed, but even though proven globally asymptotically stable by Lyapunov stability techniques, the controller was rejected after demonstrating unstable results in both the Simulink and MT simulations. The proposedly improved PID controller with both cubic stiffness and damping showed stable results, but was also rejected due to oscillating behavior most likely caused by poor tuning.

- A Disturbance Rejection by Acceleration Feedforward (AFF) controller was implemented in combination with a PID controller, and simulated in Simulink

and a simulator provided by Marine Technologies. The controller demonstrated excellent stationkeeping performance when exposed to different external disturbances, and thus greatly outperformed the existing PID controller configuration. The Simulink simulation results were confirmed by coinciding test results in the MT simulator. The controller also demonstrated good performance when implemented in combination with the selective wave filter and the predictive feedforward controller. The robustness of the AFF controller has also been demonstrated by showing that it performs just as well with uncertain system parameters.

9.2 Future Work

Several techniques for better handling of external disturbances have been proposed and simulated with satisfying results. There is, however, great room for improvement, and a few suggestions are listed below:

- The accuracy of the ice observation system should be explored more thoroughly, as it would easier justify the limits for the predictive feedforward controller.
- By modeling incoming disturbances in the NED-frame, the detection algorithm and predictive feedforward controller could be tested more realistically, instead of just applying a constant force vector in BODY-coordinates. This would also facilitate for testing of the long range prediction methods discussed in Section 8.1.
- Tuning of the wave filter parameters and structure should be further investigated to figure out a desirable compromise between phase lag and wave attenuation. Adaptive gains or gain scheduling with regards to the varying sea state could also be considered.
- The Disturbance Rejection by Acceleration Feedforward controller should be implemented and tested with external disturbances in closed loop on a DP vessel, to test how real life performances reflect the simulated results.

Bibliography

[1] T. I. Fossen, *Handbook of Marine Craft Hydrodynamics and Motion Control*. John Wiley & Sons Ltd., 2011.

[2] A. Witkowska, "Dynamic positioning system with vectorial backstepping controller," in *18th International Conference on Methods and Models in Automation and Robotics (MMAR), 2013*, Aug 2013, pp. 842–847.

[3] S. Kerkeni, X. D. Santo, and I. Metrikin, "Dynamic Positioning in Ice - Comparison of control laws in Open Water and Ice," *32nd International Conference on Ocean, Offshore and Arctic Engineering (OMAE2013)*, 2013.

[4] J. G. Balchen, N. A. Jenssen, and S. Sælid, "Dynamic positioning using Kalman filtering and optimal control theory," *Proc. IFAC/IFIP symposium on automation in offshore oil field operation, Amsterdam, The Netherlands*, 1976.

[5] J. G. Balchen, N. A. Jenssen, E. Mathisen, and S. Sælid, "A Dynamic Positioning System Based on Kalman Filtering and Optimal Control," *Modeling, Identification and Control*, vol. 1, pp. 135–163, 1980.

[6] T. I. Fossen, S. I. Sagatun, and A. J. Sørensen, "Identification of Dynamically Positioned Ships," *Modeling, Identification and Control*, vol. 17, pp. 153–165, 1996.

[7] A. J. Sørensen, S. I. Sagatun, and T. I. Fossen, "Design of a dynamic positioning system using model-based control," *Modeling, Identification and Control*, vol. 17, no. 2, pp. 135–151, 1996.

[8] S. K. Volovodov, M. G. Chernjaev, A. J. Kaverinsky, S. S. Volovodov, and B. P. Lampe, "Control principle for dynamic positioning of offshore drilling platforms and ships," in *Proceedings of the 11th Symposium on Maritime Elektrotechnik, Elektronik und Informationstechnik, Rostock, Germany*, 2004.

[9] T. Perez and A. Donaire, "Constrained Control Design for Dynamic Positioning of Marine Vehicles with Control Allocation," *Modeling, Identification and Control*, vol. 30, no. 2, pp. 57–70, 2009.

[10] R. Indergård. (2010) Marine Operations in the Arctic. DNV. [Online]. Available: http://www.dnv.com/industry/oil_gas/publications/updates/arctic_update/2010/01_2010/marineoperationsinthearctic.asp

[11] A. J. Sørensen, "A survey of dynamic positioning control systems," *Annual Reviews in Control*, vol. 35, no. 1, pp. 123 – 136, 2011. [Online]. Available: http://www.sciencedirect.com/science/article/pii/S1367578811000095

[12] A. Keinonen, H. Wells, P. Dunderdale, R. Pilkington, G. Miller, and A. Brovin, "Dynamic Positioning Operation in Ice, Offshore Sakhalin, 1999," *Proceedings of the Tenth International Offshore and Polar Engineering Conference, Seattle, USA*, 2000.

[13] A. Keinonen, M. Shirley, G. Liljestrom, and R. Pilkington, "Transit and Stationary Coring Operations in the Central Polar Pack," *ICETECH - International conference*, 2006.

[14] N. A. Jenssen, S. Muddesitti, D. Phillips, and K. Backstrom, "DP In Ice Conditions," in *Dynamic Positioning Conference*, 2009.

[15] KMB Arctic DP, "Arctic DP: Safe and Green Dynamic Positioning Operations of Offshore Vessels in an Arctic Environment," 2013. [Online]. Available: http://www.marin.ntnu.no/arctic-dp/

[16] N. A. Jenssen, T. Hals, P. Jochmann, A. Haase, X. dal Santo, S. Kerkeni, O. Doucy, A. Gürtner, S. Støle Hetschel, P. Moslet, I. Metrikin, and S. Løset, "DYPIC - A Multi-National R&D Project on DP Technology in Ice," in *Proceedings of the Dynamic Positioning Conference 2012, Houston, Texas, USA*, 2012.

[17] D. T. Nguyen, A. Sørbø, and A. J. Sørensen, "Modelling and Control for Dynamic Positioned Vessels in Level Ice," *Manoeuvring and Control of Marine Craft, Guarujá, Brazil*, pp. 229–236, 2009.

[18] I. Metrikin, S. Løset, N. A. Jenssen, and S. Kerkeni, "Numerical Simulation of Dynamic Positioning in Ice," *Marine Technology Society Journal 47*, vol. 2, pp. 14–30, 2013. [Online]. Available: http://openurl.ingenta.com/content/xref?genre=article&issn=0025-3324&volume=47&issue=2&spage=14

[19] K. J. Eik, "Ice Management in Arctic Offshore Operations and Field Developments," Ph.D. dissertation, Norwegian University of Science and Technology, Trondheim, Norway, 2010.

[20] J. Haugen, L. Imsland, S. Løset, and R. Skjetne, "Ice Observer System for Ice Management Operations," *Proc. 21st Int. Offshore (Ocean) and Polar Eng. Conf., Maui, Hawaii, USA, June 19-24, 2011*, 2011.

[21] K. J. Eik, "Review of Experiences within Ice and Iceberg Management," *Journal of Navigation*, vol. 61, pp. 557–572, 2008.

[22] F. Scibilia, U. Jørgensen, and R. Skjetne, "AUV Guidance System for Subsurface Ice Intelligence," in *Proc. 31st Int. Conf. on Ocean, Offshore and Arctic Engineering (OMAE), Rio de Janeiro, Brazil, July 1-6 2012*, 2012.

[23] R. Skjetne, "Designing for effective stationkeeping in ice," *CeSOS Highlights and AMOS Visions Conference*, 2013.

[24] M. Skogvold, "Supervisory-switched Control for Dynamic Positioning Systems in Arctic Areas," Master's thesis, Norwegian University of Science and Technology, 2010.

[25] K.-P. W. Lindegaard, "Acceleration Feedback in Dynamic Positioning," Ph.D. dissertation, Norwegian University of Science and Technology, Trondheim, Norway, 2003.

[26] Ø. K. Kjerstad, R. Skjetne, and N. A. Jenssen, "Disturbance Rejection by Acceleration Feedforward: Application to Dynamic Positioning," *Proc. 18th World Congress of the International Federation of Automatic Control, Milano, Italy*, vol. 18, pp. 2523–2528, 2011.

[27] B. L. Stevens and F. L. Lewis, *Aircraft Control and Simulation.* John Wiley & Sons Ltd., 1992.

[28] A. J. Sørensen, "Structural issues in the design and operation of marine control systems," *Annual Reviews in Control*, vol. 29, no. 1, pp. 125 – 149, 2005. [Online]. Available: http://www.sciencedirect.com/science/article/pii/S136757880500012X

[29] T. I. Fossen, K.-P. W. Lindegaard, and R. Skjetne, "Inertia Shaping Techniques for Marine Vessels using Acceleration Feedback," *Proc. IFAC World Congress, Barcelona*, 2002.

[30] A. J. Sørensen, *Marine Control Systems Propulsion and Motion Control of Ships and Ocean Structures, Lecture Notes.* Department of Marine Technology, Norwegian University of Science and Technology, 2013.

[31] D. Garcia-Garcia, Y. Valeriano-Medina, L. Hernández, and A. Martínez-Laguardia, "Wave filtering for heading control of an AUV based on passive observer," *Indian Journal of Geo-Marine Sciences*, vol. 41(6), pp. 540–549, 2012.

[32] MSS, Marine Systems Simulator, 2010. [Online]. Available: http://www.marinecontrol.org/

[33] J. Blakelock, *Automatic Control of Aircraft and Missiles.* John Wiley & Sons, Inc, 1991.

[34] P. Encarnacao and A. Pascoal, "Combined trajectory tracking and path following: an application to the coordinated control of autonomous marine craft," in *Proceedings of the 40th IEEE Conference on Decision and Control, 2001.*, vol. 1, 2001, pp. 964–969 vol.1.

[35] H. Khalil, *Nonlinear Systems*. Prentice Hall, Jan. 2002.

[36] C. Ho, Z. qiang Lang, and S. A. Billings, "The benefits of nonlinear cubic viscous damping on the force transmissibility of a Duffing-type vibration isolator," in *UKACC International Conference on Control 2012*, 2012, pp. 479–484.

[37] F. Liu, "Pole Placement Control for Nonlinear Systems via Neural Networks," in *Advances in Neural Networks - ISNN 2004*, ser. Lecture Notes in Computer Science, F.-L. Yin, J. Wang, and C. Guo, Eds. Springer Berlin Heidelberg, 2004, vol. 3174, pp. 123–128. [Online]. Available: http://dx.doi.org/10.1007/978-3-540-28648-6_19

[38] P. A. Tipler and G. Mosca, *Physics for Scientists and Engineers, 5th edition*. W. H. Freeman, 2003.

[39] K. Rottmann, *Matematisk Formelsamling*, J. Reed, Ed. Bracan Forlag, 1995.

[40] V. Hassani, A. Sørensen, A. Pascoal, and A. Aguiar, "Multiple model adaptive wave filtering for dynamic positioning of marine vessels," in *American Control Conference (ACC), 2012*, 2012, pp. 6222–6228.

[41] T. E. Østrem, "Model Free IMU-based Dynamic Positioning State Estimator," Master's thesis, Norwegian University of Science and Technology, 2014.

[42] Analog Devices, Inc., *BASIC LINEAR DESIGN*, H. Zumbahlen, Ed., 2007.

[43] W. G. Price and R. E. D. Bishop, *Probabilistic theory of ship dynamics*. Chapman and Hall London, 1974.

[44] R. N. Clark, "Integral of the error squared as a performance index for automatic control systems," *American Institute of Electrical Engineers, Part II: Applications and Industry, Transactions of the*, vol. 79, no. 6, pp. 467–471, 1961.

[45] T. Hägglund, "Signal Filtering in PID Control," in *IFAC Conference on Advances in PID Control*, 2012.

[46] Y. Peng, D. Vrancic, and R. Hanus, "Anti-windup, bumpless, and conditioned transfer techniques for PID controllers," *Control Systems, IEEE*, vol. 16, no. 4, pp. 48–57, Aug 1996.

[47] G. Torsetnes, J. Jouffroy, and T. I. Fossen, "Nonlinear Dynamic Positioning of Ships with Gain-Scheduled Wave Filtering," *IEEE Conference on Decision and Control, Paradise Island, Bahamas, 2004*, 2004.

Appendix A

Nonlinear Stability Theory

Stability is reviewed by considering the nonlinear time-invariant system

$$\dot{\boldsymbol{x}} = \boldsymbol{f}(\boldsymbol{x}), \quad \boldsymbol{x}(0) = \boldsymbol{x}_0 \tag{A.1}$$

where $\boldsymbol{x} \in \mathbb{R}^n$ and $f : \mathbb{R}^n \to \mathbb{R}^n$ are continuous differentiable functions.
Let $\boldsymbol{x}_e$ be the equilibrium point of (A.1), i.e.

$$\boldsymbol{f}(\boldsymbol{x}_e) = 0 \tag{A.2}$$

Then the solutions $\boldsymbol{x}(t)$ of (A.1) are said to be [1]:

- *stable*, if, for each $\epsilon > 0$, there exists a $\delta(\epsilon) > 0$ such that

$$\|\boldsymbol{x}(0)\| < \delta(\epsilon) \Rightarrow \|\boldsymbol{x}(t)\| < \epsilon, \quad \forall t \geq 0 \tag{A.3}$$

- *unstable*, if it is not stable.

- *attractive*, if, for each $r > 0$, $\epsilon > 0$, there exists a $T(r, \epsilon) > 0$ such that

$$\|\boldsymbol{x}(0)\| \leq r \Rightarrow \|\boldsymbol{x}(t)\| < \epsilon, \quad \forall t \geq T(r, \epsilon) \tag{A.4}$$

  Attractivity implies convergence, i.e. $\lim_{t\to\infty} \|\boldsymbol{x}(t)\| = 0$.

- *locally asymptotically stable (LAS)*, if the equilibrium point $\boldsymbol{x}_e$ is stable and attractive.

- *globally asymptotically stable (GAS)*, if the equilibrium point $\boldsymbol{x}_e$ is stable $\forall \boldsymbol{x}(0)$ (region of attraction $\mathbb{R}^n$)

Theorem A.1. *Krasovskii-LaSalle's Theorem[1]*
Let $V : \mathbb{R}^n \to \mathbb{R}_+$ be a continuously differential positive definite function such that

$$V(\boldsymbol{x}) \to \infty \ \text{as} \ \|\boldsymbol{x}\| \to \infty \tag{A.5}$$

$$\dot{V}(\boldsymbol{x}) \leq 0, \quad \forall \boldsymbol{x} \tag{A.6}$$

Let Ω *be the set of all points where* $\dot{V}(\boldsymbol{x}) = 0$*, that is*

$$\Omega = \left\{ \boldsymbol{x} \in \mathbb{R}^n \mid \dot{V}(\boldsymbol{x}) = 0 \right\} \tag{A.7}$$

and M *be the largest invariant set in* Ω*. Then all solutions* $\boldsymbol{x}(t)$ *converge to* M*. If* $M = \{\boldsymbol{x}_e\}$ *then the equilibrium point* $\boldsymbol{x}_e$ *of (A.1) is GAS.*

Appendix B

Vessel Model Description

Vessel Model

The vessel model used in all Simulink simulations in this thesis was implemented as follows:

$$\dot{\boldsymbol{\eta}} = \boldsymbol{R}(\psi)\boldsymbol{\nu} \tag{B.1}$$

$$\boldsymbol{M}\dot{\boldsymbol{\nu}} + \boldsymbol{D}\boldsymbol{\nu} = \boldsymbol{\tau} + \boldsymbol{\tau}_{env} \tag{B.2}$$

where the parameters $\boldsymbol{M}$ and $\boldsymbol{D}$ represent a supply vessel, given in the MSS toolbox [32] as

$$\boldsymbol{M} = \begin{bmatrix} 5.3122\text{e}6 & 0 & 0 \\ 0 & 8.2831\text{e}6 & 0 \\ 0 & 0 & 3.7454\text{e}9 \end{bmatrix} \tag{B.3}$$

$$\boldsymbol{D} = \begin{bmatrix} 5.0242\text{e}4 & 0 & 0 \\ 0 & 2.7229\text{e}5 & -4.3933\text{e}6 \\ 0 & -4.3933\text{e}6 & 4.1894\text{e}8 \end{bmatrix} \tag{B.4}$$

$\boldsymbol{\tau}$ represents the applied thrust, while $\boldsymbol{\tau}_{env}$ represents environmental disturbances.

Thruster Configuration

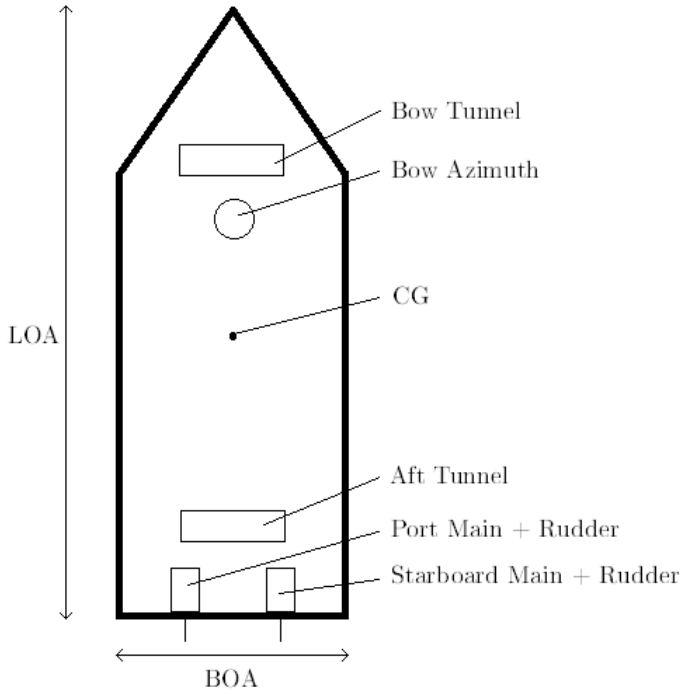

Figure B.0.1: Thruster configuration of vessel model. LOA = 85.2 and BOA = 19.2.

Figure B.0.1 illustrates the thruster configuration for the vessel used in the MT simulation in Section 7.2. The location of the thrusters with respect to CG are given in Table B.0.1, and the thruster capacities are given in Table B.0.2. The total available thrust is listed in Table B.0.3, and was found by the attached Matlab script *find_available_thrust.m*, by using the formula

$$\boldsymbol{\tau}_{max} = 9806.65 \left(\sum \boldsymbol{F}_t + \sum \boldsymbol{p}_t^b \times \boldsymbol{F}_t \right) \tag{B.5}$$

where $\boldsymbol{\tau}_{max}$ is the maximal positive thrust, i.e. positive in the x, y and ψ directions. $\boldsymbol{F}_t = [X, Y, 0]^T$ are the thruster capacities in ton-force given in Table B.0.2, and $\boldsymbol{p}_t^b = [x, y, 0]^T$ is a vector from CG to the thrusters, expressed in $\{b\}$, from Table B.0.1. For the torque contribution from the main propellers, the maximal of the rudder contribution and the main propeller was used, though it is trivial that the rudders yield the most torque. The limits were scaled from ton-force to Newton by using 1 ton-force = 9806.65 Newton. The same approach was used to find the minimal available thrust, i.e. the maximal available thrust in the negative surge, sway and yaw directions. It should be mentioned that the calculated limits are not

very rigorous, as a more complex thruster allocation would prevent the possibility of applying maximal thrust in all DOFs at once, i.e. e.g. the azimuth cannot produce max thrust in both surge and sway at the same time. These limits together with a thruster time constant $T_{tc} = 10$ seconds for each DOF, were used in all Simulink simulations. The thruster allocation and dynamics in the MT simulations were not known, but can be assumed to be more realistically modeled.

	x	y
Bow Tunnel	34.3	0
Bow Azimuth	29.4	0
Aft Tunnel	-35.6	0
Port Main	-39.6	-3.9
Starboard Main	-39.6	4.1

Table B.0.1: Thruster locations, where x and y represent BODY coordinates with respect to CG, given in meters.

	X	Y
Bow Tunnel	0	$\pm$13.7
Bow Azimuth	$\pm$16.3	$\pm$16.3
Aft Tunnel	0	$\pm$13.7
Port Main	35.9	0
Port Main reverse	-21	0
Starboard Main	35.9	0
Starboard Main reverse	-21	0
Port Rudder	0	$\pm$15.5
Starboard Rudder	0	$\pm$15.5

Table B.0.2: Thruster capacities, where X and Y represent force in surge and sway, given in ton-force.

	X (N)	Y (N)	N (Nm)
Max Thrust	8.6397e5	7.3256e5	2.6129e7
Min Thrust	-5.7173e5	-7.3256e5	-2.6129e7

Table B.0.3: Total available thrust, where X, Y and N represent force in surge and sway, and moment in yaw, respectively.

Appendix C

Attachment Description and Matlab Code

Every file use to produce the plots presented in this thesis have been electronically attached. It is however required that Matlab is installed to be able to run the files. A Matlab library called MSS GNC is also required, and can be downloaded from [32]. A brief description of the attached Matlab files and functions follows:

.m files

- init.m - Initialize global constants.
- find_available_thrust.m - Calculate available thrust limits.
- case_study.m - Simulink case study.
- case_study_wave_filtering.m - Wave filter simulations.
- plot_debug_dataset.m - Process and plot data logged from MT simulations.
- MT_find_ISE.m - Find ISE for MT simulations.
- lowpass.m - Low-pass filter MT measurements.
- highpass_thrust.m - High-pass filter MT thrust measurements.
- csvfix.m - Fix CSV file by replacing comma separated decimal-markers with dots.
- create_log_dataset.m - Create dataset from CSV file.
- predictive_sim_find_box_limits.m - Predictive simulation, find predictive box limits.
- predictive_sim_find_box_limits_fixed_time.m - Predictive simulation, find box limits with fixed time.

- find_box_limits.m - Find predictive box limits that have a ISE ratio less than 1.
- find_box_limits_worse.m - Find combinations that worsens ISE.
- predictive_sim_heading_vs_force_contour.m - Predictive simulation, heading vs force contour plots.
- predictive_sim_time_vs_force_contour.m - Predictive simulation, time vs force contour plots.
- predictive_sim_heading_vs_pp_contour.m - Predictive simulation, heading vs point of impact contour plots.
- pred_force.m - Calculate predictive force.
- error_sampling.m - Error sampling of Simulink cases.
- cube.m - Plot predictive cube.
- pidp3d3_plotting.m - Plot cubic controller testing.
- stiffness_plot.m - Cubic controller plotting.
- JONSWAP_plot.m - Bode plot of JONSWAP and notch wave filters.
- find_filter_parameters.m - Find tuning parameters for notch wave filter.
- case_study_test_LP_notch_AFF.m - AFF controller with filtered acceleration feedback.
- case_study_test_cubic_alone.m - Test with cubic controller alone.

.slx files

- sim_case_report.slx - Simulink model for controller case studies.
- sim_case_wf.slx - Simulink model for wave filter simulations.
- sim_prediction_report_test.slx - Simulink model for predictive case studies.
- sim_case_report_lpAFF.slx - Simulink model for low-pass AFF controller.
- sim_case_report_notchAFF.slx - Simulink model for notch AFF controller.
- pidp3d3.slx - Simulink model for testing of nonlinear stiffness and damping.

.csv files

- TestXXX.csv - Logged CSV-files from the MT simulations.

Simulink functions

- frequency_tracker - Frequency tracker algorithm, to estimate wave-frequency.
- selective_wave_filter - Selective wave filter algorithm.

Appendix D

Additional Results and Plots

D.1 Predictive Box Plots

D.1.1 Predicted Point of Impact 10 Meters Off

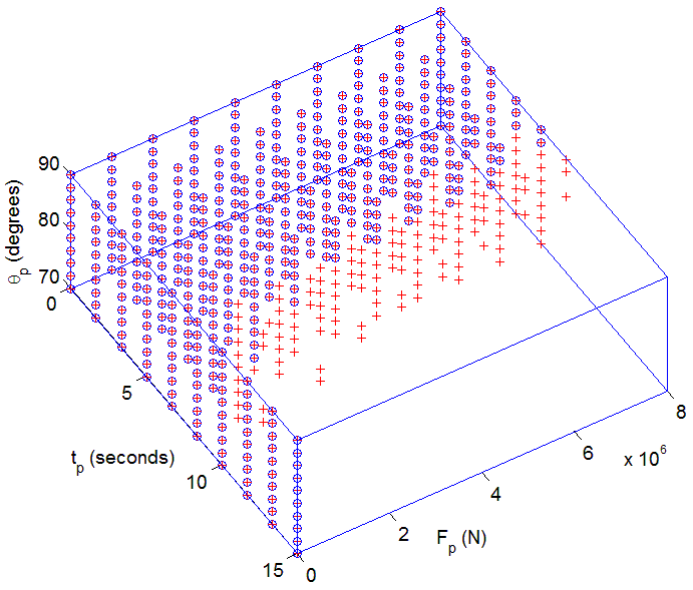

Figure D.1.1: Simulation of predictive box with $\Delta = 10$ and $\boldsymbol{p}_p^b = \begin{bmatrix} 30 & 9 \end{bmatrix}^T$, with large disturbance force: $F_I = 4e5$, $\boldsymbol{p}_{I,CG}^b = \begin{bmatrix} 40 & 9 \end{bmatrix}^T$, $\theta_{AoI} = 80°$.

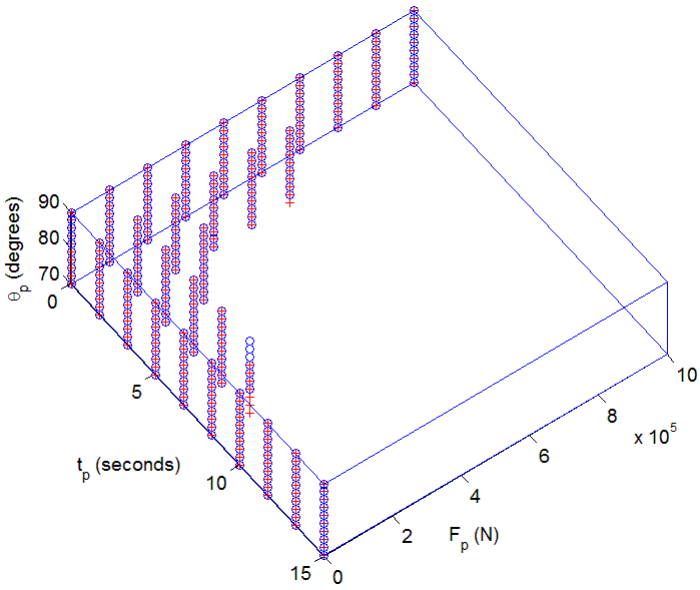

Figure D.1.2: Simulation of predictive box with $\Delta = 10$ and $\boldsymbol{p}_p^b = \begin{bmatrix} 30 & 9 \end{bmatrix}^T$, with small disturbance force: $F_I = 5e4$, $\boldsymbol{p}_{I,CG}^b = \begin{bmatrix} 40 & 9 \end{bmatrix}^T$, $\theta_{AoI} = 80°$.

D.1.2 Additional Plots for Minimal/Maximal Disturbances on Different Points of Impact and Angles

D.1.2.1 Almost Straight on Corner of Stern

Time vs Force

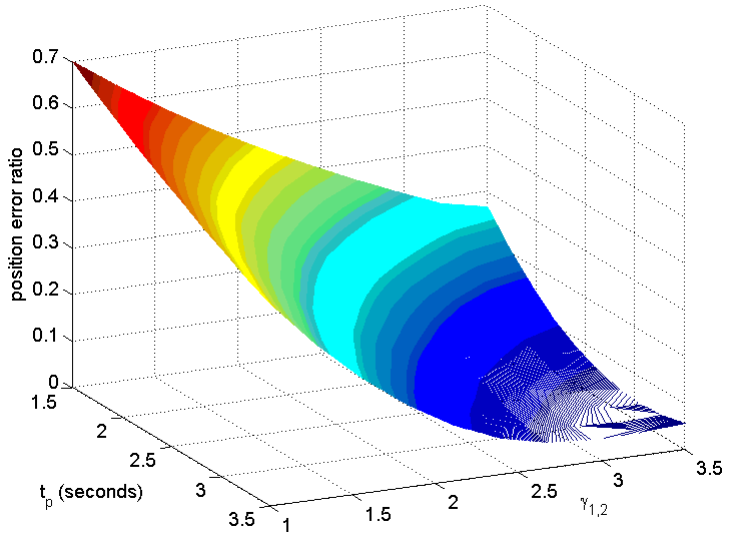

Figure D.1.3: Contour plot of the position ISE for t_p vs F_p. Large disturbance force: $F_I = 2e5$, $\boldsymbol{p}^b_{I,CG} = \begin{bmatrix} -42 & -9 \end{bmatrix}^T$, $\theta_{AoI} = 170$.

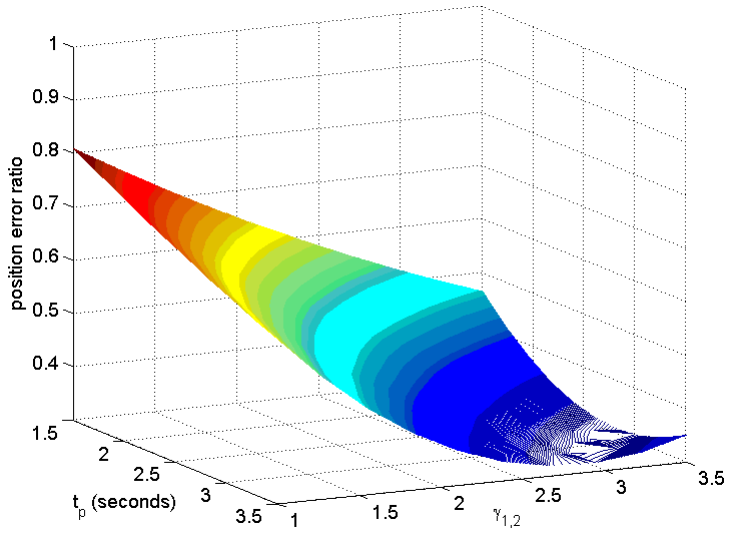

Figure D.1.4: Contour plot of the position ISE for t_p vs F_p. Small disturbance force: $F_I = 4e4$, $\boldsymbol{p}^b_{I,CG} = \begin{bmatrix} -42 & -9 \end{bmatrix}^T$, $\theta_{AoI} = 170$.

D.1.2.2 Almost Straight on Beam near CG

Time vs Force

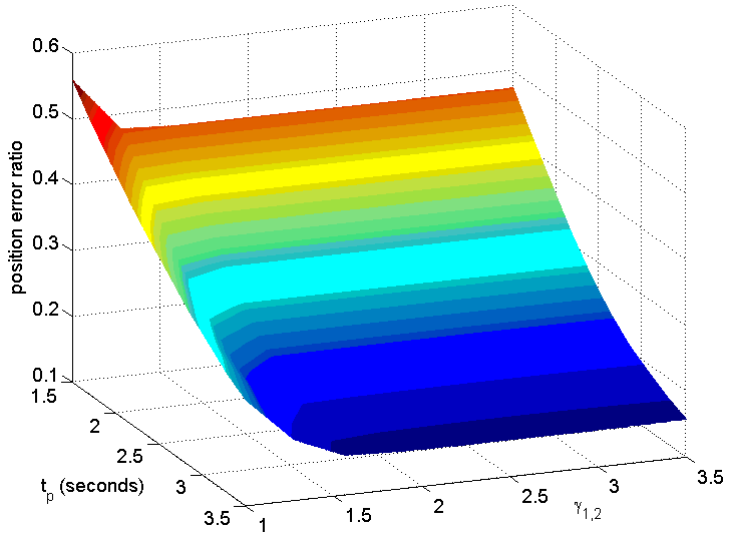

Figure D.1.5: Contour plot of the position ISE for t_p vs F_p. Large disturbance force: $F_I = 5e5$, $\boldsymbol{p}^b_{I,CG} = \begin{bmatrix} -5 & -9 \end{bmatrix}^T$, $\theta_{AoI} = -100$. Notice that the error ratio flats out for $\gamma_{1,2} > \approx 1.5$ due to saturation of the thrusters.

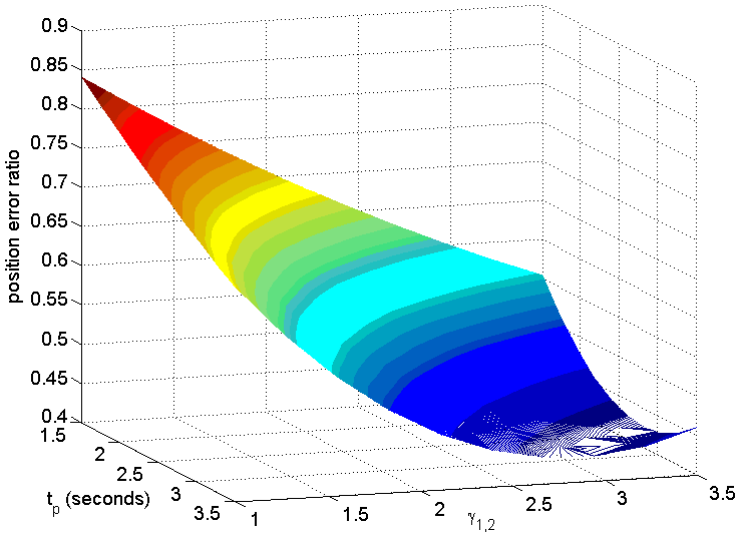

Figure D.1.6: Contour plot of the position ISE for t_p vs F_p. Small disturbance force: $F_I = 5e4$, $\boldsymbol{p}^b_{I,CG} = \begin{bmatrix} -5 & -9 \end{bmatrix}^T$, $\theta_{AoI} = -100$.

D.1.2.3 Almost Straight on Corner of Bow

Heading vs Force

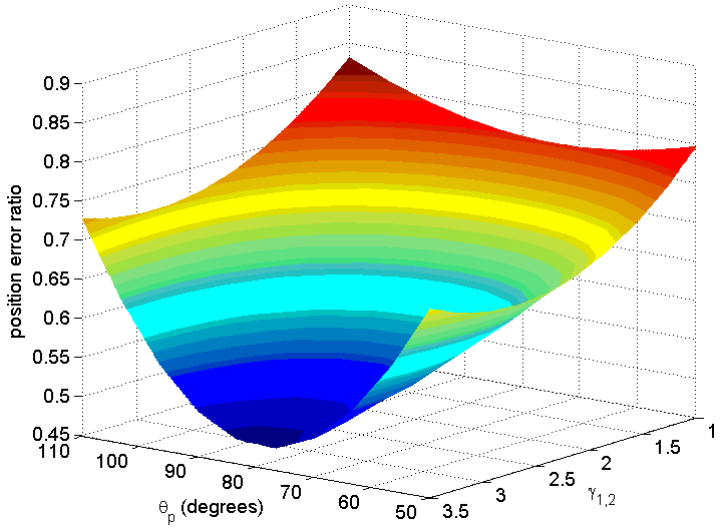

Figure D.1.7: Contour plot of the position ISE for θ_p vs F_p, $t_p = 2.5$. Small disturbance force: $F_I = 4e4$, $\boldsymbol{p}^b_{I,CG} = \begin{bmatrix} 40 & 9 \end{bmatrix}^T$, $\theta_{AoI} = 80$.

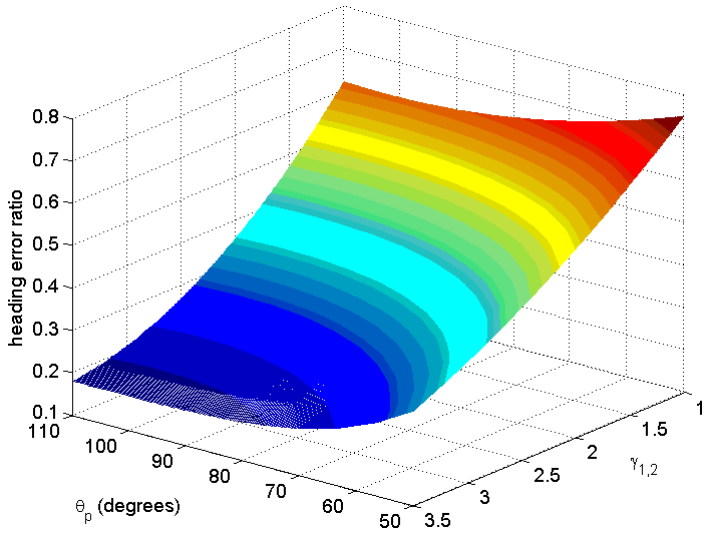

Figure D.1.8: Contour plot of the heading ISE for θ_p vs F_p, $t_p = 2.5$. Small disturbance force: $F_I = 4e4$, $\boldsymbol{p}^b_{I,CG} = \begin{bmatrix} 40 & 9 \end{bmatrix}^T$, $\theta_{AoI} = 80$.

D.2 Wave Filter Tuning

D.2.1 Tradeoff between ISE and ISO

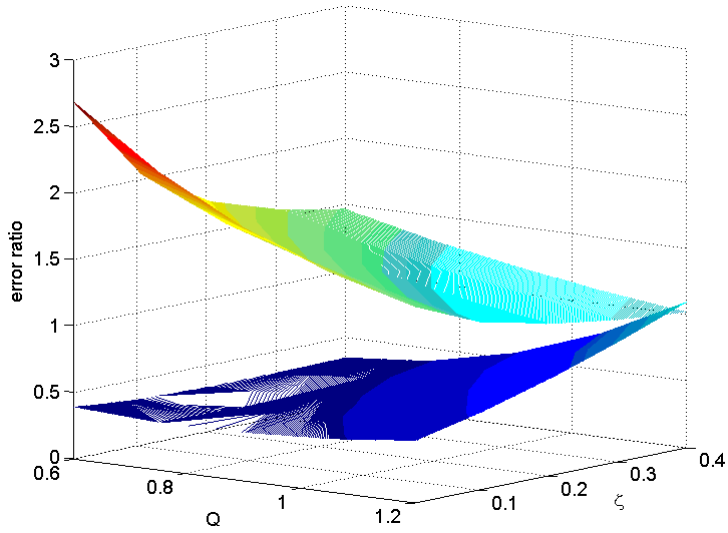

Figure D.2.1: Comparison of notch filter parameters Q vs ζ. The top layer represents ratio between position ISE with and without wave filtering, while the bottom layer represents the ISO ratio for surge. Wave disturbance of $H_s = 2.4$ meter and $\omega_0 = 1.1$ rad/s.

As seen in Figure D.2.1, there is a tradeoff between what combination of Q and ζ that yields an improvement in applied thrust, and what combination that worsens the position ISE. Plot created with the attached Matlab function *find_best_filter_parameters.m*.

D.3 Simulink Case Study

D.3.1 Cubic PID Controller without AFF

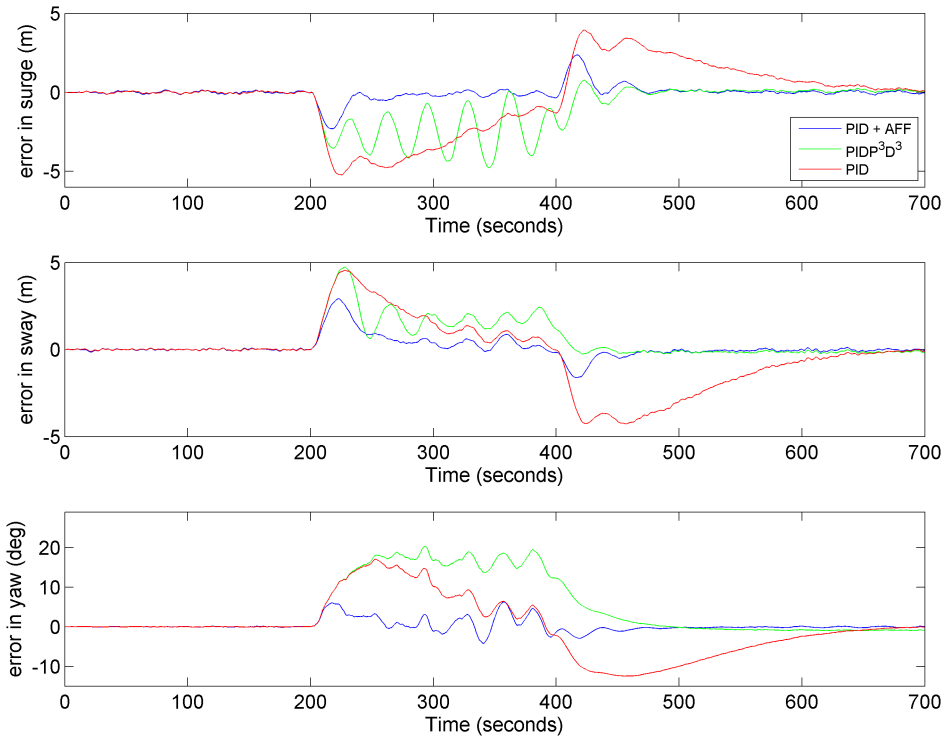

Figure D.3.1: Case 4, position and heading deviations for three different control strategies.

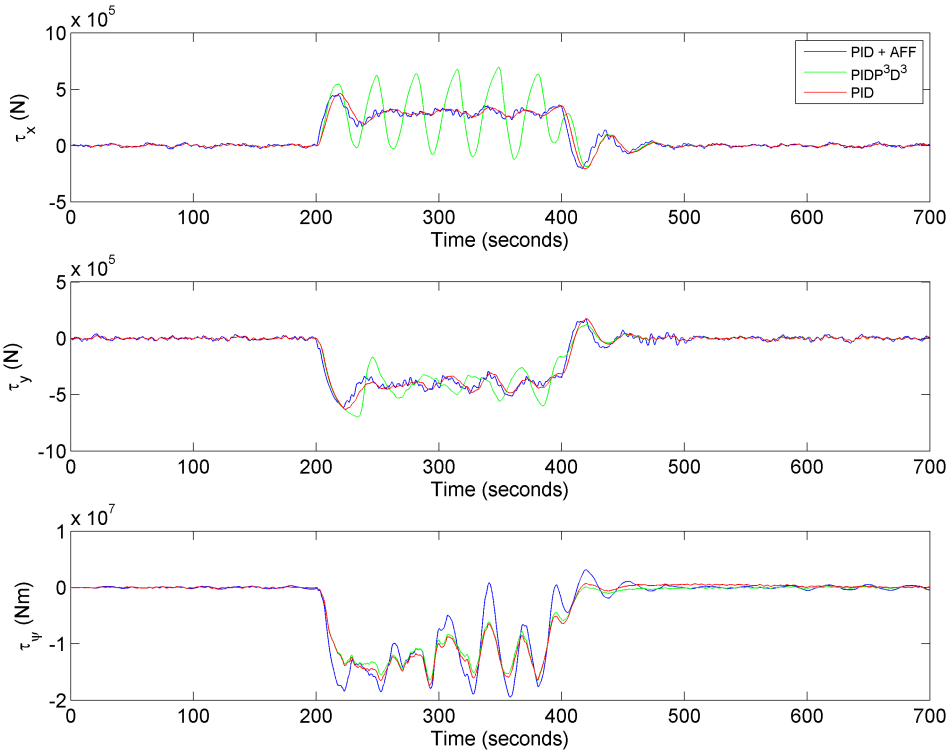

Figure D.3.2: Case 4, thruster feedback for three different control strategies.

D.3.2 AFF vs LP AFF and Notch AFF

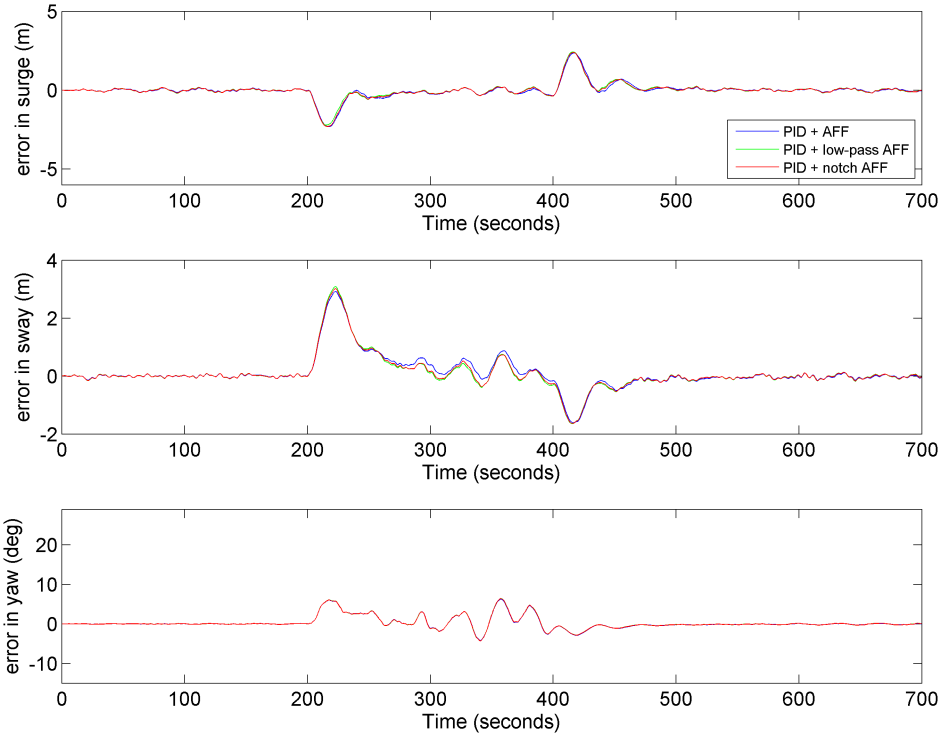

Figure D.3.3: Case 4, position and heading deviations for regular AFF vs low-pass filtered AFB and vs notch filtered AFB. Low-pass time constant $T = 1$ and notch frequency $\omega_n = \omega_0 = 1.1$ rad/s.

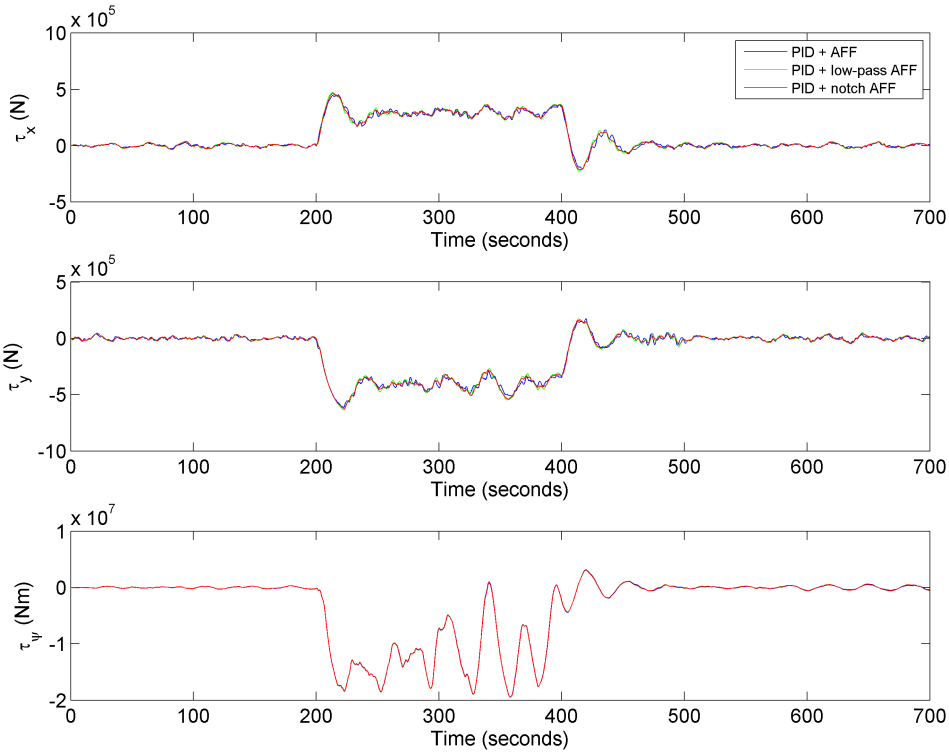

Figure D.3.4: Case 4, thruster feedback for regular AFF vs low-pass filtered AFB and vs notch filtered AFB. Low-pass time constant $T = 1$ and notch frequency $\omega_n = \omega_0 = 1.1$ rad/s.